

**UNIVERSIDADE FEDERAL DE ITAJUBÁ  
PROGRAMA DE PÓS-GRADUAÇÃO  
EM ENGENHARIA ELÉTRICA**

**Analog Radio over Fiber Solutions for Multi-band 5G  
Systems**

**Ramon Maia Borges**

**Itajubá, July 2020**

**UNIVERSIDADE FEDERAL DE ITAJUBÁ  
PROGRAMA DE PÓS-GRADUAÇÃO  
EM ENGENHARIA ELÉTRICA**

**Ramon Maia Borges**

**Analog Radio over Fiber Solutions for Multi-band 5G  
Systems**

**Thesis presented to the Postgraduate Program in  
Electrical Engineering in partial fulfillment of the  
requirements for the Doctorate Degree (PhD) in  
Electrical Engineering.**

**Concentration area: Microelectronics**

**Thesis committee:**

**Dr. Danilo Henrique Spadoti, Main Supervisor  
Dr. Arismar Cerqueira Sodré Junior, Supervisor  
Dr. José Antônio Justino Ribeiro  
Dr. Murilo Araujo Romero  
Dr. Marcelo Eduardo Vieira Segatto**

**July 2020  
Itajubá**

## Acknowledgments

Firstly, I would like to thank God for providing me this opportunity and granting me the capability to proceed successfully.

I express my gratitude to my family for the constant guidance and support, which made me able to face all challenges. I especially thank my grandparents Maury Maia e Maria do Carmo Ferrer Maia (*in memoriam*) who sacrificed so much to make me the person I am today. My Ph.D. would not have been possible if it were not for the initial encouragement and assistance I received from them. Special thanks also go to my mother Marilda Maia Cesarino and my aunt Maristela Ferrer Maia Pinto, who is a family's pillar.

I am grateful to my fiancée Ana Emília Fonseca de Castro for motivating me to improve my knowledge and moving my career forward. I was fortunate to have Ana as a partner in my life.

My sincere thanks also go to my supervisors, Prof. Dr. Danilo Henrique Spadoti and Prof. Dr. Arismar Cerqueira Sodré Junior, for accepting me as a Ph.D. student and allowing me to work in their research groups. I benefited a lot from their profound theoretical knowledge and experience. This work appears in its current form due to the guidance and critical comments of them.

I thank all my colleagues in the Wireless and Optical Convergent Access Laboratory for the assistance and pleasant working atmosphere. I am especially grateful to my co-workers Matheus Sêda Borsato Cunha, Luiz Augusto Melo Pereira, Eduardo Saia Lima and Hugo Rodrigues Dias Filgueiras for their valuable collaboration and inspiring discussions.

I also thank Alexandre Carvalho Ferreira, Tiago Reis Rufino Marins and Prof. Dr. Luciano Leonel Mendes who cooperated with the research progress by providing the 5G transceiver.

Acknowledgments go to the Federal University of Itajubá (Universidade Federal de Itajubá – UNIFEI) and National Institute of Telecommunications (Instituto Nacional de Telecomunicações – Inatel) for their important support and available infrastructure.

Acknowledgments also go to the PARKS, Fibracem, Keysight, Vivavox and Rohde & Schwarz companies for the partnership and technical support.

This work was partially supported by RNP, with resources from MCTIC, Grant No. No 01250.075413/2018-04, under the Radiocommunication Reference Center (Centro de Referência em Radiocomunicações - CRR) project of the Inatel, Brazil.

## Abstract

This study presents radio over fiber (RoF) solutions for the fifth-generation (5G) of wireless networks. After the state of the art and a technical background review, four main contributions are reported. The first one is proposing and investigating a RoF technique based on a dual-drive Mach-Zehnder modulator (DD-MZM) for multi-band mobile fronthauls, in which two radiofrequency (RF) signals in the predicted 5G bands individually feed an arm of the optical modulator. Experimental results demonstrate the approach enhances the RF interference mitigation and can prevail over traditional methods.

The second contribution comprises the integration of a 5G transceiver, previously developed by our group, in a passive optical network (PON) using RoF technology and wavelength division multiplexing (WDM) overlay. The proposed architecture innovates by employing DD-MZM and enables to simultaneously transport baseband and 5G candidate RF signals in the same PON infrastructure. The proof-of-concept includes the transmission of a generalized frequency division multiplexing (GFDM) signal generated by the 5G transceiver in the 700 MHz band, a 26 GHz digitally modulated signal as a millimeter-waves 5G band, and a baseband signal from an gigabit PON (GPON). Experimental results demonstrate the 5G transceiver digital performance when using RoF technology for distributing the GFDM signal, as well as Gbit/s throughput at 26 GHz.

The third contribution is the implementation of a flexible-waveform and multi-application fiber-wireless (FiWi) system toward 5G. Such system includes the FiWi transmission of the GFDM and filtered orthogonal frequency division multiplexing (F-OFDM) signals at 788 MHz, toward long-range cells for remote or rural mobile access, as well as the recently launched 5G NR standard in microwave and mm-waves, aiming enhanced mobile broadband indoor and outdoor applications. Digital signal processing (DSP) is used for selecting the waveform and linearizing the RoF link. Experimental results demonstrate the suitability of the proposed solution to address 5G scenarios and requirements, besides the applicability of using existent fiber-to-the-home (FTTH) networks from Internet service providers for implementing 5G systems.

Finally, the fourth contribution is the implementation of a multi-band 5G NR system with photonic-assisted RF amplification (PAA). The approach takes advantage of a novel PAA technique, based on RoF technology and four-wave mixing effect, that allows straightforward integration to the transport networks. Experimental results demonstrate

uniform and stable 15 dB wideband gain for Long Term Evolution (LTE) and three 5G signals, distributed in the frequency range from 780 MHz to 26 GHz and coexisting in the mobile fronthaul. The obtained digital performance has efficiently met the Third-Generation Partnership Project (3GPP) requirements, demonstrating the applicability of the proposed approach for using fiber-optic links to distribute and jointly amplify LTE and 5G signals in the optical domain.

## Resumo

Este trabalho apresenta soluções de rádio sobre fibra (RoF) para aplicações em redes sem fio de quinta geração (5G), e inclui quatro contribuições principais. A primeira delas refere-se à proposta e investigação de uma técnica de RoF baseada no modulador eletroóptico de braço duplo, *dual-drive* Mach-Zehnder (DD-MZM), para a transmissão simultânea de sinais de radiofrequência (RF) em bandas previstas para redes 5G. Resultados experimentais demonstram que o uso do DD-MZM favorece a ausência de interferência entre os sinais de RF transmitidos.

A segunda contribuição trata da integração de um transceptor de RF, desenvolvido para aplicações 5G e apto a prover a forma de onda conhecida como *generalized frequency division multiplexing* (GFDM), em uma rede óptica passiva (PON) ao utilizar RoF e multiplexação por divisão de comprimento de onda (WDM). A arquitetura proposta permite transportar, na mesma infraestrutura de rede, sinais em banda base e de radiofrequência nas faixas do espectro candidatas para 5G. A prova de conceito inclui a distribuição conjunta de três tipos de sinais: um sinal GFDM na banda de 700 MHz, proveniente do transceptor desenvolvido; um sinal digital na frequência de 26 GHz, assumindo a faixa de ondas milimétricas; sinais em banda base provenientes de uma PON dedicada ao serviço de Internet. Resultados experimentais demonstram o desempenho do transceptor de RF ao utilizar a referida arquitetura para distribuir sinais GFDM, além de taxas de transmissão de dados da ordem de Gbit/s na faixa de 26 GHz.

A terceira contribuição corresponde à implementação de um sistema fibra/rádio potencial para redes 5G, operando inclusive com o padrão “5G New Radio (5G NR)” nas faixas de micro-ondas e ondas milimétricas. Tal sistema é capaz de prover macro células na banda de 700 MHz para aplicações de longo alcance e/ou rurais, utilizando sinais GFDM ou *filtered orthogonal frequency division multiplexing* (F-OFDM), assim como femto células na banda de 26 GHz, destinada a altas taxas de transmissão de dados para comunicações de curto alcance. Resultados experimentais demonstram a aplicabilidade da solução proposta para redes 5G, além da viabilidade de utilizar redes ópticas pertencentes a provedores de Internet para favorecer sistemas de nova geração.

Por fim, a quarta contribuição trata da implementação de um sistema 5G NR multibanda, assistido por amplificação de RF no domínio óptico. Esse sistema faz uso de um novo método de amplificação, baseado no efeito não linear da mistura de quatro ondas, que

permite integração direta em redes de transporte envolvendo rádio sobre fibra. Resultados experimentais demonstram ganho de RF igual a 15 dB em uma ampla faixa de frequências (700 MHz até 26 GHz), atendendo simultaneamente tecnologias de quarta e quinta geração. O desempenho digital obtido atendeu aos requisitos estabelecidos pela 3GPP (Third-Generation Partnership Project), indicando a aplicabilidade da solução em questão para distribuir e conjuntamente amplificar sinais de RF em enlaces de fibra óptica.

## List of figures

Figure 1.1 – 5G general scenarios and requirements.....	02
Figure 1.2 – 5G X-haul vision regarding the physical architecture.....	05
Figure 2.1 – Structure of a generic PON. ....	15
Figure 2.2 – Basic TDM-PON topology.....	15
Figure 2.3 – Basic TWDM-PON topology.....	17
Figure 2.4 – Basic WDM-PON topology. ....	18
Figure 2.5 – WDM overlay schemes: (a) TDM-PON with video overlay; (b) TDM-PON with a set of wavelengths overlaid.....	21
Figure 2.6 – PONs coexistence scenario: (a) Optical access network; (b) Wavelength plan representation. ....	22
Figure 2.7 – Distributed radio access network: (a) BBU an RU integrated in the base station; (b) BBU in the cabinet and RRH close to the antennas. ....	23
Figure 2.8 – Centralized radio access network.....	24
Figure 2.9 – Digital radio over fiber scheme.....	27
Figure 2.10 – Analog radio over fiber scheme. ....	30
Figure 2.11 – E/O and O/E conversion schemes: (a) Direct modulation; (b) External modulation; (c) Direct detection; (d) Coherent detection. ....	31
Figure 2.12 – Block diagram of the 5G transceiver: (a) Transmitter; (b) Receiver. ....	34
Figure 2.13 – Principle of the DPD operation.....	36
Figure 2.14 – The main graphical interface of the 5G transceiver. ....	38
Figure 2.15 – Electrical spectra at the 5G transceiver RF output for OFDM, GFDM and F-OFDM waveforms: (a) All subcarriers on; (b) Some subcarriers off. ....	39
Figure 3.1 – MZM transfer function.....	42
Figure 3.2 – Optical spectrum at the MZM output: (a) MZM biased to QP; (b) MZM biased to MATP; (c) MZM biased to MITP. ....	44
Figure 3.3 – MZM types: (a) Single-drive; (b) Dual-drive; (c) Dual-parallel.....	44
Figure 3.4 – Multi-band A-RoF technique based on a single-drive Mach-Zehnder modulator. ....	45
Figure 3.5 – Multi-band A-RoF technique based on a dual-drive Mach-Zehnder modulator. ....	47

Figure 3.6 – Frequency response of the RoF system: (a) Schematic for realizing the $S_{21}$ measurements; (b) $S_{21}$ results for SD-MZM and DD-MZM. ....	49
Figure 3.7 – Experimental setup for evaluating the A-RoF techniques based on SD-MZM and DD-MZM. ....	49
Figure 3.8 – SNR of the received 6 and 28 GHz RF signals as a function of the photodetector input power: (a) RoF technique based on SD-MZM; (b) RoF technique based on DD-MZM.....	51
Figure 4.1 – Illustration of the 5G fronthaul using RoF technology. ....	53
Figure 4.2 – Block diagram of the RoF-based fronthaul architecture for multi-band 5G systems.....	55
Figure 4.3 – The experimental setup. ....	57
Figure 4.4 – Measured optical spectrum at the DD-MZM output.....	59
Figure 4.5 – GFDM-based 5G transceiver performance at 100 Mbit/s: (a) MER as a function of the RF-driven power and RF amplification; (b) Electrical spectrum from the B2B configuration; (c) Electrical spectrum from the integrated RoF and GPON with electrical amplification of 12 dB.....	60
Figure 4.6 – DPD impact on Scenario 4 for $P_{RF1} = P_{RFout} = 0$ dBm: (a) Received RF spectra; (b) Constellation with DPD off; (c) Constellation with DPD on. ....	61
Figure 4.7 – EVM as a function of the RF-driven power and bitrate for the 26 GHz signal.....	63
Figure 4.8 – Performance of the received 26 GHz RF signal at 1 Gbit/s for $P_{RF2} = 1$ dBm: (a) RF spectrum; (b) Constellation; (c) Eye diagram. ....	64
Figure 4.9 – GPON performance as a function of frame sizes and scenarios: (a) Throughput; (b) Latency.....	66
Figure 5.1 – Multi-application 5G fiber-wireless system proposal.....	68
Figure 5.2 – Multi-band FiWi 5G architecture based on RoF and WDM overlay.....	70
Figure 5.3 – Photographs of the FiWi system implementation in indoor environment. ....	72
Figure 5.4 – Photographs of the FiWi system implementation in outdoor environment. ....	72
Figure 5.5 – Measured electrical spectrum at the PD output for $\lambda_1$ . ....	73
Figure 5.6 – OFDM, GFDM and F-OFDM electrical spectra before radiation. ....	74
Figure 5.7 – MER analyses for the OFDM, GFDM and F-OFDM waveforms. ....	75
Figure 5.8 – Received 256- and 64-QAM F-OFDM constellations. ....	75
Figure 5.9 – The 5G NR resource block scheme.....	76
Figure 5.10 – 5G NR performance at 3.5 GHz, as a function of bandwidth.....	77

Figure 5.11 – The 5G NR spectra and constellations for 60 MHz bandwidth: (a) B2B; (b) RoF; (c) FiWi. ....	78
Figure 5.12 – EVM as a function of bandwidth, modulation and DPD usage. ....	79
Figure 5.13 – Performance analysis of the 4 Gbit/s signal at 26 GHz for 10 m range: (a) Constellation; (b) Eye diagram; (c) Electrical spectrum; (d) $EVM_{RMS}$ . ....	79
Figure 5.14 – 5G NR performance at 26 GHz as a function of bandwidth. ....	80
Figure 5.15 – The received 5G NR constellations from the FiWi system for 100 MHz bandwidth. ....	81
Figure 5.16 – The experimental setup for the M2M application. ....	81
Figure 5.17 – M2M application: (a) B2B latency measurement; (b) optical link latency measurement. ....	82
Figure 6.1 – The CRoF and PBRA-assisted RoF architectures. ....	85
Figure 6.2 – The CRoF and PBRA comparison: (a) electrical spectra at the photodetector output; (b) optical spectra at the photodetector input. ....	86
Figure 6.3 – PAA technique employing optical pumping after the electro-optic modulation process. ....	87
Figure 6.4 – Multi-band RoF system with photonic-assisted RF amplification. ....	88
Figure 6.5 – Measured electrical spectra at the PD output: (a) F-OFDM at 788 MHz; (b) LTE at 2.7 GHz; (c) 5G NR at 3.5 GHz; (e) QAM at 26 GHz. ....	91
Figure 6.6 – PAA characterization: (a) Flatness as a function of frequency; (b) Phase noise at 26 GHz. ....	92
Figure 6.7 – Digital performance analysis of the 26-GHz sub-bands for PAA and CRoF. ....	92
Figure 6.8 – Digital performance analysis of the F-OFDM, LTE, and 5G NR signals, assuming PAA without RF amplifiers and CRoF with two cascaded 12 dB EAs. ....	93

## List of tables

Table 1.1 – State of the art on RoF solutions for 5G.....	12
Table 2.1 – Summary of the PON standards and some of their aspects.....	19
Table 2.2 – CPRI options with the corresponding line coding factors and data rates.....	28
Table 2.3 – CPRI aggregated bit rates as a function of LTE, LTE-A and 5G scenarios.....	29
Table 2.4 – Fading points as a function of the radiofrequency. ....	33
Table 4.1 – GFDM point-to-multipoint distribution in the WDM overlay system. ....	62
Table 4.2 – 26-GHz point-to-multipoint distribution in the WDM overlay system.....	65
Table 5.1 – Optical and electrical power levels.....	72
Table 5.2 – Variables for throughput calculation. ....	76

## List of abbreviations and acronyms

3GPP	3rd Generation Partnership Project
4G	Fourth-generation
5G	Fifth-generation
6G	Sixth-generation
5G PHY	Flexible 5G physical layer
ADC	Analog-to-digital converter
AI	Artificial intelligence
Anatel	National Telecommunications Agency (in Portuguese)
AP	Access point
A-RoF	Analog radio over fiber
ASG	Analog signal generator
ASK	Amplitude shift keying
ATM-PON	Asynchronous transfer mode-passive optical network
AWG	Arbitrary waveform generator
BBU	Baseband unit
BDTM	Burst data transfer mode
BER	Bit error rate
BH	Backhaul
BPON	Broadband passive optical network
BS	Base station
B2B	Back-to-back
BW	Bandwidth
CAPEX	Capital expenditure
CATV	Cable television
CDTM	Continuous data transfer mode
CO	Central office
CoMP	Coordinate multi-point
CNR	Carrier-to-noise ratio
CP	Cyclic prefix
CP-OFDM	Cyclic prefix-based orthogonal frequency division multiplexing
CPRI	Common Public Radio Interface

C-RAN	Centralized radio access network
CRoF	Conventional radio over fiber
CRR	Radiocommunications Reference Center (in Portuguese)
CS	Cyclic suffix
CU	Central unit
CW	Continuous wave
CWDM	Coarse wavelength division multiplexing
DAC	Digital-to-analog converter
DAS	Distributed antenna systems
DCF	Dispersion compensating fiber
DD-MZM	Dual-drive Mach-Zehnder modulator
DEMUX	Demultiplexer
DFB	Distributed-feedback
DL	Downlink
DL-SCH	Downlink shared channel
DMLs	Directly modulated lasers
DMRS	Demodulation reference signal
DPD	Digital pre-distortion
DP-MZM	Dual-parallel Mach-Zehnder modulator
DPSK	Differential phase shift keying
DQPSK	Differential quadrature phase shift keying
D-RAN	Distributed radio access network
D-RoF	Digital radio over fiber
DSP	Digital signal processing
DU	Distribution unit
DVB-T	Digital Video Broadcasting-Terrestrial
DWDM	Dense wavelength division multiplexing
EA	Electrical amplifier
EAM	Electroabsorption modulator
ECL	External cavity laser
eCPRI	Enhanced Common Public Radio Interface
EDFA	Erbium doped fiber amplifier
eMBB	Enhanced mobile broadband
EMI	Electromagnetic interference

EMLs	Electroabsorption modulated lasers
EPON	Ethernet passive optical network
ESA	Electrical spectrum analyzer
ET	Ethernet tester
E/O	Electrical-to-optical
EVM	Error vector magnitude
FBG	Fiber Bragg grating
FBMC	Filterbank Multicarrier
FEC	Forward error control
FH	Fronthaul
FiWi	Fiber-wireless
F-OAN	Future optical access network
F-OFDM	Filtered Orthogonal Frequency Division Multiplexing
FSAN	Full Service Access Network
FTTB	Fiber-to-the-building
FTTC	Fiber-to-the-cabinet
FTTH	Fiber-to-the-home
FTTx	Fiber-to-the-x
FWM	Four-wave-mixing
GbE	Gigabit Ethernet
GFDM	Generalized Frequency Division Multiplexing
GPON	Gigabit passive optical network
HetNet	Heterogeneous network
HNLF	Highly nonlinear fiber
IEEE	Institute of Electrical and Electronics Engineers
IF	Intermediate frequency
IFoF	Intermediate frequency over fiber
IL	Insertion loss
IMT	International Mobile Telecommunications
Inatel	National Institute of Telecommunications (in Portuguese)
IQ	In-phase and quadrature
ISP	Internet service provider
ITU-R	International Telecommunication Union Radiocommunication Sector
ITU-T	International Telecommunication Union Standardization Sector

LD	Laser
LDPC	Low-density parity check
LO	Local oscillator
LOS	Line of sight
LTE	Long Term Evolution
LTE-A	Long Term Evolution-Advanced
M2M	Machine-to-machine
MATP	Maximum transmission point
MC	Media converter
MER	Modulation error ratio
MH	Midhaul
MIMO	Multiple input multiple output
MITP	Minimum transmission point
mMTC	Massive machine type communications
mm-waves	Millimeter-waves
MUX	Multiplexer
MWP	Microwave photonics
MZM	Mach-Zehnder modulator
NB-IoT	Narrowband Internet of things
NGFI	Next generation fronthaul interface
NG-PON1	Next generation passive optical network phase one
NG-PON2	Next generation passive optical network phase two
NG-PON3	Next generation passive optical network phase three
NR	New radio
OBF	Optical bandpass filter
OBSAI	Open Base Station Architecture Initiative
OC	Optical circulator
ODN	Optical distribution network
OFDM	Orthogonal Frequency Division Multiplexing
OGD	Optical general distributor
OLT	Optical line terminal
ONU	Optical network unit
OOBE	Out-of-band emission
OOK	On-off keying

OPC	Optical polarization controller
OPEX	Operational expenditure
OPM	Optical power monitor
ORI	Open Radio equipment Interface
O/E	Optical-to-electrical
OTPBF	Optical tunable passband filter
P2MP	Point-to-multipoint
P2P	Point-to-point
PA	Power amplifier
PAA	Photonic-assisted RF amplification
PAM	Pulse amplitude modulation
PBRA	Photonics-based RF amplifier
PC	Personal computer
PD	Photodetector
PIN	<i>p</i> -intrinsic- <i>n</i>
PLC	Programmable logic controller
PolM	Polarization modulator
PON	Passive optical network
PRBS	Pseudorandom binary sequence
PSK	Phase shift keying
QAM	Quadrature amplitude modulation
QP	Quadrature point
QPSK	Quadrature phase shift keying
RAN	Radio access network
RAU	Remote antenna unit or radio access unit
RB	Resource blocks
RBW	Resolution bandwidth
RF	Radiofrequency
RMS	Root mean square
RN	Remote node
RoF	Radio over fiber
RRU	Remote radio unit
RRH	Remote radio head
RU	Radio unit

RX	Receiver
SD-MZM	Single-drive Mach-Zehnder modulator
SDN	Software defined network
SFP	Small form-factor pluggable
SISO	Single-input single-output
SMF	Single mode fiber
SNR	Signal-to-noise ratio
ST	Space-time
TDD	Time division duplex
TDM-PON	Time division multiplexing-passive optical network
TR-STC	Time-reversal space-time coding
TV	Television
TWDM-PON	Time and wavelength division multiplexing-passive optical network
TX	Transmitter
UFMC	Universal Filtered Multi-carrier
UF-OFDM	Universal Filtered Orthogonal Frequency Multiplexing
UL	Uplink
UL-SCH	Uplink shared channel
UMTS	Universal mobile telecommunications system
URLLC	Ultra-reliable and low latency communications
USRP	Universal software radio peripheral
UWB	Ultra-wideband
VBW	Video bandwidth
VOA	Variable optical attenuator
VSA	Vector signal analyzer
VSG	Vector signal generator
WDM	Wavelength division multiplexing
WDM-PON	Wavelength division multiplexing-passive optical network
WiFi	Wireless fidelity
WiMax	Worldwide Interoperability for Microwave Access

## List of symbols

$a$	Number of 64-QAM symbols per subcarrier
$A$	Number of antennas per sector
$b$	Number of 256-QAM symbols per subcarrier
$b_s$	Number of bits per sample
$B_{\text{CPRI}}$	CPRI aggregated bit rate
$c$	Speed of light
$D$	Chromatic dispersion
$E_j(t)$	Sideband electrical field
$E_j$	Sideband amplitude
$E_o$	Optical carrier amplitude
$E_o(t)$	Optical carrier electrical field
$E_{\text{out}}(t)$	Electrical field at the MZM output
$f_s$	Sample rate
$f_{\text{RF}}$	RF signal frequency
$H$	Integer
$I_{\text{in}}$	MZM input optical intensity
$I_{\text{out}}$	MZM output optical intensity
$I(t)$	Current at the photodetector output
$(I_u, Q_u)$	Ideal symbol so-ordinates
$j$	Sideband order
$J_n$	Bessel function of the first kind of order $n$
$K$	Number of subcarriers
$L$	Fiber length
$L_{\text{DP}}$	Fiber length in which occur power fading
$L_{\text{NL}}$	Fiber length over which nonlinear effects become relevant
$LC$	Line coding factor
$M$	Number of subsymbols
$n$	Number of users
$N$	Number of symbols
$N_{64\text{DMRS}}$	Number of 64-QAM DMRS symbol per RB
$N_{64\text{SCH}}$	Number of 64-QAM DL-SCH channels

$N_{256\text{DMRS}}$	Number of 256-QAM DMRS symbol per RB
$N_{256\text{SCH}}$	Number of 256-QAM DL-SCH channels
$N_{\text{RB}}$	Number of allocated resource blocks
$OH$	Overhead factor
$P$	Optical power level
$P_{\text{HNLf}}$	Optical power at the HNLf input
$P_{\text{RF}1,2,\dots,n}$	RF-driven signal power
$P_{\text{RFout}}$	System RF output power
$P_{\text{th}}$	Optical power threshold
$Q_{64\text{-QAM}}$	Number of bits per 64-QAM symbol
$Q_{256\text{-QAM}}$	Number of bits per 256-QAM symbol
$R$	Responsivity of the photodetector
$R_{\text{b}}$	Throughput or bitrate
$\text{RF}_{1,2,\dots,n}$	RF-driven signal
$S$	Number of sectors
$S_0$	Fiber dispersion slope
$TF$	Transfer function
$T_{\text{frame}}$	Frame periodicity
$V$	Peak to mean voltage ratio
$V_{\text{bias}}$	MZM bias voltage
$V_{\text{e}}$	MZM incident electrical signal
$V_{\text{m}}$	RF-driven signal amplitude
$V_{\pi}$	MZM half-wave voltage
$\alpha$	Fiber attenuation
$\beta_2$	Second order dispersion
$\gamma$	Fiber nonlinear coefficient
$(\delta I_u, \delta Q_u)$	Error in the received symbol position
$\lambda$	Laser wavelength
$\lambda_0$	Zero-dispersion wavelength
$\lambda_{\text{LD}}$	Laser wavelength
$\varphi$	Phase shift between the RF-driven signals
$\varphi_j$	Sideband phase
$\varphi_0$	Optical carrier phase

$\omega_j$	Sideband angular frequency
$\omega_o$	Optical carrier angular frequency
$\omega_{\text{RF}}$	RF-driven signal angular frequency

## List of Publications

### Journals:

1. **R. M. Borges**, L. A. M. Pereira, H. R. D. Filgueiras, A. C. Ferreira, M. S. B. Cunha, E. R. Neto, D. H. Spadoti, L. L. Mendes, Arismar Cerqueira S. Jr., “DSP-based flexible-waveform and multi-application 5G fiber-wireless system,” *Journal of Lightwave Technology*, vol. 38, no. 3, pp. 642-653, Feb. 2020.
2. **R. M. Borges**, E. S. Lima, A. C. Ferreira, D. H. Spadoti, L. L. Mendes, Arismar Cerqueira S. Jr., “Multiband 5G NR system with photonic-assisted RF amplification,” *Optics Letters*, vol. 45, no. 6, pp. 1539-1542, Mar. 2020.
3. E. S. Lima, **R. M. Borges**, L. A. M. Pereira, H. R. D. Filgueiras, A. M. Alberti, Arismar Cerqueira S. Jr., “Multiband and photonicly amplified fiber-wireless Xhaul,” *IEEE Access*, vol. 8, pp. 44381-44390, Mar. 2020.
4. L. A. M. Pereira, C. H. S. Lopes, **R. M. Borges**, E. S. Lima, A. C. Ferreira, M. Abreu, L. L. Mendes, Arismar Cerqueira S. Jr., “Implementation of a multiband 5G NR fiber-wireless system using analog radio over fiber technology,” *Optics Communications*, vol. 474, May 2020.
5. **R. M. Borges**, L. A. M. Pereira, A. C. Ferreira, L. L. Mendes, D. H. Spadoti, Arismar Cerqueira S. Jr., “Fifth-generation new radio fiber-wireless system for long-reach and enhanced mobile broadband scenarios,” *Microwave and Optical Technology Letters*, Early view, Aug. 2020.
6. H. R. D. Filgueiras, **R. M. Borges**, M. C. Melo, T. H. Brandão, Arismar Cerqueira S. Jr., “Dual-band wireless fronthaul using a FSS-based focal-point/Cassegrain antenna assisted by an optical midhaul,” *IEEE Access*, vol. 7, pp. 112578-112587, Aug. 2019.
7. **R. M. Borges**, T. R. R. Marins, M. S. B. Cunha, H. R. D. Filgueiras, I. F. da Costa, R. N. da Silva, D. H. Spadoti, L. L. Mendes, Arismar Cerqueira S. Jr., “Integration of a GFDM-based 5G transceiver in a GPON using radio over fiber technology,” *Journal of Lightwave Technology*, vol. 36, no. 19, pp. 4468-4477, Oct. 2018.
8. D. F. Noque, **R. M. Borges**, A. L. M. Muniz, A. Bogoni, Arismar Cerqueira S. Jr., “Thermal and dynamic range characterization of a photonics-based RF amplifier,” *Optics Communications*, vol. 414, pp. 191-194, May 2018.
9. **R. M. Borges**, T. R. R. Marins, M. S. B. Cunha, D. H. Spadoti, L. L. Mendes, Arismar Cerqueira S. Jr., “Implementation of a multi-Gbit/s and GFDM-based optical-wireless 5G network,” *Journal of Microwaves, Optoelectronics and Electromagnetic Applications*, vol. 17, no. 4, pp. 579-589, Dec. 2018.

## Conferences:

10. **R. M. Borges**, L. A. M. Pereira, T. R. R. Marins, L. L. Mendes, D. H. Spadoti, Arismar Cerqueira S. Jr., “Sistema fibra/rádio com vazão de Gbit/s para aplicações 5G,” in *Proc. XXXVII Simpósio Brasileiro de Telecomunicações e Processamento de Sinais (SBrT)*, Petrópolis, RJ, Brazil, Oct. 2019.
11. **R. M. Borges**, T. R. R. Marins, M. S. B. Cunha, D. H. Spadoti, L. L. Mendes, Arismar Cerqueira S. Jr., “Transceptor GFDM integrado em sistema rádio sobre fibra para redes 5G,” in *Proc. 18º SBMO - Simpósio Brasileiro de Micro-ondas e Optoeletrônica e 13º CBMAG - Congresso Brasileiro de Eletromagnetismo (MOMAG)*, Santa Rita do Sapucaí, MG, Brazil, Aug. 2018.
12. M. S. B. Cunha, **R. M. Borges**, E. S. Lima, I. F. da Costa, Arismar Cerqueira S. Jr., “Sistema híbrido fibra/rádio baseado em GPON para redes 5G,” in *Proc. 18º SBMO - Simpósio Brasileiro de Micro-ondas e Optoeletrônica e 13º CBMAG - Congresso Brasileiro de Eletromagnetismo (MOMAG)*, Santa Rita do Sapucaí, MG, Brazil, Aug. 2018.
13. **R. M. Borges**, L. A. M. Pereira, T. R. R. Marins, D. H. Spadoti, L. L. Mendes, Arismar Cerqueira S. Jr., “Implementação de uma rede óptico-wireless baseada em GFDM para 5G,” in *Proc. 8º Conferência Nacional em Comunicações, Redes e Segurança da Informação (ENCOM)*, Salvador, BA, Brazil, Oct. 2018.

## **Awards**

1. The paper entitled “Transceptor GFDM integrado em sistema rádio sobre fibra para redes 5G,” received honorable mention in the research area on optics from MOMAG 2018.

# Contents

<b>1. Introduction</b> .....	<b>1</b>
1.1. Motivation.....	1
1.1.1. Emerging 5G networks.....	1
1.1.2. Microwave Photonics (MWP).....	5
1.2. State of the art .....	8
1.3. Goals and contributions .....	10
1.4. Thesis outline .....	13
<b>2. Technical background</b> .....	<b>14</b>
2.1. Passive optical network (PON).....	14
2.1.1. PON topologies and standards.....	15
2.1.2. WDM overlay .....	20
2.2. Radio Access Network (RAN).....	22
2.2.1. Distributed RAN (D-RAN) .....	23
2.2.2. Centralized RAN (C-RAN) .....	24
2.3. Mobile fronthaul .....	26
2.3.1. Digital RoF (D-RoF) .....	27
2.3.2. Analog RoF (A-RoF).....	30
2.4. The Intel's 5G Transceiver .....	33
2.4.1. Block diagram, operation principle and features.....	33
2.4.2. Performance from the waveform point-of-view .....	38
<b>3. RoF solutions for multi-band 5G systems</b> .....	<b>40</b>
3.1. The Mach-Zehnder modulator (MZM).....	41
3.2. RoF technique based on a single-drive MZM .....	45
3.3. RoF technique based on a dual-drive MZM .....	47
3.4. Performance analysis .....	48
3.4.1. Challenges and setup .....	48
3.4.2. Experimental results .....	50
<b>4. Implementation 1: Integration of the 5G transceiver in a WDM overlay system</b> .....	<b>52</b>
4.1. The proposed architecture.....	54
4.2. Experimental results .....	58
4.2.1. GFDM analysis.....	59
4.2.2. 26-GHz analysis .....	62
4.2.3. GPON analysis .....	65

<b>5. Implementation 2: DSP-based flexible-waveform and multi-application 5G fiber-wireless system</b> .....	<b>67</b>
5.1. The proposed architecture.....	69
5.2. Experimental results .....	73
5.2.1. 5G flexible waveform at 788 MHz: Long-reach .....	74
5.2.2. 5G NR at 3.5 GHz: Outdoor eMBB .....	75
5.2.3. 26-GHz femtocell: Indoor eMBB.....	78
5.2.4. M2M application .....	81
<b>6. Implementation 3: Multi-band 5G NR system with photonic-assisted RF amplification (PAA)</b> .....	<b>83</b>
6.1. Photonic-assisted RF amplification techniques .....	85
6.2. The proposed multi-band 5G NR system with PAA .....	87
6.3. Experimental results .....	90
<b>7. Final remarks</b> .....	<b>94</b>
7.1. Conclusions.....	94
7.2. Future works .....	97
<b>Appendix A</b> .....	<b>99</b>
<b>Appendix B</b> .....	<b>100</b>
<b>References</b> .....	<b>102</b>

# 1. Introduction

This Chapter presents a general overview of this academic research. Section 1.1 introduces the work motivation. Section 1.2 discusses the state of the art on the subject of study. Section 1.3 highlights the research focus and contributions. Section 1.4 reports the structure of this thesis.

## 1.1. Motivation

### 1.1.1. Emerging 5G networks

The fifth-generation (5G) of wireless networks is expected to be a remarkable mobile broadband evolution within the scope of International Mobile Telecommunications (IMT) for 2020 and beyond. In short, 5G shall support 1000-fold gains in data volume and number of connected devices over the fourth-generation (4G), as well as 100-fold higher user data rate, 10 times longer battery life and 5 times reduced end-to-end latency [1]. Moreover, 5G emerges as an enabler of a fully-connected society and will create an open ecosystem for innovation, since it is predicted to deal with new value-added services and applications. Key usage scenarios defined by the International Telecommunication Union Radiocommunication Sector (ITU-R) include [2]:

- Enhanced mobile broadband (eMBB), focused on Gbit/s individual user experience as an opportunity to launch innumerable human-centric services, such as extensive multimedia access and virtual reality;
- Massive machine type communications (mMTC), which cover billions of connections from the narrowband Internet of things (NB-IoT) capabilities;
- Ultra-reliable and low latency communications (URLLC), for tactile Internet and mission critical cases, such as self-driving cars, Industry 4.0, health care and control of unmanned aerial vehicle.

In addition, extreme long range coverage (up to 100 km) appears as an important usage case, which focuses on remote or rural access for connecting the large offline populations and enabling new opportunities, such as environmental control, smart farms and

IoT-based agribusiness [3]. High mobility wireless communications (up to 500 km/h) also rise with particular interest to enable satisfactory connectivity in high-speed trains [2].

According to the standardization-related groups and research institutes in the field of 5G, each envisaged scenario demands particular and challenging requirements, which also depends on the deployment case [4-8]. For instance, indoor eMBB claims to user experienced data rates of 1 Gbit/s and 500 Mbit/s for downlink (DL) and uplink (UL), respectively. The eMBB throughput target even assumes 300 Mbit/s DL and 50 Mbit/s UL for dense urban deployment cases, as well as 50 Mbit/s DL and 25 Mbit/s UL for urban macro applications [4, 5]. On the other hand, the general mMTC case requires continuous low data rates experience between devices, e.g. from 10 kbit/s to 10 Mbit/s, whereas end-to-end latency becomes crucial and must not exceed 1 ms for URLLC with 99.999% of reliability [6-8]. Assuming extreme long range coverage in low density areas (up to 2 user/km<sup>2</sup>), the target is a minimum user throughput of 1 Mbit/s on DL and 100 kbit/s on UL at the cell edge, which can reach 100 km distance. High-speed mobility claims to 50 Mbit/s DL and 25 Mbit/s UL up to 500 km/h [4].

As a consequence, 5G networks must have a flexible physical layer (5G PHY) for multi-service IMT systems based on a broad variety of capabilities [9]. 5G must support multiple radio access technologies, efficient spectrum usage plan, dynamic allocation of radio resources and interoperability with standardized legacy systems. Due to these all reasons, it is required the use of innovative technical solutions, including: 5G new radio (NR), additional spectrum bands, software defined network (SDN), virtualization, network slicing, massive multiple input multiple output (MIMO) and multi-antenna beamforming [5, 10]. Figure 1.1 summarizes the discussed 5G scenarios and requirements.

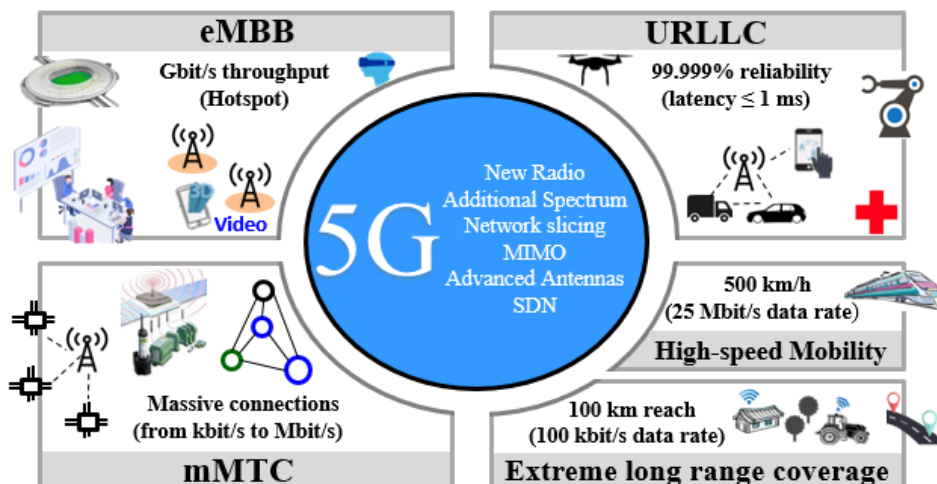


Figure 1.1 – 5G general scenarios and requirements. Adapted from [10].

One of the 5G NR most important innovation refers to the multiplexing technique used, since it affects the resulting transmit spectrum and, consequently, the coexistence with other communication systems. A notable drawback from the Orthogonal Frequency Division Multiplexing (OFDM), typically employed for 4G, is the difficulty of achieving the desirable signal confinement into the spectrum. Therefore, diverse waveforms based on multicarrier transmission and spectral confinement techniques, e.g. filtering, have been presented in the literature as promising for 5G [11-15].

Filterbank Multicarrier (FBMC) enables high spectral efficiency and very low out-of-band emission (OOBE), typically more than 50 dB below from that obtained with OFDM, assuming the baseband signal form [13, 14]. However, FBMC might not be attractive for short burst data transmission from NB-IoT applications, once the employed digital filtering causes a signaling overhead during that no useful data is transmitted. This overhead can significantly extend the burst length, becoming a drawback in the context of short package transmission [16]. Filtered Orthogonal Frequency Division Multiplexing (F-OFDM) relies on subcarrier-based filtering and can also enable very low OOBE [14]. The use of one cyclic prefix (CP) per block makes F-OFDM robust for intersymbol interference in multipath channels, but reduces the spectrum efficiency especially when short symbols are required [17]. Universal Filtered Multi-Carrier (UFMC), also known as Universal Filtered Orthogonal Frequency Multiplexing (UF-OFDM), is another OFDM-based waveform that benefits from a filtering technique to provide attractive OOBE [13]. However, UFMC does not use CP and then is more sensitive to time misalignments, resulting in performance loss even when small time synchronization errors occur [18]. Generalized Frequency Division Multiplexing (GFDM) also employs subcarrier-based filtering and performs a signal smoothing in the time domain to reduce OOBE. This non-orthogonal waveform has been shown potential to achieve a trade-off between flexibility, performance and complexity [19, 20]. The flexibility comes from the GFDM capability of addressing other waveforms as alternative cases, whereas performance regards the GFDM higher spectral efficiency and approximately 20 dB lower OOBE compared to OFDM. On the other hand, GFDM brings complexity because it is a generalized non-orthogonal waveform [11].

Among the discussed and other 5G candidate waveforms, CP-based OFDM (CP-OFDM) including the optional addition of filtering, e.g. F-OFDM, has been recently specified by the 3rd Generation Partnership Project (3GPP) for the next generation wireless networks [21]. One of the reasons for this decision is the CP-OFDM compatibility with the 4G systems, added to the low out-of-band emission characteristic in case of using F-OFDM.

Regarding frequency spectrum, 5G networks are likely to operate in at least two distinct bands [22-24]. The first one is above 6 GHz, including millimeter-waves (mm-waves), in which there are unexploited frequencies and a large amount of available bandwidth (BW). For instance, carrier frequencies around 30 GHz with BW of up to 1 GHz can be used for covering eMBB applications [5]. The W-band (75-110 GHz) has also been considered for satisfying the challenging requirements of this new generation, despite suffering from higher free-space loss, high complexity and manufacturing costs [25]. A second 5G band comprises carrier frequencies between 1 and 6 GHz with BW of up to 200 MHz toward cellular, mMTC and URLL applications, in such way the 5G services should coexist with consolidated technologies at this frequency range. In parallel, carrier frequencies below 1 GHz, e.g. around 700 MHz, might also be used as the third and lowest 5G band for enabling low-bandwidth (maximum of 20 MHz) long range applications, which is also expected to coexist with Long Term Evolution (LTE) and digital television (TV) services [5]. These bands have been included in the recent launched 5G NR standard as frequency range 1 (FR1: 0.45 – 6.00 GHz) and frequency range 2 (FR2: 24.25 – 52.60 GHz), with a set of bandwidth options [26]. In Brazil, the National Telecommunications Agency (Anatel – Agência Nacional de Telecomunicações) has evaluated the bands of 2.3 and 3.5 GHz, as well as the frequency range from 24.25 to 27.50 GHz and beyond for the 5G purpose [24].

The envisaged association of the 5G bands for covering several applications requires a considerable expansion in the current mobile networks, in such way trends on network planning point out to optical-wireless convergence [27] and mobile dense heterogeneous networks (HetNet) [28]. HetNet consists of a mix of cell sizes with multiple radio access technologies, and can employ super or macrocells overlay and smaller cells (pico, micro and femtocells) underlay toward user equipment experience continuity. It is worth mentioning that the supercell concept refers to a coverage area that extends the macrocell range and adheres the 3GPP scenario for extreme long-range coverage [29]. In parallel, 5G radio access network (RAN) should evolve and shows a promising direction to be primarily centralized due to the imminent increase in the number of base stations (BS) [30].

As will be discussed on Chapter 2, centralized RAN (C-RAN) brings advantages over distributed RAN (D-RAN), which physically locate the baseband unit (BBU) with the remote radio unit (RRU) in the traditional base station. C-RAN, on the other hand, consists of keeping RRU close to the antenna and displacing BBUs from remote cell sites to a unified central unit (CU), giving rise to the BBU pool concept. On C-RAN, CU can connect RRU by using a physical link known as fronthaul (FH), or employing an optical midhaul (MH) up to a

distribution unit (DU) followed by the FH, which can be optical or wireless despite it is mostly based on single mode fiber (SMF). The fronthaul and midhaul transport networks compose then the next generation fronthaul interface (NGFI), in which the 5G base station is also called gNodeB and it can include RRU, DU and CU entities [30].

NGFI is part of the 5G X-haul vision, illustrated in Figure 1.2. It integrates backhaul (BH) and fronthaul into a common physical architecture supporting transport and access, as well as flexible functional splits [27, 30]. Therefore, 5G might benefit from quick communication between co-located baseband units, management and energy efficiency, non impracticable site costs, scalability and agile deployment time, besides the advantages from optical communications that are going to be discussed in the next subsection.

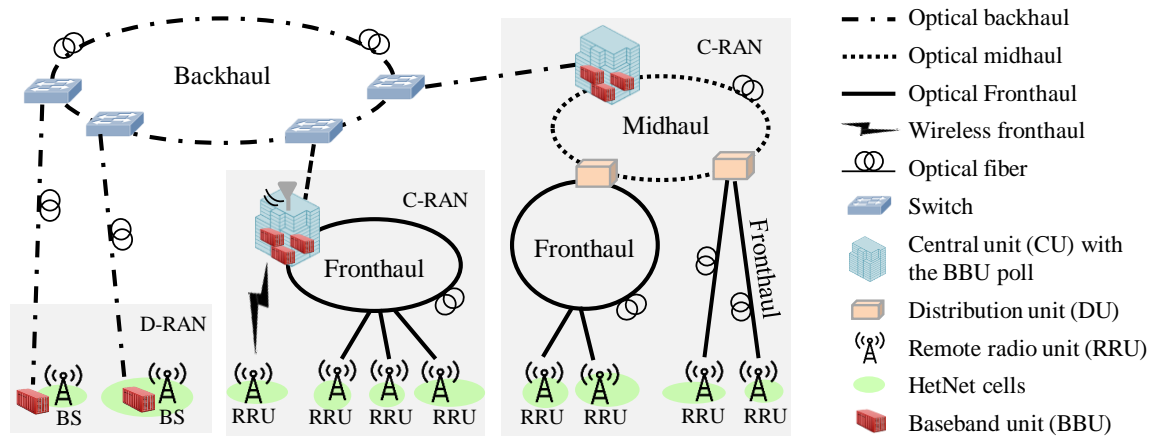


Figure 1.2 – 5G X-haul vision regarding the physical architecture. Adapted from [30].

### 1.1.2. Microwave Photonics (MWP)

Microwave photonics (MWP) can be defined as an interdisciplinary area that deals with the interaction between microwave and optical signals by combining optoelectronics and radiofrequency (RF) engineering. It has been explored for a wide range of applications, such as broadband wireless access networks, instrumentation, radar, satellite communications, remote sensing and warfare systems [31]. MWP benefits from unique advantages of photonics—including wide bandwidth, electromagnetic interference (EMI) immunity and extremely high frequency flexibility—to upgrade microwave systems. One of the MWP aims is using optical techniques for providing functionalities that are very complex or even impossible to carry out directly with conventional electronics [32].

The MWP major functions are the following ones: generation, processing and distribution of RF, microwaves and mm-waves signals [31]. As the carrier frequency increases, these tasks become more and more challenging in the electrical domain, because of severe propagation losses and electronics-based hardware limitations. The last ones are related to the typical narrow bandwidth and frequency response of electronic components, which restrict digital signal processing to few GHz and make necessary the use of some specific hardware for each communication mobile standard. Additional limitation issues from conventional electronics include stability and phase noise, since the mm-waves generation and detection commonly require diverse stages of upconversion and downconversion, respectively. Stability can be especially impaired due to the EMI sensitivity.

Photonics technological maturity on microwave generation and processing in fact has led to proposals of photonic-assisted analog-to-digital converters (ADC) [33], filters [34], phase-shifters [35], true-time delay beamforming and RF front-ends [31, 36], which include tunable and broadband RF converters [37]. Frequency-agile photonics-based RF transceivers have also been demonstrated for radar and wireless communication purposes [38, 39]. In parallel, photonics technology for distributing RF signals via fiber-optic links gave rise to the radio over fiber (RoF) systems [40]. RoF systems take advantages of optical communications, such as high capacity, EMI immunity, unlicensed optical spectrum and low and fixed propagation losses ( $\approx 0.2$  dB/km at 1550 nm with today's SMF) regardless the operational radio frequency [41]. When transmitting microwaves or mm-waves through coaxial RF lines or wireless channels instead, propagation losses increase significantly and can make the transport network prohibitive. As an example, SUCOFLEX<sup>®</sup>329 microwave cable imposes losses of 31.3 dB/km at 26 GHz [42], whereas Friis formula indicates a free space attenuation of 120.74 dB after 1 km wireless transmission in line of sight (LOS) at this frequency [43].

RoF systems can use analog (A-RoF) or digital radio over fiber (D-RoF) schemes, both requiring transmitter and receiver, besides a careful planning with technical issues to be overcome. In short, the transmitter essentially associates the light source and the electrical-to-optical (E/O) conversion, whereas the receiver employs at least a photodetector (PD) for performing the reverse processes, typically followed by electrical amplifiers (EAs). From this concept, different techniques can be applied in the RoF link design for achieving a trade-off between cost and performance [44]. Despite D-RoF is the main available fronthaul solution today, it may not be suitable for the strict 5G requirements. On the other hand, A-RoF topologies are gradually becoming attractive as the industry begins to deploy mm-waves

access services and scalable 5G networks [45]. The aspects of future mobile fronthaul based on A-RoF and D-RoF schemes will be discussed on Chapter 2.

The RoF applications have been increased over the years. A RoF link was first demonstrated by Stephens et al. [46] and proposed in a telecommunications context for the provision of second generation cordless telephony services in the access network [47]. During the same era, mm-waves transmission using optical fiber started to be investigated for video services remote delivering purposes [48]. Since then, RoF techniques have been exploited to favor distributed antenna systems (DAS) of multiple radio access technologies, such as universal mobile telecommunications system (UMTS), wireless fidelity (Wi-Fi) and LTE [49-52]. RoF-based DAS enabled to increase and/or provide relatively uniform mobile coverage over large areas and spaces where it is not convenient to add base stations, e.g. buildings, public centers, rails and winding tunnels. The possibility of achieving operational flexibility and cost savings even stimulated RoF modules design to the point where a number of products were available in the market [53, 54].

With the mobile communications diffusion and consequent demand for spectrum, RoF links have also been widely explored for distributing mm-waves, especially in the Ka (27-40 GHz), W (75-110 GHz) and unlicensed 60 GHz bands. This task has commonly been unified with photonics-based RF upconversion and downconversion approaches, enabling ultra-wideband wireless applications [55-59]. Moreover, RoF links based on RF signal digitization were introduced as a strategy to avoid impairments from mm-waves over fiber, e.g. dispersion-induced power fading, and have gained popularity for the 4G cellular systems with adoption of the Common Public Radio Interface (CPRI) standard [44, 60].

In the 5G context, MWP has been recognized as a key area of study to simplify the radio access networks by taking advantages of optical and mobile communications. Whereas photonics-based RF generation and processing can overcome the electronics-based hardware limitations of high frequency wireless systems, RoF technology can enable fiber-wireless (FiWi) communications to maximize coverage. For instance, RoF-based FiWi systems can provide high capacity fronthaul links for mm-waves femtocells, thus extending the distance between central stations and wireless end-users. Besides favoring C-RAN and simplifying RRU, the RoF technology can also be used for jointly transporting RF signals at different frequency bands through the same optical infrastructure. In this way, it is expected to take advantage of the passive optical network (PON) solutions for distributing them, promoting multi 5G applications in broadband wireless systems [45, 61].

## 1.2. State of the art

Academia and telecommunication companies/organizations are continuously working on new technologies for 5G core, metro and access networks. Core and metro networks deal with dense traffic connections between cities and local regions, whereas access networks compose the last mile links between service providers and the end user. As stated earlier, the radio access networks from mobile systems should evolve toward the next generation fronthaul interface, which can integrate optical fiber and wireless links using RoF technology. In this way, the current section reports the state of the art on RoF solutions for 5G, assuming four specific architectures:

- Analog RoF, supporting the transmission of analog RF signals as little processing as possible;
- Digital RoF, in which the RF signals are digitized to the fiber-optic transmission;
- Fiber-wireless, i.e. an architecture that adds wireless transmission to the RoF configuration;
- RoF in conjunction of PONs, in which the optical access infrastructure is exploited not only for wired services, but also for mobile fronthaul applications.

Analog RoF architectures have been successfully exploited to distribute 5G candidate waveforms through the fronthaul links [62-65]. For instance, GFDM and multi-Gbit/s FBMC transmission over SMF were reported in [62] and [63], respectively. Both works employed an external modulation technique based on a single-drive Mach-Zehnder modulator (SD-MZM). On the other hand, Kim et al. made use of directly (DMLs) and electroabsorption modulated lasers (EMLs) to transmit 100-MHz bandwidth F-OFDM signals in a RoF-based 20-km mobile fronthaul [64], whereas Delmade et al. employed direct modulation for distributing OFDM, GFDM and UF-OFDM signals in an optical link with 4G and 5G coexistence [65].

An additional topic on A-RoF architectures that has triggered interest is the use of digital signal processing (DSP) for compensating transmission impairments and linearizing the link [66, 67]. A recent applicability was demonstrated by Noweir et al., which applied digital pre-distortion (DPD) in a 24-GHz RoF system to reduce the error vector magnitude (EVM) at the photodetector output [67]. Moreover, progress on A-RoF links has indicated the possibility of simultaneously providing multiple services, at distinct frequency bands, using a single light source [68-71]. Pan and Yao addressed baseband and ultra-wideband (UWB)

applications [69], whereas Ho et al. exploited RoF, fiber-to-the-x (FTTx) and cable television (CATV) services [70]. In [71], the authors reported a simultaneously distribution of distinct wireless standards, including Digital Video Broadcasting-Terrestrial (DVB-T), Worldwide Interoperability for Microwave Access (WiMax) and LTE.

Advances on the second architecture considered in this discussion, digital RoF, include the possibility of implementing functional split and data compression options assisted by DSP [72, 74]. A study regarding these D-RoF tasks was presented in detail in Santos' thesis [72], which investigated eight split options between cloud center and RRU, as well as the EVM performance as a function of different compression factors. The functional split concept even contributed to the enhanced Common Public Radio Interface (eCPRI) design, toward a packetized and flexible D-RoF-based fronthaul link [75].

Regarding the fiber-wireless architectures, they have incorporated new waveforms and a set of techniques for improving wireless capacity and mobile coverage [76-82]. MIMO was implemented in [77] as 5G technical solution for extending the wireless link after 2.2 km fiber-optic transmission. Li et al. exploited 6 GHz bandwidth in the mm-waves band for implementing a 24 Gbit/s FiWi link with up to 4 m wireless range [78]. Mobile 4K video services at 28 GHz were demonstrated by taking advantage of sub-bands allocation, intermediate frequency over fiber (IFoF) and beamforming antenna [79]. Additionally, Argyris et al. reported 24 Gbit/s throughput in an IFoF/mm-wave link with electrical subcarrier multiplexing [80], and Morant et al. exploited a mm-wave photonic beamforming system for reaching 21 Gbit/s as data rate for 5G New Radio [81]. A large-capacity (>100 Gbit/s) photonics-aided mm-wave communication was reported in [82], in which the authors exploited the following kinds of techniques: MIMO; multi-level vector modulation; electrical and optical multicarrier multiplexing; multi-band allocation, including mm-waves; large-gain/high-power RF electrical amplifiers; large-gain small-beamwidth Cassegrain antenna; DSP-based heterodyne coherent detection.

The last architecture under discussion, RoF in conjunction of passive optical networks, has been shown attractive for enabling a unified point-to-multipoint (P2MP) transport system, capable of supporting baseband triple-play (voice/data/video) services and 5G applications [83-89]. As will be discussed latter, PON has evolved driven mainly by the broadband wired demands and can be divided into three types [72], namely: time division multiplexing PON (TDM-PON); time and wavelength division multiplexing PON (TWDM-PON); wavelength division multiplexing PON (WDM-PON). A successful field trial exploiting WDM-PON for connecting BBUs and RRUs in the 5G context was reported in [83], resulting in a flexible

fronthaul with CPRI data transmission. Furthermore, Liu et al. presented a schematic in which multiple RF signals are simultaneously transmitted after being intensity modulated onto a different wavelength by of-the-shelf transceivers [61], and Souza and Romero proposed a bidirectional self-seeding WDM-PON, even with carrier remodulation scheme, as an alternative for supporting RoF-based fronthauls [86]. Another important solution is using WDM overlay, i.e. PON topologies with RF overlay at an additional wavelength [87-89], representing a simple and agile way of integrating RoF technology in the existent FTTx infrastructure. A set of WDM overlay schemes on top of TWDM-PON for converged broadband services were reported in [88]. Additionally, Shahpari et al. proposed a coexistence scenario in which RF overlay and legacy PON standards are integrated toward future optical access networks (F-OANs) [89].

### 1.3. Goals and contributions

The aim of this research is presenting analog RoF solutions for multi-band 5G systems and experimentally demonstrating application cases in accordance with the C-RAN concept. The PON capillarity will be exploited as transport network to diverse RF signals. Our target is addressing 5G emerging usage cases by associating the predicted 5G bands, e.g. 700 MHz, 3.5 GHz and 26 GHz, in the proposed fronthaul architecture without requiring multiple lasers (LDs) and electro-optic modulators. The fiber-wireless transmission and analysis of the promising GFDM and F-OFDM signals, as well as the 5G NR standard in microwaves and mm-waves, supplement the research focus. The work main contributions can be listed as follows:

- Employment of a dual-drive Mach-Zehnder modulator (DD-MZM) for simultaneous modulating an optical carrier with the lower and higher frequency RF-driven signals of future 5G networks, thus mitigating interferences between them;
- Integration of a DSP-based flexible-waveform RF transceiver, developed by our group and called 5G transceiver, in the proposed RoF-based fronthaul solution. The innovative radio equipment was designed at Inatel (National Institute of Telecommunications) for contributing to the fifth-generation, specially addressing remote and rural mobile access.

- Deployment of a multi-band FiWi system, capable of providing macrocells and high-throughput indoor femtocells, as well as addressing 5G, machine-to-machine (M2M) and fiber-to-the-home (FTTH) applications;
- Using digital pre-distortion for linearizing the RoF link, especially at 26 GHz carrier frequency with bandwidth of up to 800 MHz;
- FiWi transmission of the 5G NR standard in accordance with the 3GPP Release 15 [90], at 3.5 GHz and 26 GHz.
- System performance analysis by taking into consideration the coexistence among the distinct applications, as well as the 3GPP EVM requirements for 5G NR [91];
- Proposal and implementation of a multi-band 5G NR system with photonic-assisted RF amplification (PAA).

Table 1.1 summarizes the state of the art on RoF solutions compared to the current work, with the aim of highlighting our contributions. Despite the fact that FTTH and RoF-based multi-services have already been jointly employed in literature, we innovate on experimentally demonstrating multi-band Gbit/s RoF and FiWi transmission using a single distributed-feedback (DFB) laser and DD-MZM as RoF transmitter. We also innovate on addressing 5G predicted bands, using the GFDM and F-OFDM waveforms in a real-time flexible way, and employing the 5G NR standard in microwaves and mm-waves. Compared to previous works as [67, 80], we have applied DPD in the 26 GHz band and analyzed the system performance as a function of root mean square (RMS) EVM in accordance with the 3GPP requirements for 5G NR. To the best of our knowledge, we report the first implementation of a FiWi system including the transmission and analysis of the 5G NR standard, in accordance with the 3GPP Release 15 at 26 GHz. Additionally, we introduce the concept and report the implementation of a multi-band and photonicly amplified 5G NR system. The latter one takes advantage of a novel PAA technique allowing straightforward integration with the transport network.

Table 1.1 – State of the art on RoF solutions for 5G.

Ref.	Architecture	Application	Modulation/ Waveform	RF bands	RoF TX	DSP use
[63]	- A-RoF	- 5G	- FBMC	- 53 GHz	- DFB LDs + single-drive intensity modulator	- Equalization
[64]	- A-RoF	- 5G	- F-OFDM	- 2.7 GHz	- DMLs - EMLs	- F-OFDM generation and detection
[65]	- A-RoF	- 4G - 5G	- OFDM - GFDM - UF-OFDM	- 1.5 GHz	- DML	- Not applied
[67]	- A-RoF	- LTE - 5G	- Standard LTE	- 24 GHz	- DFB LD + SD-MZM	- DPD
[69]	- A-RoF	- FTTH - UWB service	- Phase shift keying (PSK) - On-off keying (OOK)	- 0-3.1 GHz - 3.1-10.6 GHz	LD + SD-MZM + electrical combiner	- Not applied
[70]	- A-RoF	- FTTH - CATV - RF distribution	- Amplitude shift keying (ASK)	- Baseband - 6 GHz	DFB LD + 2 external modulators	- Not applied
[72]	- D-RoF	- LTE - 5G	- OFDM	- Baseband	- DML	- Functional split and data compression
[73]	- D-RoF	- 5G	- Pulse amplitude modulation (PAM)	- Baseband	- DML	- Data Compression - CPRI and eCPRI supporting
[74]	- D-RoF	- 5G	- Quadrature PSK (QPSK) - 16- to 1024-quadrature amplitude modulation (QAM)	- Up to 4 GHz	- External cavity laser (ECL) + DFB laser + SD-MZM	- Data compression
[75]	- D-RoF	- 5G	- SC-FDM - QAM	- Baseband	- DML	- Adaptive quantization - eCPRI detection
[76]	- FiWi	- 5G	- F-OFDM	- 6 GHz	- DFB LD + SD-MZM	- F-OFDM generation and detection
[77]	- FiWi	- 5G	- OFDM	- 60 GHz	- 2 directly modulated DFB LD	- MIMO
[78]	- FiWi	- RF transmission	- OFDM	- 57 GHz - 91 GHz	- ECL + in-phase and quadrature (IQ)-MZM	- Not applied
[80]	- FiWi	- 5G	- QPSK - 16-QAM	- 57-64 GHz	DFB LD + SD-MZM	- DPD
[81]	- FiWi	- 5G	- 16-, 32- 64- and 128-QAM	- 17.6 GHz - 26 GHz	- DFB LD + SD-MZM + optical ring resonators	- Not applied
[82]	- FiWi	- 5G	- OFDM	- 26 GHz - 40 GHz - 90 GHz	- Non-specified	- Coherent detection
[61]	RoF + PON (WDM-PON)	- TV - WiMax - Wireless Fidelity (WiFi)	- Standard WiFi - Analog TV	- 2.4 GHz - 60 GHz	- Multiple off-the-shelf transceivers	- Not applied
[83]	- RoF + PON (WDM-PON)	- 5G	- OFDM	- LTE band	- Non-specified	- Not applied
[84]	- RoF + PON (WDM-PON)	- 5G	- F-OFDM	- Up to 3 GHz	- directly modulated distributed Bragg reflector laser	- F-OFDM generation and detection
[85]	- RoF + PON (GPON/EPON)	- 4G - 5G	- OFDM	- Baseband - LTE channels	- DFB LD + SD-MZMs + electrical combiner	- Signal generation and detection
[89]	- RoF + PON (WDM overlay)	- F-OAN	- Differential QPSK (DQPSK)	- 47-820 MHz - 0.95-2.15 GHz	- ECL + IQ modulator + MZM	- DQPSK modulation and demodulation
This work	- FiWi + PON (WDM overlay) + PAA	- 5G - FTTH - M2M	- OFDM - GFDM - F-OFDM - 16- and 64 QAM - Standard 5G NR	- Baseband - 700 MHz - 3.5 GHz - 26 GHz	- DFB LD + DD-MZM	- DPD - Flexible-waveform generation and detection

## **1.4. Thesis outline**

This thesis is structured in seven chapters. Chapter 2 presents the technical background necessary for the understanding of this thesis. It includes discussions regarding passive optical networks, radio access networks and mobile fronthaul. Additionally, Chapter 2 describes the Intel's 5G transceiver employed in the experiments. Chapter 3 reports an experimental study of analog RoF techniques based on SD-MZM and DD-MZM for supporting mobile fronthauls. Afterwards, three multi-band RoF-based 5G systems are implemented. Chapter 4 presents the integration of the 5G transceiver in a WDM overlay system. Chapter 5 refers to a DSP-based flexible-waveform and multi-application 5G FiWi system. Chapter 6 presents a multi-band 5G NR system with photonic-assisted RF amplification. Finally, the conclusions and future works are commented in Chapter 7.

## 2. Technical background

This Chapter is structured in four sections. Section 2.1 reports the different passive optical network topologies and standards. Section 2.2 deals with distributed and centralized radio access networks. Section 2.3 regards the mobile fronthaul based on digital and analog radio over fiber technology. Section 2.4 describes the 5G transceiver, including its block diagram, features and performance from the waveform point-of-view.

### 2.1. Passive optical network (PON)

With the increasing demand for broadband access, optical fibers started to get progressively closer to the end user, giving rise to the optical access networks. Driven mainly by the world wide web-related opportunities, Internet providers extended their services to the so called Fiber-To-The-x (FTTx), where x can mean home (FTTH), building (FTTB), cabinet (FTTC), etc. To implement such connections, the companies developed a series of standards based on a point-to-multipoint network with no active elements between the service provider and the distribution facility or end user. This kind of architecture leads to the passive optical network (PON) concept.

Figure 2.1 reports the structure of a generic PON, which is composed of three main parts as follows:

- Optical line terminal (OLT), placed at the central office (CO) to provide the interface between backbone network and PON. OLT contains the transceivers and the active modules. Examples of these elements are the Fiberlink 20028 OLT from Parks [92] and KTS 2110+ small form-factor pluggable (SFP) transceiver from Intelbras [93];
- Optical network unit (ONU), a transceiver located either at the distribution facility or close to the end user. Beyond this point the service can be delivered by metallic cables. The Fiberlink 4100 product from Parks [94] is an example of ONU;
- Optical distribution network (ODN), connecting OLT and ONUs. ODN includes the remote node (RN), which contains the passive optical splitter/combiner for distributing and collecting the user's signals. A feeder fiber connects CO to RN, whereas the distribution fibers connect RN to ONU.

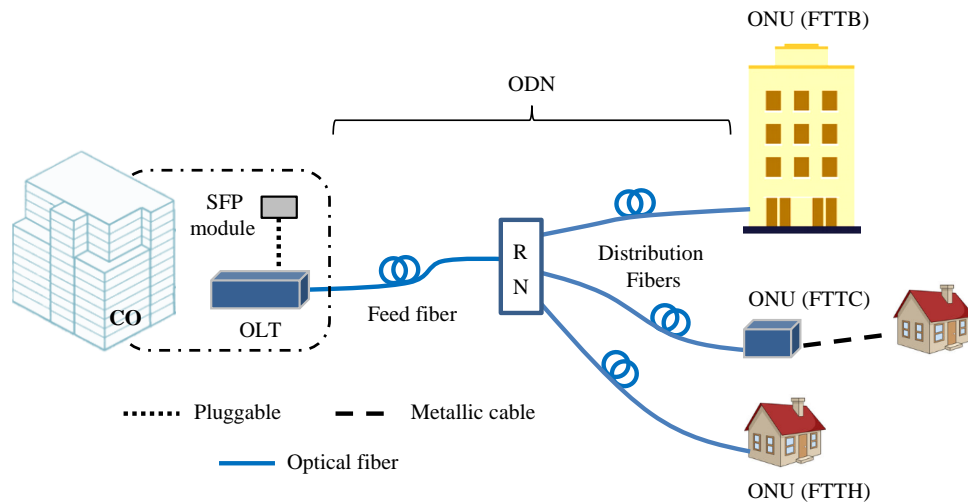


Figure 2.1 – Structure of a generic PON: CO - central office; OLT - optical line terminal; SFP - small form-factor pluggable; RN - remote node; ONU - optical network unit.

### 2.1.1. PON topologies and standards

Passive optical networks have three main topologies according with the sharing resources technique, which is required due to the P2MP transmission. The most commonly implemented topology is TDM-PON, depicted in Figure 2.2. TDM-PON uses time division multiplexing for data multiplexing and coarse wavelength division multiplexing (CWDM) to separate upstream and downstream. The latter one occurs on broadcast, i.e. OLT sends the information to all ONUs through the power splitter. Each ONU opens then only their addressed packages and, for upstream, sends data to OLT on specific time slots. The synchronization process is provided by OLT and a single pair of wavelengths ( $\lambda_1$  and  $\lambda_2$ ) is shared in such topology.

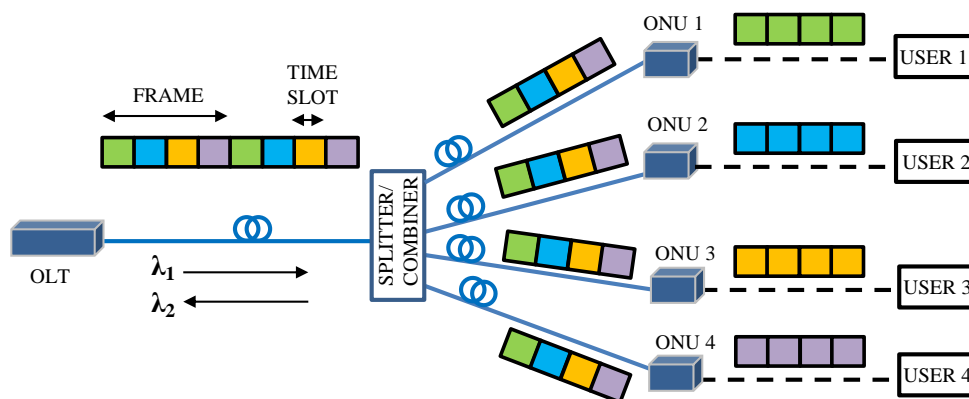


Figure 2.2 – Basic TDM-PON topology. Adapted from [72].

TDM-PON is a solution for different PON standards defined by the International Telecommunication Union Standardization Sector (ITU-T) and Institute of Electrical and Electronics Engineers (IEEE), with support of the Full Service Access Network (FSAN) group. Initially, ITU-T launched the Asynchronous Transfer Mode PON (ATM-PON), which was redesigned as Broadband PON (BPON) [95]. This specification addressed mainly residential services, allowing 155.52, 622.08 and 1244.16 Mbit/s nominal data rates. Next, ITU-T defined the G.984.x series, known as Gigabit PON (GPON) [96]. Such standard covers business and residential applications with 2.4 Gbit/s downstream and 1.2 or 2.4 Gbit/s upstream data rates. While GPON was diffused in America and Europe countries, Japan and South Korea implemented the IEEE802.3ah or Ethernet PON (EPON) [97], specified by IEEE and capable of providing a symmetric 1.25 Gbit/s uplink and downlink data rate. To increase the capacity, IEEE802.3av task force standardized a 10G-EPON technology, which offers symmetric 10 Gbit/s or asymmetric 10 and 1 Gbit/s downstream and upstream, respectively [98]. With the same goal, ITU-T concentrated in upgrading GPON toward the next generation passive optical network phase one (NG-PON1). As a result, ITU-T specified the G.987.x series, including XG-PON1 with 10 Gbit/s on downstream and 2.5 Gbit/s on upstream, as well as the XG-PON2 with 10 Gbit/s data rate for both downlink and uplink [99].

From the information above, one can consider TDM-PON cost-effective, working with several PON standards and offering data rates up to 10 Gbit/s with 20-km reach. Drawbacks are associated to the throughput, latency and scalability limitations, since it is necessary to share the overall bandwidth by all users and wait a number of costumers send their packets.

The second PON topology, TWDM-PON, uses both time and wavelength division multiplexing. Figure 2.3 shows the basic TWDM system, in which distinct wavelengths coexist in the optical distribution network with WDM, and each wavelength serves multiple optical network units with TDM. For downstream, the wavelengths from the OLT reach the power splitter and all ONUs, which selectively receive a single channel using a tunable receiver. For upstream, each ONU group transmits on one of the upstream wavelengths. It is used a number of 4 to 8 TWDM channel pairs, each one comprising a downstream and upstream wavelength channel. As an example, 4x10 Gbit/s WDM channels can run in the same ODN and be divided in time to each customer.

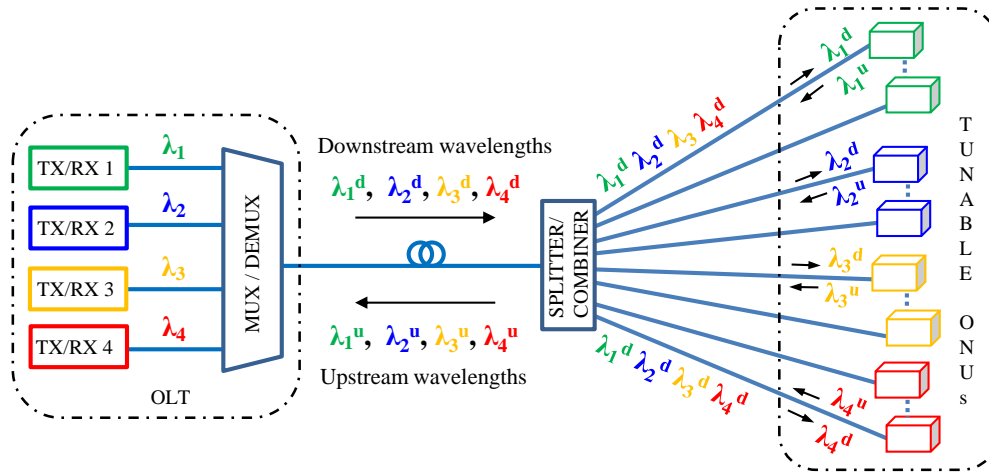


Figure 2.3 – Basic TWDM-PON topology. Adapted from [88].

TWDM-PON was chosen as topology for the next generation passive optical network phase two (NG-PON2), standardized by the ITU-T recommendation G.989 [100]. This standard is available with symmetric 40 Gbit/s throughput or asymmetric data rates, i.e. 40 Gbit/s in downstream direction and 10 Gbit/s in upstream direction, maintaining the capability of coexisting with legacy PON systems. Despite TWDM-PON increases the network capacity and scalability, even meeting the maximum CPRI data rate ( $\approx 24.3$  Gbit/s) from D-RoF links, it can be considered a medium to long-term solution because the required tunable optics is expensive and the synchronization-associated latency is still a challenge for C-RAN applications. Moreover, providers must prepare to deal with a large number of devices on inventory and network management.

The third PON topology is known as WDM-PON and provides dedicated wavelength for each ONU in order to significantly increase their available bandwidth. Figure 2.4 illustrates such solution assuming  $n$  as the number of users, which corresponds to the number of transmitters (TX) and receivers (RX) in both OLT and ONUs sides. In downstream direction, the different wavelengths are multiplexed to a common port at OLT using a multiplexer (MUX), typically based on arrayed waveguide grating. The optical signals share then the optical distribution network and each channel is directed to the respective ONU, after being filtered by a demultiplexer (DEMUX) at the remote node. For the upstream, the optical signal from each user goes through the reverse path using the same downstream wavelength or a different optical band. It is worth mentioning the fiber sharing method under discussion can be classified as CWDM or dense WDM (DWDM), depending on the wavelength grid used. This grid denotes central wavelengths that may be assigned with sufficient separation in a set of applications [101, 102].

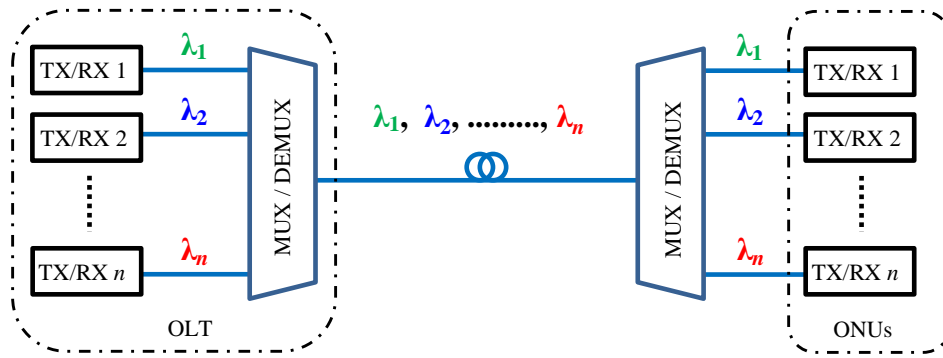


Figure 2.4 – Basic WDM-PON topology.

WDM-PON was considered in the development of NG-PON2, which focus on further increasing the user data rates, as well as enabling easy scalability and supporting 5G-demanded C-RAN resources [103]. Such topology is also studied by the IEEE P802.3ca task force on the standardization of 25, 50, and 100G EPON [104]. Additionally, the still hypothetical third phase of NG-PON (NG-PON3) considers a variety of technological options and WDM-PON is one of them [105]. Indeed, WDM-PON can provide very high throughput, reduced latency, extended physical reach and adaptability, but at a cost of requiring different TXs/RXs for each wavelength, resulting in possible inventory and operational costs increase. Therefore, there are many researches concerning how WDM-PON may be effectively implemented, e.g. employing tunable lasers, spectral slicing or self-seeding with wavelength reuse [86, 103]. These technical solutions compose colorless sources, which are optical devices that use the same hardware to provide any wavelength in a given range [86]. Hence, a single transmitter model might be employed for all users regardless of their operation channel.

Completing the PON standards overview, it is worth mentioning that IEEE P802.3cs task force and ITU-T Q2/SG15 study group are designing the “Super-PON”, an innovative architecture to scale optical access networks up to 50-km reach, expand customer coverage per fiber and provide central office consolidation. Super-PON is planned to achieve these results by exploiting WDM, optical amplification in the CO and wavelength routing technologies [106].

Table 2.1 summarizes the discussed PON standards with their topologies, data rates and potential applications. Among the available options, we chose to consider the optical distribution network from GPON for the solutions proposed in this work, due to the following reasons:

- GPON found commercial success and has been widely implemented for the Internet provision, in such way the FTTH infrastructure supporting such standard increased significantly in the last years. Therefore, designing a mobile fronthaul based on the existent ODNs from GPON can be a cost-effective and short-term solution toward 5G radio access networks;
- There is a GPON in the Inatel campus, from the city of Santa Rita do Sapucaí-MG, Brazil. Such infrastructure is available for the Internet provision and research purposes, bringing then the opportunity of conducting our experimental studies under real channel conditions.
- We established a partnership with a local Internet service provider (ISP), called Vivavox (<http://www.vivavox.com.br>), aiming to implement the proposed RoF-based fronthaul solutions in a commercial and wider system. Such ISP uses the GPON standard and has a FTTH infrastructure based on TDM-PON.

In fact, the GPON rigid architecture hinders any easy and dynamic adaptability for simultaneously distributing baseband data stream and RF signals. As alternative to overcome this issue, we are going to exploit the TDM-PON topology from GPON with an additional wavelength assigned to the RoF-based mobile fronthaul application. Such solution fits into systems recognized as WDM overlay, which are described in the next subsection.

Table 2.1 – Summary of the PON standards and some of their aspects.

Standard	Topology	Downstream data rate (Gbit/s)	Upstream data rate (Gbit/s)	Application
ITU-T G.983.x (BPON) [95]	- TDM-PON	- 0.15552 - 0.62208 - 1.24416	- 0.15552 - 0.62208	- Residential services
ITU-T G.984.x (GPON) [96]	- TDM-PON	- 2.4	- 1.2 - 2.4	- Business and residential services
IEEE 802.3ah (EPON) [97]	- TDM-PON	- 1.25	- 1.25	- Business and residential services
IEEE 802.3av (10G-EPON) [98 ]	- TDM-PON	- 10	- 1 - 10	- Business and residential services
ITU-T G.987.x (NG-PON1: XG-PON1) [99]	- TDM-PON	- 10	- 2.5	- Business and residential services
ITU-T G.987.x (NG-PON1: XG-PON2) [99]	- TDM-PON	- 10	- 10	- Business and residential services
ITU-T G.989.x (NGPON 2) [100]	- TWDM	- 40	- 10 - 40	- Mobile backhaul/fronthaul, business and residential services
IEEE P802.3ca 25, 50 and 100G-EPON [104]	- TDM-PON - WDM-PON	- 25 - 50 - 100	- 10 - 25 - 50 - 100	- Mobile backhaul/fronthaul, business and residential services
The expected NGPON 3 [105]	- WDM-PON - OFDM-PON - Coherent-PON	- Not standardized yet	- Not standardized yet	- All the previous ones, with disruptive increases in the network capacity
Super-PON [106]	- WDM-PON	- 10	- 10	- Business and residential services in an extended area

### 2.1.2. WDM overlay

A WDM overlay system consists of using one or more wavelengths on top of the passive optical networks in order to enhance their capacity and enable multiple functionalities. It has been studied since the 90s and allows taking advantage of existing optical equipment and fibers to aggregate new services in a simple and agile way [107]. One of the driven applications has been the distribution of high definition video, overlaid on PON within the wavelength range between 1550 and 1560 nm [87].

Figure 2.5 presents two WDM overlay schemes. Part (a) shows a legacy PON structure, based on TDM-PON and standardized wavelengths (e.g.  $\lambda_1 = 1490$  nm and  $\lambda_2 = 1310$  nm), with video overlay at  $\lambda_3$ . One can note the video distribution occurs by broadcast over the existent PON topology, now updated with WDM couplers. The latter ones are coarse wavelength combiners/decouplers that typically offer reduced power losses in comparison to the power splitters/combiners, as well as higher wavelength range per channel in relation to the WDM or DWDM multiplexers/demultiplexers. At the central office, the WDM coupler combines  $\lambda_3$  from the video OLT with  $\lambda_1$  assigned by the legacy PON OLT for downstream. Such combination could even occur at the remote node according with the provider demand. At ONUs, the WDM coupler realizes the reverse process, ensuring huge bandwidth for the video delivery while maintaining the baseband data downstream and upstream from TDM-PON [87].

Figure 2.5(b) reproduces the same legacy PON structure, however, allowing a set of wavelengths overlaid around 1550 nm. Such WDM overlay scheme integrates the WDM-PON topology in the TDM-PON architecture, creating individual routed wavelength paths toward a point-to-point (P2P) transmission, at the same time of preserving the original PON P2MP characteristic [107]. In comparison to the previous scheme, this solution enhances the network capacity and scalability at a cost of requiring additional WDM couplers at the remote node and a pair of MUX/DEMUX with identical channel spacing. In any case, new functionalities can be added to the FTTx infrastructure without any significant service interruption. Besides the described WDM overlay schemes, there are many others always focusing on leveraging the existing optical access networks to provide new and converged services. As example, four distinct arrangements of TWDM-PON with WDM overlay are reported in [88].

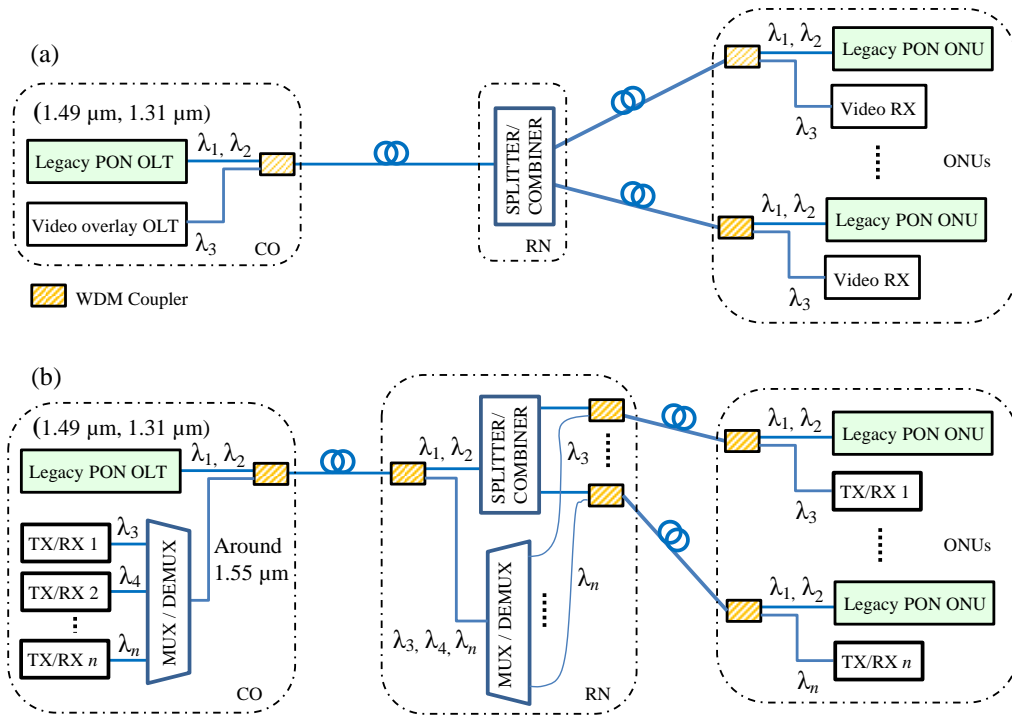


Figure 2.5 – WDM overlay schemes: (a) TDM-PON with video overlay; (b) TDM-PON with a set of wavelengths overlaid. Adapted from [107].

The perspective of multi-service delivery, followed by the idea of evolving from the legacy systems without discontinuity of the previous technology aiming to exploit the investment, bring a coexistence scenario as illustrated in Figure 2.6(a) [89]. It embraces different PON generations, P2P WDM communication and RF overlay in a single optical access network, which shall simultaneously support wired and mobile fronthaul applications. Since the technologies are going to coexist, a careful wavelength planning becomes required.

Figure 2.6(b) shows the recent ITU-T wavelength range considerations for each system, including the respective guard bands [108]. One can observe the wavelength range from 1550 to 1560 nm is assigned to RF video overlay, despite such service is not widely exploited today. Therefore, this band is promising for addressing the emerging RF overlay applications. Other possibility is exploiting the P2P WDM band for such purpose. P2P WDM channels can even be within the 1524-1625 nm wavelength range in the case of the expanded spectrum option, available in the absence of other services.

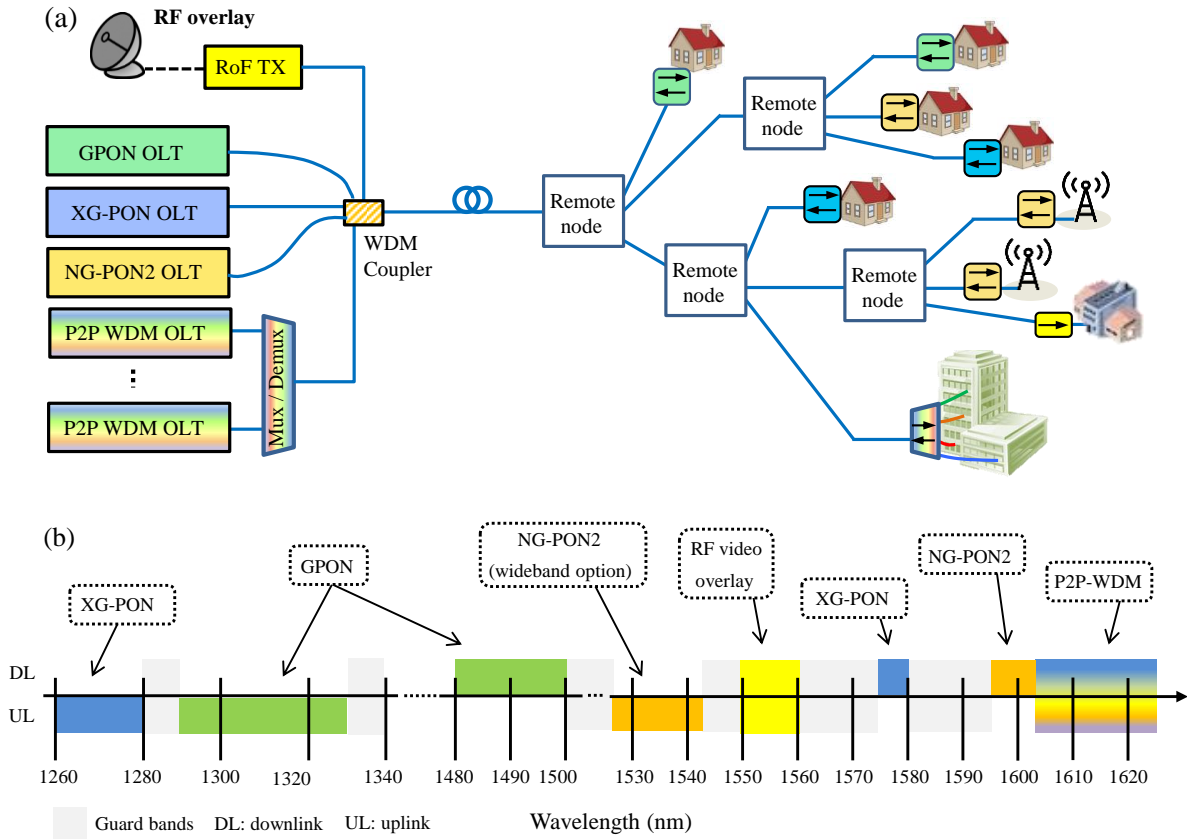


Figure 2.6 – PONs coexistence scenario: (a) Optical access network; (b) Wavelength plan representation.

Adapted from [89].

This work is going to exploit a WDM overlay scheme similar to that from Figure 2.5(a), however, in the context of multi-band 5G systems. The simplicity justifies the choice for such scheme. The radio over fiber solutions for mobile fronthaul applications are going to be implemented within the RF overlay band defined by ITU-T (Figure 2.6(b)), more specifically at 1560 nm, taking advantage of the lasers and WDM couplers available in the laboratory.

## 2.2. Radio Access Network (RAN)

The radio access network (RAN) represents the bridge between the mobile users and the core network, being composed by coax cables and/or optical fibers in addition to the antennas and base station elements. The latter ones are mainly the baseband unit, responsible for the full baseband signal processing, including resource control, and radio unit (RU), which performs RF processing tasks, such as frequency filtering and amplification. According with

the topology, RAN can be classified as distributed radio access network and centralized radio access network [72, 109].

### 2.2.1. Distributed RAN (D-RAN)

The distributed RAN architecture physically locates the baseband unit with the radio unit in the cell sites from the mobile networks. Figure 2.7(a) shows that, initially, the radio and baseband processing functions are integrated into the base station, in such way the functional electronics are placed at the base of the tower and connected with the antennas using coaxial cables. Hence, all functionalities are processed at the cell site, connected to the core network through the gateway and backhaul physical link. This D-RAN structure was implemented mainly to the second generation (2G) [109].

In a second moment, the baseband and radio units are separated from each other as reported in Figure 2.7(b). RU is located close to the antennas and called remote radio head (RRH) or remote radio unit, whereas BBU keeps in the cabinet. RRH and BBU are connected using optical single mode fiber, which enables reducing weight, volume and attenuation in comparison with the coaxial cable. This D-RAN solution also enables to employ short coaxial jumper cables for connecting sector antennas, reducing then RF losses [72].

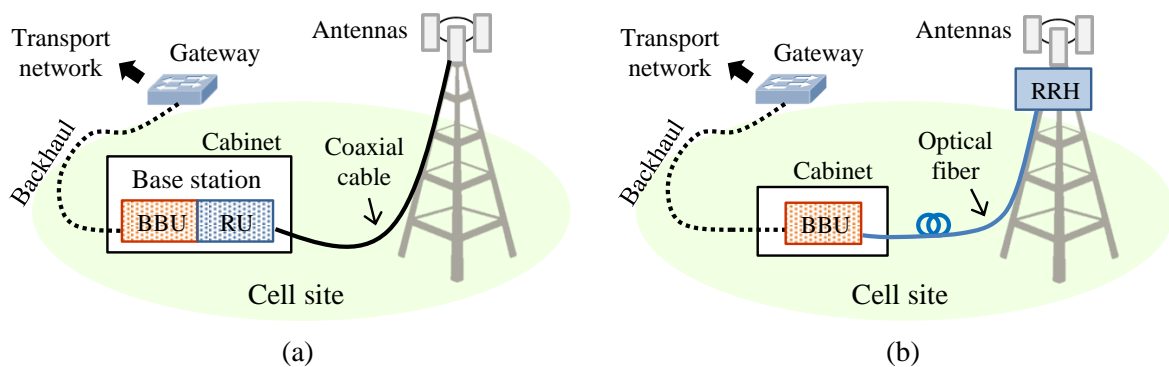


Figure 2.7 – Distributed radio access network: (a) BBU and RU integrated in the base station; (b) BBU in the cabinet and RRH close to the antennas. Adapted from [72].

D-RAN second phase supplied the UMTS and 4G demands, but it is neither scalable nor efficient to deliver the high bandwidth and low latency services expected by 5G. Moreover, D-RAN operational expenditure (OPEX) and capital expenditure (CAPEX) increase significantly when more base stations (called NodeB) are acquired, since each new

site requires a complete energy and refrigeration infrastructure besides a relevant physical area. CAPEX covers the cost needed to the network construction, including site acquisition, RF and baseband hardware, software licenses, installation, etc., whereas OPEX refers to the cost relevant for operating the network, e.g. electricity, site rental, maintenance and upgrade. These expenditures are an important issue for future wireless generations owing the envisaged increment in the number of cell sites. Therefore, D-RAN has not been considered as a competitive RAN solution toward 5G [109-111].

### 2.2.2. Centralized RAN (C-RAN)

The centralized RAN, illustrated in Figure 2.8, rose as an alternative to the distributed architecture. C-RAN keeps RRH close to the remote antenna and centralizes the baseband processing functions from multiple BBUs at the same location, usually the central unit. The latter one is a single equipment room accommodating the so called BBU pool, which may be kilometers (up to 20 km) from RRHs. The backhaul connects the BBU pool with the core network, whereas the fronthaul links connect the BBU pool with diverse RRHs. Fronthaul is mostly based on optical fiber, although it can also be wireless. The RAN solution under discussion proved to be attractive for cost saving and has been widely implemented in 4G commercial networks [30, 112].

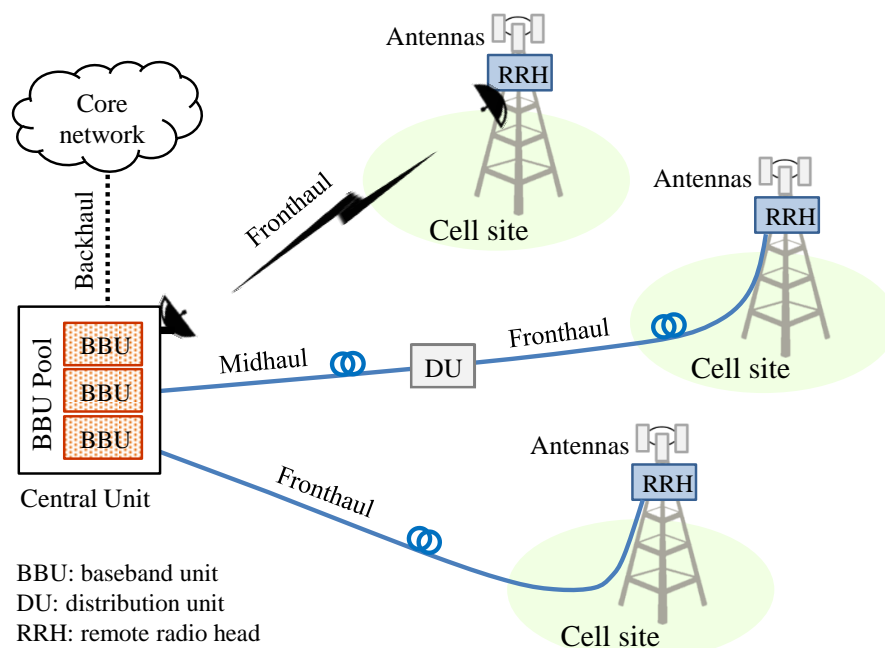


Figure 2.8 – Centralized radio access network.

Figure 2.8 also illustrates the C-RAN architecture according with the next generation fronthaul interface concept, proposed by China Mobile in 2014 toward 5G. Such architecture introduces the distribution unit as new base station element in order to enable a functional split between the baseband functions. Functional split consists of removing some functions from BBU and assigning them to DU or antenna site, which commonly realize fast processing tasks. The complex control functions continue centralized at CU. Fronthaul is to connect DU and RRH, whereas midhaul rises as the connectivity segment between CU and DU. This RAN solution leads to a base station structure named as gNodeB [30].

The C-RAN key advantages that make it promising for 5G can be listed as follows:

- Cost saving on CAPEX and OPEX. The centralization of BBUs and site support equipment in a single room enables to share facilities, such as power, air-conditioning and civil installation. Moreover, the centralization allows simplifying the cell site, which has size and power consumption reduced since it accommodates only RRH and no baseband equipment cabinet. RRH can even sit on poles with minimum site rental fee and support requirement. The network management and maintenance becomes then easier and feasible assuming a large number of base stations [109-113]. In one of the C-RAN field trials reported in literature, it was observed that CAPEX and OPEX for new cell sites can be reduced by 30% and 53%, respectively, compared with the distributed RAN deployment method [112].
- Network deployment speed-up, achieved with the remote site simplification and hardware grouping at CU. In numbers, the RAN construction cycle can be reduced from about 77 days to approximately 30 days when using the centralized architecture [112].
- Scalability and flexibility. Besides the remote site simplification, the central unit is supposed to use general hardware, which can be easily extended and/or upgraded for connecting a number of DUs or RRHs on demand. In addition, CU and DU can be deployed independently as a function of the hardware capacities, leading to flexibility. This characteristic is also achieved by the split options between the C-RAN entities, in such way their tasks can be properly set according to the service requirements [30].

- Performance improvement. The agile communication between co-located BBUs contributes to the latency reduction and can facilitate cooperation mechanisms as coordinate multi-point (CoMP), already introduced in LTE-Advanced (LTE-A). CoMP algorithms in C-RAN benefit from the BBUs quick interaction and can favor, for example, a data rate increase at the cell edge [109, 111].
- Virtualization/cloudification. Since the computation resources are aggregated in the BBU pool, they can be consolidated using industry-standard servers located in data centers. This feature is expected to enable a flexible and on demand resource allocation [30].
- Energy efficiency toward a green network. C-RAN offers energy saving owing factors as centralization, which enables facilities sharing, and virtualization, which reduces the hardware requirement. Furthermore, processing resources can be selectively turned off when a virtual base station is idle, e.g. at night, reducing the power consumption. According with the literature, energy saving on C-RAN reach about 40% over D-RAN due to the shared cooling infrastructure [30], and can exceed 70% depending on the baseband functions centralization level and deployment scale (number of cells that one BBU pool covers) [109, 113].

Indeed, C-RAN brings various advantages that stimulate its commercial deployment for 5G, but a number of challenges need to be addressed. For instance, high bandwidth transport network need to be available, BBUs cooperation approaches are demanded and techniques for the BBU pool virtualization need to be consolidated. The solutions that are going to be proposed in this work are related to the fronthaul link of the C-RAN architecture.

## 2.3. Mobile fronthaul

As mentioned before, fronthaul is a connectivity segment introduced with the C-RAN concept for interfacing central unit or distribution unit with remote radio heads. It requires a broadband physical link to support the 5G features presented on Chapter 1, such as Gbit/s throughput and mm-waves distribution. These characteristics make optical fibers an adequate solution for deploying the transport network. Basically, optical fronthaul links are based on radio over fiber technology, which can take digital or analog RoF schemes.

### 2.3.1. Digital RoF (D-RoF)

Digital RoF schemes digitize analog signals for launching them into the optical fronthaul. More specifically, D-RoF uses CPRI as main interface for producing a sampled digital data stream, although Open Base Station Architecture Initiative (OBSAI) and Open Radio equipment Interface (ORI) are also available. As shown in Figure 2.9, the CPRI frame feeds the E/O conversion stage and next is transmitted through the SMF-based optical link from the central office to the cell site, in which optical-to-electrical (O/E) conversion is realized and radio functions are mandatory for enabling wireless transmission. The remote radio unit functionalities embrace then O/E conversion, CPRI interfacing, digital-to-analog conversion (DAC), RF upconversion carried out by the RF front-end, RF amplification and finally, radiation through the antenna. The described sequence refers to the downlink, whereas the uplink imposes the reverse process [61]. In terms of optical transmitter and receiver, they are typically integrated in a CPRI SFP transceiver in accordance with the block diagram presented in [114].

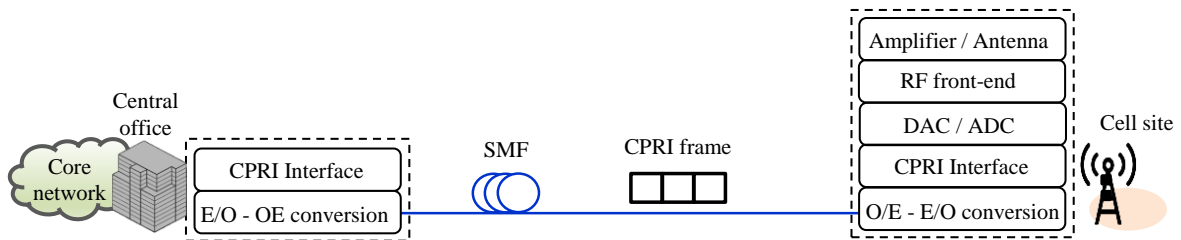


Figure 2.9 – Digital radio over fiber scheme. Adapted from [61].

CPRI-based digital radio over fiber links become the base for commercial 4G fronthaul solutions, supporting legacy radio standards, as well as the functional split between baseband unit and remote radio head. Such transport scheme brings also as advantage the possibility of being integrated to passive optical networks using diffused SFP modules, besides avoiding impairments as dispersion-induced power fading from microwaves and mm-waves over fiber [30].

On the other hand, some drawbacks arise when considering the current digital RoF fronthaul technology for 5G. The first one is the need for digitization equipment and RF conversion stages at the remote site, opposing the C-RAN principle of RRH simplification toward densely distributed 5G cells. This issue is even more critical when introducing the mm-waves access, which requires complex and expensive RF upconversion and

downconversion hardware remotely. Moreover, the constant transmission rate of CPRI leads to an inefficient operation mode, since the throughput keeps the same no matter how much traffic the network is demanding. It can result in unnecessary processing power consumption during the idleness periods [45, 30].

Another challenge to be overcome is the total data rate that CPRI-based D-RoF links require, significantly higher than peak rates achieved on the radio interface. Currently, there are 11 CPRI data rate options, as reported in Table 2.2 [72]. These data rates provide capacity for the in-phase and quadrature (IQ) data, overhead information and line coding. Since a real implementation of remote sites can contain multiple sectors, to cover a 360° angle geographically, and multiple antennas, each one of them with dedicated IQ data flow, the CPRI aggregated bit rate in a digital fronthaul link can be calculated by [115]

$$B_{\text{CPRI}} = S \cdot A \cdot f_s \cdot b_s \cdot 2 \cdot OH \cdot LC, \quad (2.1)$$

in which  $S$  and  $A$  are the number of sectors and antennas per sector, respectively,  $f_s$  is the sample rate (15.36 MS/s per 10 MHz radio bandwidth),  $b_s$  is the number of bits per sample (15 for LTE) and 2 is a multiplication factor related to the separate processing of I and Q samples. Additionally,  $OH$  represents the overhead factor (16/15) and  $LC$  refers to the line coding factor (10/8 or 66/64 depending on the CPRI data rate option).

Table 2.2 – CPRI options with the corresponding line coding factors and data rates.

CPRI options	1	2	3	4	5	6	7	7A	8	9	10
Line coding factor	10/8	10/8	10/8	10/8	10/8	10/8	10/8	66/64	66/64	66/64	66/64
CPRI data rate (Gbit/s)	0.6144	1.2288	2.4576	3.0720	4.9152	6.1440	9.8304	8.1100	10.1376	12.1651	24.33024

Table 2.3 presents examples of CPRI aggregated bit rates as a function of some LTE, LTE-A and 5G potential scenarios. One can note that a LTE base scenario with 10 MHz bandwidth demands 614.4 Mbit/s CPRI total data rate, which exceeds the achievable throughput in the air ( $\approx 50$  Mbit/s for downlink) by more than 12 times. One can also observe that the nature of CPRI enables covering diverse mobile scenarios using the available data rate options (up to 24.3302 Gbit/s). However, the CPRI transmission capacity saturates for massive MIMO and/or wide-bandwidth LTE-A and 5G configurations toward Gbit/s throughput on the radio interface, in such way additional transceivers are required. The aggregated bit rate easily extends into hundreds of Gbit/s in these conditions for both 10/8 and

66/64 line coding factors, demanding a huge fixed bandwidth in the fronthaul. It is worth mentioning that the 5G-related figures are based on the current CPRI framing for LTE, but they will probably not be far from the real performance.

Table 2.3 – CPRI aggregated bit rates as a function of LTE, LTE-A and 5G scenarios.

Scenario	Number of sectors	Number of antennas	Channel Bandwidth (MHz)	LC	CPRI aggregated bit rate (Gbit/s)	Number of CPRI transceivers
LTE	1	1 (SISO)	10	10/8	0.6144	1 (CPRI option 1)
LTE	1	2 (2x2 MIMO)	20	10/8	2.4576	1 (CPRI option 3)
LTE	3	2 (2x2 MIMO)	20	10/8	7.3728	1 (CPRI option 7)
LTE-A	1	2 (2x2 MIMO)	100 (5x20 MHz)	66/64	10.1376	1 (CPRI option 8)
LTE-A	1	8 (8x8 MIMO)	60 (3x20 MHz)	66/64	24.3302	1 (CPRI option 10)
LTE-A	3	8 (8x8 MIMO)	100 (5x20 MHz)	10/8	147.4560	15 (CPRI option 7)
				66/64	121.6512	5 (CPRI option 10)
5G	3	1 (SISO)	200	10/8	36.8640	6 (CPRI option 6)
				66/64	30.4128	3 (CPRI option 8)
5G	3	8 (8x8 MIMO)	200	10/8	294.9120	30 (CPRI option 7)
				66/64	243.3024	10 (CPRI option 10)
5G	3	8 (8x8 MIMO)	400	10/8	589.8240	60 (CPRI option 7)
				66/64	486.6048	20 (CPRI option 10)

Diverse technical solutions to enable a bandwidth-efficient digital fronthaul have been proposed in the literature, such as IQ data compression and new functional splits between BBU and RRH [111]. IQ data compression approaches can employ load-adaptive quantization and less than 15 bits per sample in the digitization process, typically allowing to reduce the required channel capacity by a factor of 2–3 with some performance degradation, e.g.  $\approx 3\%$   $EVM_{RMS}$  [72, 75]. A low-pass filter can also be used to remove redundant spectral data and, consequently, contribute to the signal compression in the frequency domain [72, 111]. On the other hand, the functional split strategy offers different options to transfer part of the baseband functions from BBU to RRH, relaxing the data exchange between them [30, 72]. The enhanced CPRI interface employs such resources to achieve approximately 10-fold reduction of the required bandwidth, at a cost of re-introducing complexity to the remote radio unit and challenges on the CoMP deployment [116, 117]. Therefore, the above-mentioned techniques impose a trade-off between compression ratio, computational resources/delay, signal distortion and complexity. It is important highlighting that CPRI-based D-RoF schemes continue to be further developed to keep as a competitive solution for 5G fronthaul applications. While 100 Gbit/s Ethernet and CPRI (4 x 24.33 Gbit/s) transceivers become commercially available [118], the newest eCPRI 2.0 encourages the Ethernet and IP protocols utilization, as well as the CPRI and eCPRI interworking toward a more bandwidth-efficient transport network [116, 117].

### 2.3.2. Analog RoF (A-RoF)

Analog RoF schemes concentrate the most complex radio functions in the central office and distribute analog signals already in the wireless carrier frequency through the optical fronthaul, as reported in Figure 2.10. First, the baseband DSP stage digitally modulates the input data and DAC delivers the generated analog signal to the RF front-end, which performs RF upconversion to the channel frequency. These tasks can be grouped in a radio equipment or even neglected if the input data comes from a RF signal already in the desired channel frequency. After E/O conversion also in the CO, the analog RF signal is launched into the SMF-based optical link up to the remote antenna unit or radio access unit (RAU), converted to the electrical domain, amplified and finally radiated. The described sequence refers to the downlink, whereas the uplink imposes the reverse process [61].

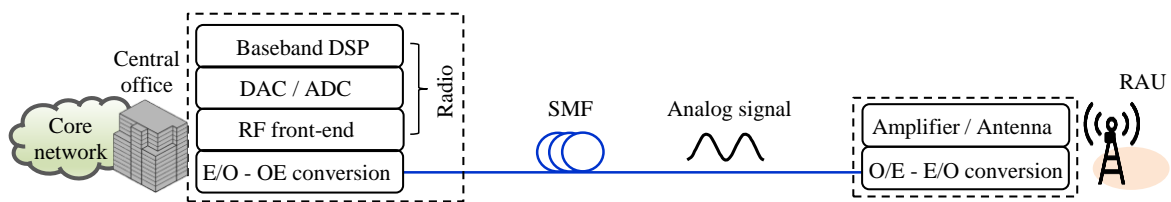


Figure 2.10 – Analog radio over fiber scheme. Adapted from [61].

Figure 2.11 exhibits E/O and O/E conversion schemes that might compose the optical transmitter and receiver of an A-RoF system, respectively. The E/O process can be realized with direct or external modulation. The first approach (Figure 2.11(a)) consists of using a laser, in such way the RF signal at a frequency  $f_{RF}$  promotes a time-variant LD driven current and, consequently, the lightwave intensity variation. Direct modulation up to about 20 GHz is possible and brings the advantage of simplicity [54, 119], but suffers from chirp [44]. This can be overcome by using external modulation (Figure 2.11(b)), in which an optical carrier at  $\lambda_{LD}$  (laser wavelength) and the RF-driven signal are injected in an optical modulator via its optical and RF ports, respectively. The resultant electrical field in the optical domain is then composed of the optical carrier and sidebands equally spaced by  $f_{RF}$ . The referred approach can perform intensity and phase modulation. Besides mitigating chirp, another remarkable advantage over direct modulation is the fact of external modulators are commercially available up to about 40 GHz [120], which means they can offer much larger modulation bandwidths. Obviously, cost increases because of jointly using laser and external modulator to perform the E/O conversion, rather than only a laser from the direct modulation scheme.

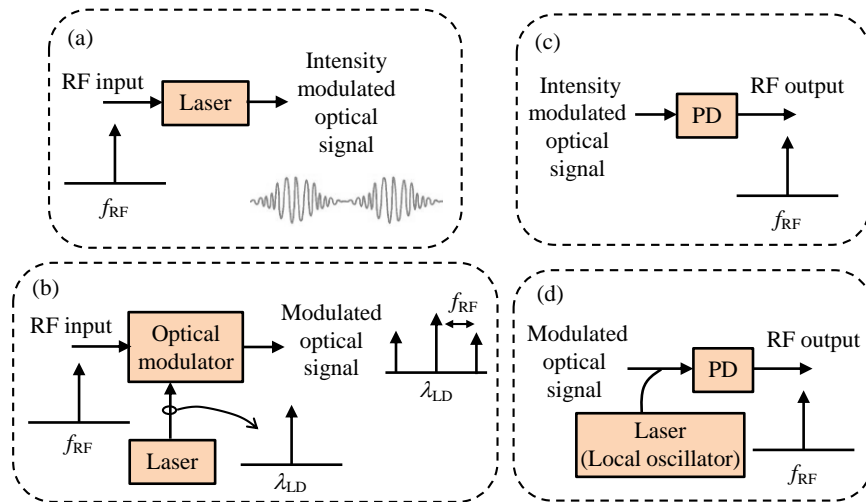


Figure 2.11 – E/O and O/E conversion schemes: (a) Direct modulation; (b) External modulation; (c) Direct detection; (d) Coherent detection. Adapted from [44].

Regarding the O/E conversion process, it can be realized with direct or coherent detection. Direct detection (Figure 2.11(c)) uses only a photodetector for receiving the intensity modulated optical signal and recovering the RF wave, whereas coherent detection (Figure 2.11(d)) basically requires a narrow linewidth local oscillator (LO) laser in addition to PD. The latter approach offers improved sensitivity and also enables detection of phase modulated optical signals [44], however the direct detection implementation is simplest because it requires a single component, commercially available up to 100 GHz [121].

Although D-RoF is the main available fronthaul solution today, A-RoF topologies have been gradually becoming attractive as the envisaged throughput in the air increases and industry begins to deploy mm-waves access for 5G [45]. The A-RoF main advantages over D-RoF are as follows: capability of transporting RF signals through the optical fiber with as little processing as possible, i.e. there are no need for digitization and RF conversion remotely; optical bandwidth and computational power saving due to the digitization absence; remote site simplification, since their elements are reduced to a minimum [44].

The non-direct compatibility with TDM-PON is a drawback of A-RoF schemes, which might also suffer from nonlinear effects and chromatic dispersion. However, there are well-known and non-complex solutions to overcome these issues [60]. For instance, A-RoF topologies can be integrated to the TDM-PON infrastructure using WDM overlay, as described on Section 2.1.2. The nonlinear effects from the light propagation in the optical fiber are typically avoided by not exceeding the optical power threshold ( $P_{th}$ ) defined as

$$P_{\text{th}} = \frac{1}{\gamma L_{\text{NL}}}, \quad (2.2)$$

in which  $\gamma$  is the fiber nonlinear coefficient and  $L_{\text{NL}}$  represents the fiber length over which nonlinear effects become relevant [122]. Nonlinearities from the electro-optic components that cause inter-modulation distortion can be minimized by optical or electrical techniques, such as mixed polarization, dual-wavelength linearization and pre-distortion [123].

Regarding the chromatic dispersion, it causes power fading, i.e. power nulls at different fiber lengths calculated by [44]

$$L_{\text{DH}} = \frac{(2H + 1) \cdot \pi}{\beta_2 \omega_{\text{RF}}^2}, \quad (2.3)$$

where  $H$  is an integer,  $\omega_{\text{RF}}$  is the RF angular frequency and  $\beta_2$  is the second order dispersion given by

$$\beta_2 = -\frac{D \cdot \lambda^2}{2 \cdot \pi \cdot c}, \quad (2.4)$$

in which  $D$ ,  $\lambda$  and  $c$  are the chromatic dispersion, optical wavelength and speed of light respectively. Table 2.4 shows the dispersion-induced power fading is more severe as the signal frequency increases and could impact 5G fiber-wireless systems in the frequency range 2 (24.25 – 52.60 GHz), since fading points occur within the planned SMF-based fronthaul distances. Nevertheless, using spans of dispersion compensating fiber (DCF) or optical single-sideband modulation techniques enable efficiently mitigating this impairment. Other possibilities are planning the network terminations to not coincide with the fading points or using intermediate frequency over fiber, which requires a mixer at the remote site or an up-conversion photonic technique to reach the wireless frequency [40].

From the previous discussions on D-RoF and A-RoF technologies, one can conclude that advantages of each solution might be exploited to meet the 5G fronthaul demands and probably there will be no an “one-size-fits-all” approach. A prove of this is the fact that mobile fronthaul based on hybrid analog/digital RoF schemes has already been proposed in the literature [124], whereas groups of researchers and companies continue to design and update both transmission methods individually [45, 75]. In this thesis, only A-RoF schemes

will be considered because we understand it fits better with the C-RAN principle, i.e., promotes the centralization and RRH simplification, besides bandwidth and processing savings. Anyway, the A-RoF solutions that are going to be presented may coexist with D-RoF approaches in a future hybrid fronthaul, especially whether D-RoF sustains commercial success. With respect to the E/O and O/E conversion techniques, external modulation and direct detection are going to be adopted for avoiding chirp and simplifying the optical receiver, respectively. The possibility of using optical modulators with independent RF inputs also justifies the choice for external modulation, since one of our goals is simultaneously distributing RF signals at distinct spectral bands.

Table 2.4 – Fading points as a function of the radiofrequency.

Frequency (GHz)	$L_{D0}$ (km)	$L_{D1}$ (km)	$L_{D2}$ (km)
52.60	1.31	3.93	6.55
26.00	5.36	16.09	26.81
24.25	6.16	18.49	30.82
6.00	100.71	302.14	503.57
3.50	295.98	887.93	1,479.88
0.70	7,399.41	22,198.23	36,997.05

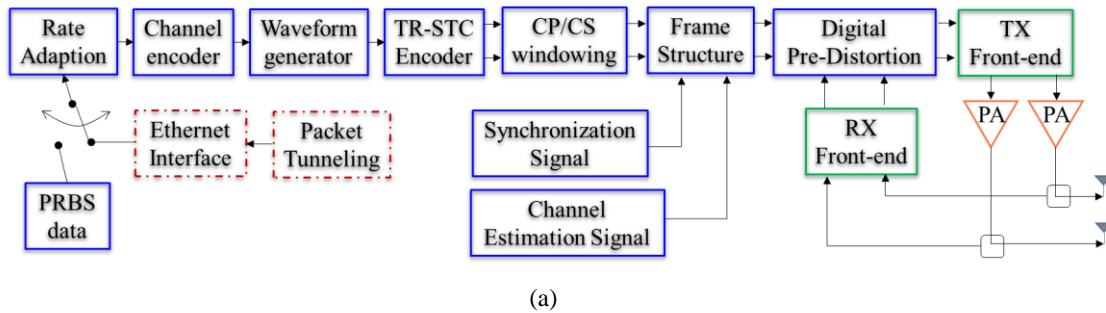
\*Calculation for  $D = 17 \text{ ps.nm}^{-1}\text{km}^{-1}$  (in accordance with standard SMF) and  $\lambda=1560 \text{ nm}$  (wavelength within the RF overlay window from Figure 2.6(b)).

## 2.4. The Intel's 5G Transceiver

### 2.4.1. Block diagram, operation principle and features

The 5G transceiver has been developed by our research group in the last years for the Radiocommunications Reference Center (CRR) and 5G-Range projects [125, 29]. The purpose is addressing the most-demanding 5G scenarios and applications, mainly remote and rural access. The prototype was implemented in a software defined radio platform with LabView Communications by means of using a NI-PXIe 1071 personal computer (PC) and two NI-USRP 2954R universal software radio peripherals (USRPs) as hardware. GFDM and F-OFDM waveforms are the core of this innovative radio equipment, which operates in the 700 MHz band for favoring long-range coverage. Figure 2.12 depicts its transmitter and receiver block diagrams.

## Transmitter



## Receiver

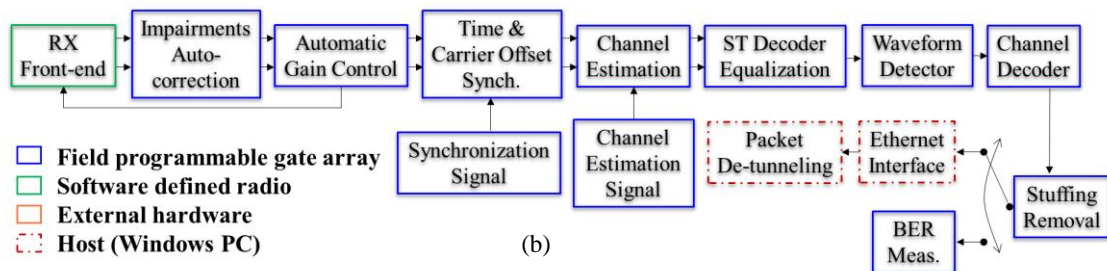


Figure 2.12 – Block diagram of the 5G transceiver: (a) Transmitter; (b) Receiver.

The developed 5G transceiver can operate in the continuous data transfer mode (CDTM), in which the RF signal at the transmitting antennas is always present, or in burst data transfer mode (BDTM), where the RF signal is available only when there are useful data from the users to be transmitted. The rate adaptation block in the transmitter side generates dummy information for the CDTM operation, appending stuffing bits into the input data signal, when the income throughput is smaller than the transceiver capacity. It is worth mentioning the useful data consists of a pseudorandom binary sequence (PRBS) or packets from the Ethernet interface.

The input data signal with appropriate data rate is delivered to the channel encoder, which adds parity information to improve the robustness against the noise and interference introduced by the channel. Two forward error control (FEC) codes were implemented: i) low-density parity check (LDPC) code [126]; ii) polar code [127]. Code rates of 1/2, 2/3, 3/4 and 5/6 can be selected for any one of these options.

The encoded data sequence is modulated into a 4 up to 256 quadrature amplitude modulation (QAM) symbol and then mapped into an OFDM, GFDM or F-OFDM signal by the waveform generator. Such block is the main responsible for the 5G transceiver flexibility, defined as the capability of providing the three distinct waveforms. Once the GFDM signal is

generated, other waveforms can be easily set as alternative cases. For instance, GFDM is a non-orthogonal waveform that transmits  $N = MK$  QAM symbols per block using  $M$  subsymbols per subcarrier and  $K$  subcarriers. It means GFDM can accommodate more than one subsymbols per subcarrier. By making  $M = 1$ , keeping  $K > 1$ , and using a rectangular filter as pulse-shape (typically employed for the OFDM waveform generation), OFDM is covered since  $N$  become equal to  $K$  QAM symbols, i.e. one subsymbol per subcarrier. Additionally, F-OFDM is achieved by setting GFDM to behave as OFDM as previously described, and using a sub-band digital filter bank to restrict the OOB [11].

The modulated signal is applied to a time-reversal space-time coding (TR-STC) scheme [128], which generates two correlated versions of the transmit signal that are propagated to the receiver by two separated antennas. This procedure allows the receiver to harvest diversity gain from multipath channel, in such way the system performance can be improved. A CP and a cyclic suffix (CS) are added to the transmit signals in order to improve robustness against multipath channels. A time window can be optionally applied to the waveform for further reducing OOB.

The frame structure block multiplexes the user data with the synchronization and channel estimation preambles, which are used on the receiver stage to recover synchronism and perform the channel equalization. The transceiver parameters, such as waveform, modulation order, coding rate, number of subcarriers and subsymbols, CP and CS length, periodicity of the synchronization, channel estimation preambles and the overall occupied bandwidth, can be adjusted according with the channels conditions and application requirements.

The generated signals, as any other multicarrier system, might present high peak-to-average power ratio [129]. Since power amplifiers (PA) are used to transmit the OFDM, GFDM or F-OFDM signal, the high amplitude peaks can lead the PA to its non-linear region, resulting in high spectrum regrowth, high OOB and intercarrier interference. A digital pre-distortion scheme has been implemented to reduce the effect of the non-linear distortions introduced by PA. Basically, DPD is a non-linear block with input-output amplitude and phase responses that are complementary to those presented by PA [130]. Figure 2.13 illustrates the DPD and PA amplitude transfer functions for demonstrating the DPD principle. In order to DPD identify the PA transfer function, samples of the transmitted signals are feedback to the DPD block in a closed loop as showed in the transceiver block diagram. This approach allows DPD to constantly adjust its coefficients, whenever there is any change in the PA operation due to temperature variation, gain adjustment, operation frequency and occupied

bandwidth. DPD might also act in a static way, in which the operator adjusts its coefficients for reaching linearization.

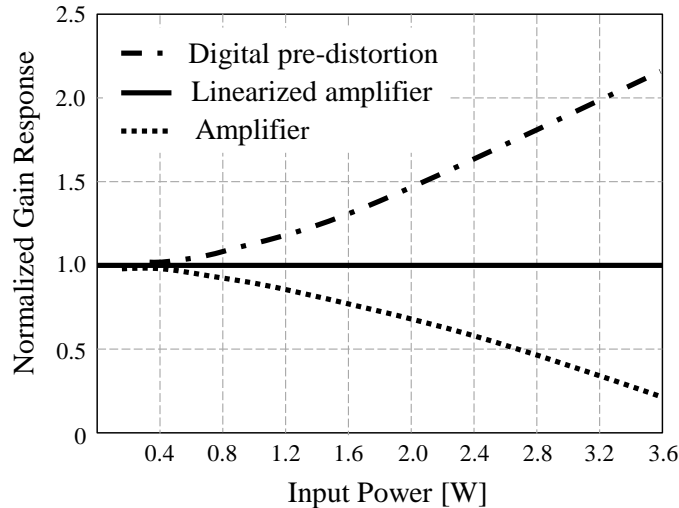


Figure 2.13 – Principle of the DPD operation.

The 5G transmitter next stage is the RF front-end, which determines the channel frequency and the power level that feeds power amplifiers. The latter ones are implemented in external hardware because the USRP is limited to a 20 dBm maximum output power. Subsequently, PAs feed the antennas for enabling radiation.

At the receiver stage, the RF front-end performs downconversion, whereas the impairment auto-correction block removes the imperfections introduced by the RF chain, such as IQ imbalance. The automatic gain control block adjusts the input level, assuring that the analogic-to-digital converter dynamic range is properly exploited. Time and frequency synchronization is performed using the transmitted synchronization preamble and a locally generated version of this signal. After synchronization, the channel estimation block estimates the channels frequency responses based on the received channel estimation preambles.

The estimated channel frequency responses are used by the space-time (ST) decoder to combine the signal received by the multiple antennas, resulting in diversity gain. In case of employing two receive antennas, the ST decoder can achieve diversity of order 4 (MIMO 2x2). The ST decoder also equalizes the combined signal and delivers it to the waveform detector, which performs the QAM demapping, feeding the channel decoder with the received bits. The channel decoder removes errors introduced by the channel and the stuffing removal block eliminates the dummy information introduced by the rate adaptation block, finally, delivering only the relevant information to the Ethernet interface.

The 5G transceiver main features are as follows:

- Real time GFDM, F-OFDM and OFDM waveforms generation, which enables properly selecting one of them and, consequently, covering different scenarios with attractive performance;
- Low out-of-band emission in case of using GFDM and F-OFDM, which favors the coexistence with other technologies, e.g. TV broadcast and 3GPP legacy systems;
- Flexible modulation, in such way the most robust 4-QAM can be used to provide connectivity for IoT devices, while 256-QAM provides the high data rate for mobile broadband access;
- Flexibility on setting LDPC or Polar code in the data plane as a function of the application scenario. The rationale here is that LDPC outperforms Polar codes when the code word is large (thousands of bits from the eMBB scenario), while Polar codes outperform LDPC when the code word is small (tens to few hundreds of bits). On the long range usage case, the LDPC advantage to Polar codes is marginal and under the influence of imperfect channel estimation, Polar Codes outperforms LDPC [131];
- MIMO 2x2 for diversity, which favors robustness for the long range coverage;
- Digital pre-distortion, which enables to reduce non-linear distortions introduced by electrical amplifiers;
- Simple graphical interface for setting the transmission parameters and measuring the digital performance, as reported in Figure 2.14.

The described 5G transceiver, when compared to the commercially available 5G test solutions that employ the 5G NR current version [132, 133], differs by increasing the flexibility and enabling a broader research application. For example, the real-time implementation to cover OFDM, GFDM and F-OFDM allows us to compare the performance of these waveforms in different scenarios, while 5G NR uses only CP-OFDM. The FEC options in the data field bring the possibility of properly setting Polar or LDPC codes according to the usage case, while 5G NR uses LDPC. Reduced OOB is achieved with time-windowing and filtering in the digital domain, whereas 5G NR relies on RF filtering for reducing OOB. The prototype supports MIMO for multiplexing and also diversity, instead of only a multiplexing MIMO scheme from the 5G NR.

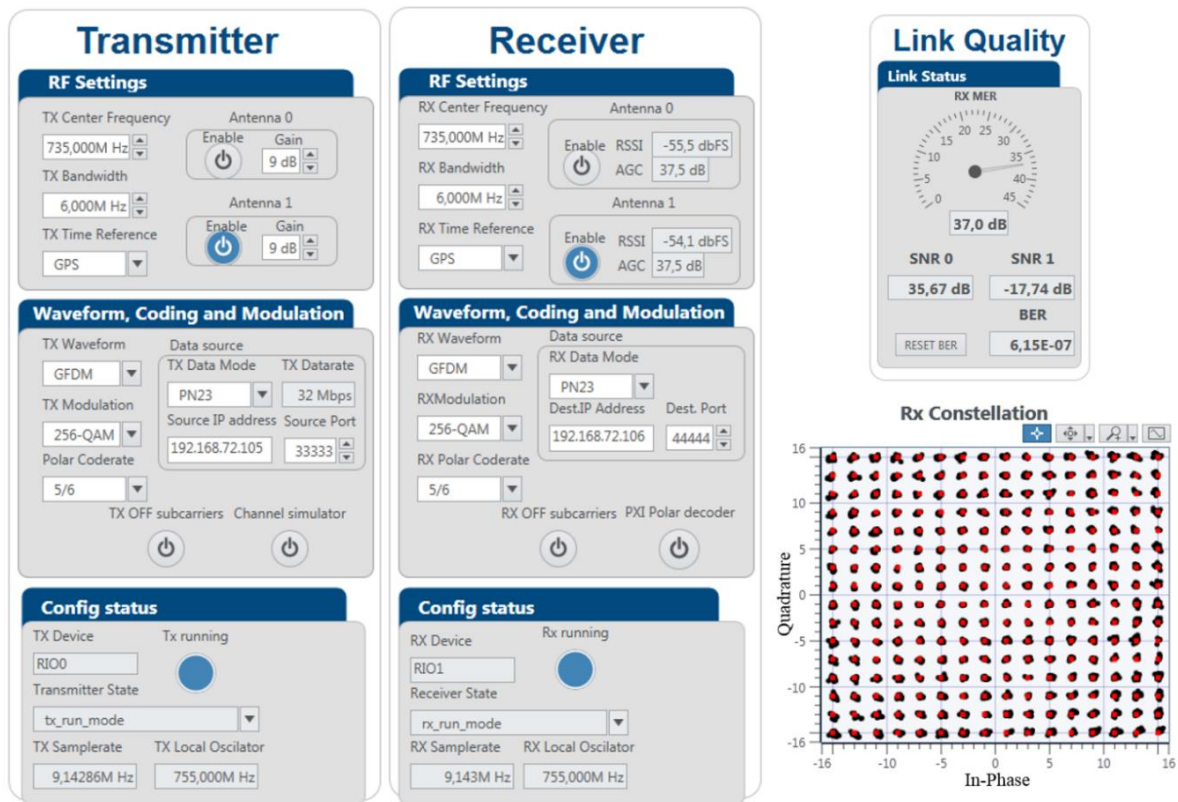


Figure 2.14 – The main graphical interface of the 5G transceiver.

## 2.4.2. Performance from the waveform point-of-view

The 5G transceiver performance evaluation from the waveform point-of-view is based on three main measurements: i) spectral efficiency, given by the data throughput for a given occupied bandwidth; ii) modulation error ratio (MER), which defines the dispersion of the QAM symbols; iii) Out-of-band emission, related to unwanted emissions immediately outside the channel bandwidth resulting from the modulation process and non-linearity in the transmitter.

OFDM and F-OFDM achieve the same spectral efficiency, since both schemes use one CP and one CS per waveform symbol. On the other hand, GFDM can achieve higher spectral efficiency, since it uses one CP and one CS per  $M$  waveform symbols. In the current implementation, the data rate has been adjusted by employing a different number of subcarriers in each scheme. While GFDM has  $K = 512$  subcarriers and  $M = 3$  waveforms symbols for each CP and CS, OFDM and F-OFDM employ  $K = 1536$  and  $M = 1$  to achieve the same throughput. By comparing the MER parameter obtained by each waveform, GFDM

and OFDM achieve about the same value (up to 40 dB). The sub-band filtering applied to the F-OFDM waveform degrades the MER performance in approximately 2 dB.

Figures 2.15(a) and 2.15(b) present the measured electrical spectra at the 5G transceiver RF output for each waveform, in case of using 10 MHz bandwidth and 735 MHz central frequency. Particularly in Figure 2.15(b), the subcarriers on the lower half of the spectrum are inactive, with the exception of the extreme subcarriers close to 730 MHz. All subcarriers in the upper spectrum part are active. This configuration denotes a fragmented spectral allocation, emulating a case where a primary user is detected in this portion of the spectrum. F-OFDM slightly outperforms GFDM in term of OOB. The difference of performance could be more visible at higher power levels and occurs because the F-OFDM wider sub-band filtering allows for steeper filter frequency response when compared with the GFDM subcarrier filtering. Both GFDM and F-OFDM outperforms OFDM in terms of OOB by approximately 20 dB. Clearly, OFDM cannot be used to avoid interference outside the desired band without RF filtering. Among the considered waveforms, only GFDM and F-OFDM can be used for fragmented and dynamic spectrum allocation without RF filters.

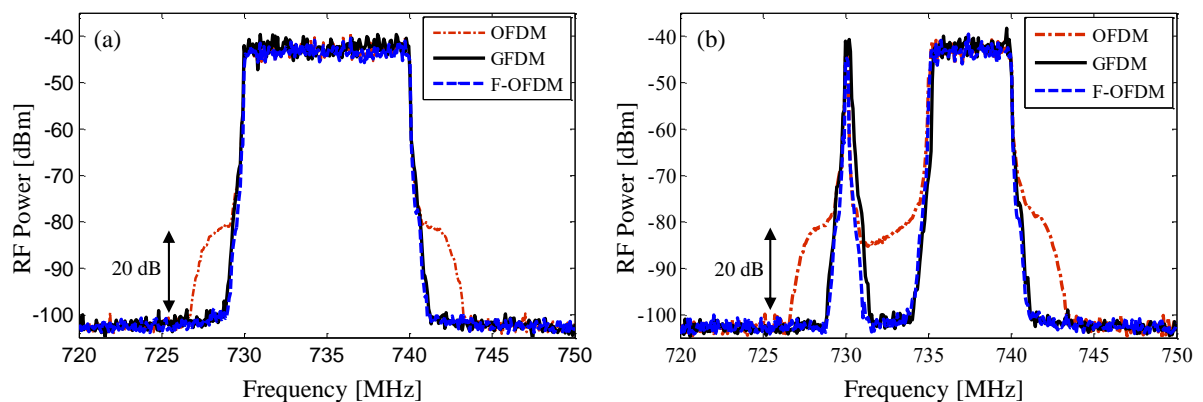


Figure 2.15 – Electrical spectra at the 5G transceiver RF output for OFDM, GFDM and F-OFDM waveforms:  
(a) All subcarriers on; (b) Some subcarriers off.

It is worth mentioning that GFDM-based field trials have been realized by the CRR research group in order to demonstrate the 5G transceiver applicability in different wireless scenarios. The prototype was successfully used for providing a video conference between two buildings of the Esplanade of Ministries, in Brasília-DF, Brazil, as well as for delivering Internet to a high school in a rural area, from the city of Santa Rita do Sapucaí-MG, Brazil. A smart vegetables garden was also connected allowing sensors control and remote operation of the watering [134, 135].

### 3. RoF solutions for multi-band 5G systems

Advances on A-RoF links have indicated the possibility of sharing an optical infrastructure to simultaneously provide multiple services at distinct spectral bands, resulting in the so called “Multi-band Systems”. One of the solutions is using multiple optical transceivers, each one dealing with a radiofrequency and operating at an optical wavelength, as proposed in [61]. The corresponding architecture leads to a RoF architecture based on WDM, which might employ an optical switch to enable flexibility on assigning the RF signals to the distributed remote antenna units. RF interferences in the transport network are not an alarming issue for such approach, since each RF signal is intensity modulated onto a specific wavelength. However, the requirement of one optical transceiver per RF signal may be not attractive from the perspective of radio access technologies exploiting multiple frequencies.

Moreover, other strategies are taking benefits of requiring a single light source, e.g. Ho et al. proposed a three-band RoF system based on direct and external modulation [70]. The methodology consists of applying a RF signal to a DFB laser and stimulating a large optical modulation index (9%), which results in a multi-wavelength output characteristic, exploited as light source. The modulated field is then split into three parts and goes through three segments, in which selected wavelengths are filtered out and handled independently. One segment preserves the direct transmission, whereas the other two add external modulation to distribute electrical signals at different spectral bands. The authors successfully demonstrated the jointly transmission of baseband, CATV (channels 2-78) and 6 GHz RF signals, but notable drawbacks from this approach are the need for multiple optical filters and electro-optic modulators.

As an alternative to reduce the complexity on providing wired and wireless downstream services simultaneously, Pan and Yao proposed a RoF scheme that employs laser, SD-MZM and electrical power combiner at CO, as well as direct detection at the remote unit [69]. In such approach, a 1.25 Gbit/s baseband signal and an UWB (3.1–10.6 GHz) signal were electrically combined to drive the SD-MZM and modulate the optical carrier from LD. After transmission over fiber, the electrical signals were recovered by a single photodetector. It was demonstrated that the baseband transmission had no influence on the UWB signal, whereas the latter one caused a maximum power penalty of 0.4 dB for reaching bit error rate (BER) of  $10^{-3}$  with the baseband communication.

Hu et al. presented a similar approach in [85], however replacing the UWB signal to  $120 \times 20$  MHz LTE-like co-channels. These ones were multiplexed and then electrically

combined with a 2.5 Gbit/s baseband signal to drive the SD-MZM, also fed by a DFB laser. Again, direct detection including a single photodetector was applied at the end of the RoF link. It is worth mentioning that a pair of electrical low pass and band pass filters were employed at the transmitting and receiving stages to avoid overlap between the baseband and intermediate frequency (IF) signals. With such configuration, the coexistence analysis pointed out to 0.15% EVM degradation over the measured average EVM (3.89%) related to the 120 channels when the baseband signal was off. According to authors' comments, the hybrid baseband-IF transmission scheme also imposed a power penalty of about 4 dB for the baseband signal, although no results were showed concerning this issue.

Additionally, Morant et al. exploited the external modulation technique to simultaneously distribute baseband and distinct wireless standards, namely: DVB-T in the 800 MHz band; LTE at 2.6 GHz; WiMax at 3.5 GHz; UWB signals at 3.96 and 4.448 GHz [71]. The electrical signals were combined using a 5:1 RF combiner before driven the SD-MZM at quadrature bias point (QP) and being launched into the fiber over the laser wavelength (1554 nm). The multi-band receiver performed the optical-to-electrical conversion using a single photodetector. At the remote unit, the signal-to-noise ratio (SNR) reached approximately 40 dB for the baseband signal, 30 dB for the DVB-T, LTE and WiMax signals, as well as 26 dB for the UWB signals. The authors considered the implementation as a successful, but the impact of the coexistence over each signal was not analyzed.

This Chapter focuses on presenting and investigating two A-RoF techniques to support multi-band 5G mobile systems and Gigabit Ethernet (GbE) wired communication. It is structured in four sections. Section 3.1 describes the Mach-Zehnder modulator (MZM), a key component for the RoF approaches. Section 3.2 reports the first studied RoF technique, which is based on single-drive MZM and employs a diplexer to combine RF-driven signals at 5G predicted spectral bands. Section 3.3 introduces the second one, an innovative RoF solution based on dual-drive MZM. The performance analysis of both methodologies taking into account the signals coexistence is presented in Section 3.4.

### **3.1. The Mach-Zehnder modulator (MZM)**

The Mach-Zehnder modulator is one of the most used optical modulators for performing external modulation in broadband photonic analog links. It is structured with electrodes and two separate optical guides of equal length, called "arms", in such a way the

input optical signal is split into these ones and posterior recombined by a Y junction. An incident wave in the electrical domain changes the optical signal phase in one of the arms relative to the other, affecting the interferometric recombination and generating the intensity modulated optical signal at the MZM output. Figure 3.1(a) reports the MZM transfer function, which can be written as [44]

$$TF = \frac{I_{out}}{I_{in}} = \frac{1}{2} \left[ 1 + \cos \left( \frac{\pi \cdot V_e}{V_\pi} \right) \right], \quad (3.1)$$

where  $I_{out}$  and  $I_{in}$  are the MZM output and input optical intensity, respectively,  $V_\pi$  is the modulator half-wave voltage and  $V_e$  is the incident electrical signal. The last one can be described by

$$V_e = V_m \cos(\omega_{RF}t) + V_{bias}, \quad (3.2)$$

where  $V_m$  and  $\omega_{RF}$  refer to the amplitude and angular frequency of the RF-driven signal, respectively, and  $V_{bias}$  is the MZM bias voltage. Specifically,  $V_{bias}$  determines the region of the transfer function in which the modulator operates. The quadrature point (QP) is preferred to address optical signal modulation and avoid distortions. In contrast, the enhanced nonlinearity from the maximum and minimum transmission points (MATP and MITP) enable additional applications, e.g. RF downconversion and optical frequency multiplication [31, 37].

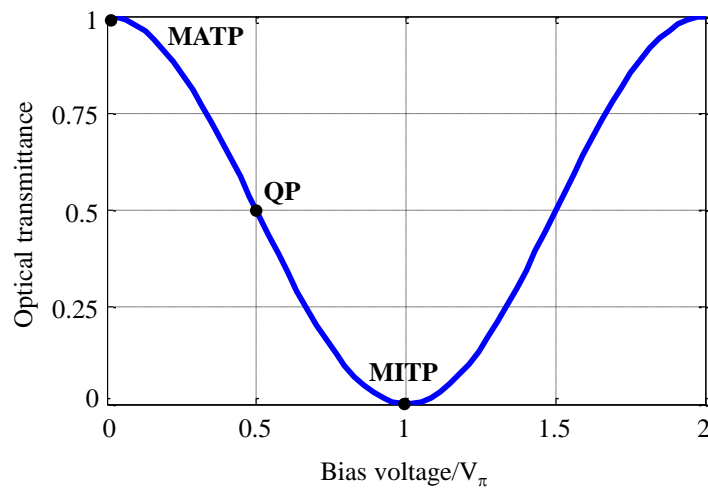


Figure 3.1 – MZM transfer function.

The impact of the modulator bias point on the resulting signal can be clearly noticed by analyzing the electrical field at the MZM output, described by [136]

$$E_{\text{out}}(t) = E_o \cos\left(\frac{\pi}{2} \cdot \frac{V_e}{V_\pi}\right) \cos(\omega_o t), \quad (3.3)$$

where  $E_o$  and  $\omega_o$  denote the amplitude and angular frequency of the input optical carrier, respectively. Applying Eq. (3.2) in Eq. (3.3) enables to express the modulated signal at the MZM output as

$$\begin{aligned} E_{\text{out}}(t) &= E_o \cos\left[\frac{\pi}{2} \cdot \frac{V_m \cos(\omega_{\text{RF}} t) + V_{\text{bias}}}{V_\pi}\right] \cos(\omega_o t) = \\ &E_o \cos\left[\frac{\pi V_m}{2V_\pi} \cdot \cos(\omega_{\text{RF}} t) + \frac{\pi V_{\text{bias}}}{2V_\pi}\right] \cos(\omega_o t), \end{aligned} \quad (3.4)$$

which might be expanded using Bessel functions and, therefore, rewritten as [37, 136]

$$\begin{aligned} E_{\text{out}}(t) &= E_o \cos\left(\frac{\pi V_{\text{bias}}}{2V_\pi}\right) \\ &\cdot \left\{ J_0\left(\frac{\pi V_m}{2V_\pi}\right) \cos(\omega_o t) \right. \\ &+ \sum_{n=1}^{\infty} \left[ J_{2n}\left(\frac{\pi V_m}{2V_\pi}\right) \cos(\omega_o t + 2n\omega_{\text{RF}} t - n\pi) \right. \\ &\quad \left. \left. + J_{2n}\left(\frac{\pi V_m}{2V_\pi}\right) \cos(\omega_o t - 2n\omega_{\text{RF}} t + n\pi) \right] \right\} \\ &+ E_o \sin\left(\frac{\pi V_{\text{bias}}}{2V_\pi}\right) \\ &\cdot \left\{ \sum_{n=1}^{\infty} \left[ J_{2n-1}\left(\frac{\pi V_m}{2V_\pi}\right) \cos(\omega_o t + (2n-1)\omega_{\text{RF}} t - n\pi) \right. \right. \\ &\quad \left. \left. + J_{2n-1}\left(\frac{\pi V_m}{2V_\pi}\right) \cos(\omega_o t - (2n-1)\omega_{\text{RF}} t + n\pi) \right] \right\}, \end{aligned} \quad (3.5)$$

being  $J_n$  the Bessel function of the first kind of order  $n$ . From Eq. (3.5), one can observe that optical carrier and sidebands equally spaced by the RF-driven signal frequency ( $f_{\text{RF}} = \omega_{\text{RF}}/2\pi$ ) compose the optical spectrum at the MZM output, illustrated in Fig. 3.2(a) for quadrature biased MZM ( $V_{\text{bias}} = V_\pi/2$ ). This spectrum form allows preserving  $f_{\text{RF}}$  after the photodetection process. On the other hand, biasing MZM to MATP results in  $\frac{\pi V_{\text{bias}}}{2V_\pi} = 0$ , odd sidebands suppression and optical spectrum with  $2f_{\text{RF}}$ -spaced dominant components (Fig. 3.2(b)). The  $E_{\text{out}}(t)$  detection generates then a RF carrier whose frequency is twice higher than that of the

RF-driven signal. Additionally, biasing MZM to MITP ( $V_{\text{bias}} = V_{\pi}$ ) makes  $\frac{\pi V_{\text{bias}}}{2V_{\pi}} = \frac{\pi}{2}$  and only odd sidebands become part of  $E_{\text{out}}(t)$ . Figure 3.2(c) illustrates the corresponding optical spectrum, composed by  $2f_{\text{RF}}$ -spaced dominant sidebands. The  $E_{\text{out}}(t)$  detection with such configuration causes once again the RF carrier frequency multiplication by a factor of 2, besides significant electrical power reduction owing the spectral components suppression [37].

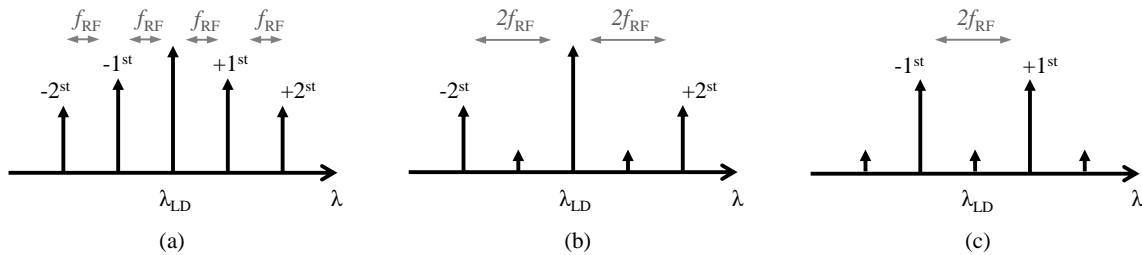


Figure 3.2 – Optical spectrum at the MZM output: (a) MZM biased to QP; (b) MZM biased to MATP; (c) MZM biased to MITP.

Three types of Mach-Zehnder modulators are commonly available, as illustrated in Figure 3.3. They differ mainly by the electrical inputs number and arrangement, since the operational principle is the same. SD-MZM offers one RF input port and a single bias control, whereas DD-MZM enables two RF ports with independent bias control ( $V_{\text{bias1}}$  and  $V_{\text{bias2}}$ ) in the upper and bottom arms. The IQ or dual-parallel MZM (DP-MZM) combines two SD-MZMs and adds a third bias control ( $V_{\text{bias3}}$ ) possibility before the final Y junction. It is worth highlighting each one of these MZM types can be properly used to cover specific applications. For instance, SD-MZM typical functions include external modulation and photonic processing of a single RF signal [31]. A DD-MZM well-known application refers to the optical single-sideband modulation [137], whereas DP-MZM recognized functions include IQ modulation and photonic mm-waves generation [78, 136].

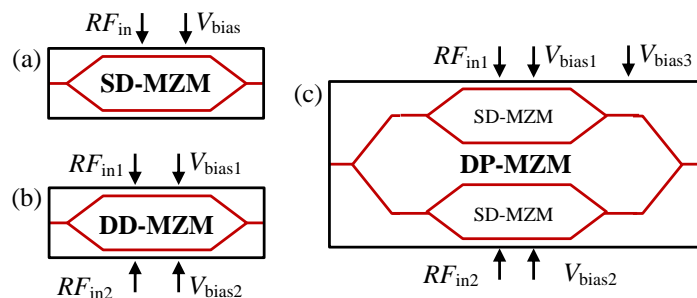


Figure 3.3 – MZM types: (a) Single-drive; (b) Dual-drive; (c) Dual-parallel.

We have experimentally investigated the SD-MZM and DD-MZM applicability to simultaneously modulate an optical carrier with multiple RF signals at distinct spectral bands, thus integrating analog RoF techniques for multi-band 5G systems. Dual-parallel MZM has not been considered for such purpose because it probably leads to a performance similar to that from DD-MZM, with the disadvantage of requiring the third bias control.

### 3.2. RoF technique based on a single-drive MZM

This section reports the analog RoF technique based on SD-MZM for simultaneously distributing distinct RF signals on top of a Gigabit Ethernet wired link. The 6 GHz and 28 GHz frequency bands were chosen for the experimental investigation, with the aim of addressing two 5G predicted bands. Figure 3.4 presents the block diagram of the proposed approach, which is in contrast to methodologies that apply one optical transceiver or modulator per RF wave in order to enable multi-band RoF systems. The current topology also differs from [69], [71] and [85] by supporting GbE communication and 5G potential frequencies with WDM overlay.

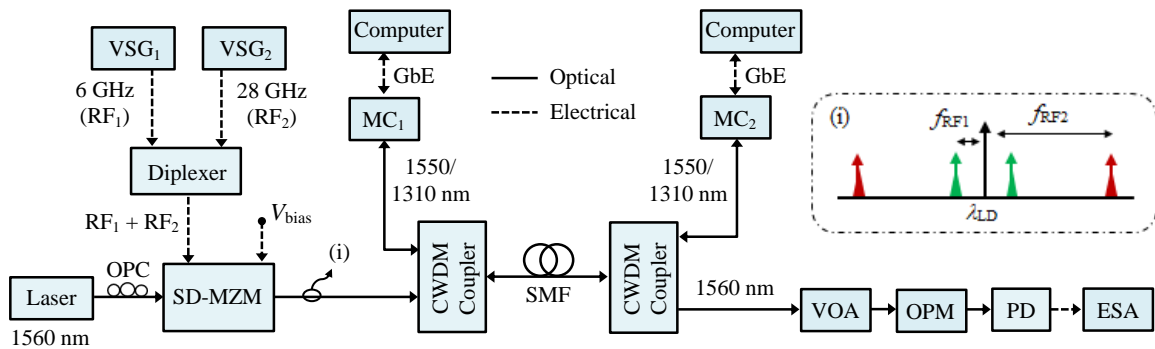


Figure 3.4 – Multi-band A-RoF technique based on a single-drive Mach-Zehnder modulator.

Since SD-MZM has only one RF input port, the diplexer combines two RF-driven signals ( $RF_1$  and  $RF_2$ ) from vector signal generators ( $VSG_1$  and  $VSG_2$ ) and delivers the resultant electrical field to the modulator, which also receives a 1560 nm optical carrier from a laser, and a bias voltage.  $RF_1$  corresponds to a 120 Mbit/s 16-QAM signal at 6 GHz, whereas  $RF_2$  is a 50 Mbit/s QPSK signal at 28 GHz. The lower bitrate in the 28 GHz band is due to the fact the modulation order was reduced for reaching robustness and the bandwidth was not increased due to the hardware limitations at this research phase.

The broadband diplexer imposes insertion loss (IL) lower than that from broadband power dividers/combiners. As an example, the DPX-1721 diplexer from Marki imposes 1.5 dB IL at 28 GHz [138], whereas the PD-OR636 power combiner also from Marki imposes 6 dB IL at the same frequency [139]. Regarding the optical carrier wavelength (1560 nm), it was set to meet the laser channel grid and also to be within the RF/video overlay band defined by ITU-T [108].

Following with the technique description, an optical polarization controller (OPC) ensures the suitable light polarization state at the optical input of SD-MZM, which is biased as close as possible to QP ( $V_{\text{bias}} = V_{\pi}/2$ ). We experimentally shifted the bias voltage and identified 8.2 V as the  $V_{\text{bias}}$  value that reduced nonlinearities at 6 and 28 GHz. The SD-MZM output signal, which can be expressed by

$$E_{\text{out}}(t) = E_0 \cos \left[ \frac{\pi}{2} \cdot \frac{V_{m1} \cos(\omega_{\text{RF1}} t) + V_{m2} \cos(\omega_{\text{RF2}} t + \varphi) + V_{\text{bias}}}{V_{\pi}} \right] \cos(\omega_0 t), \quad (3.6)$$

consists then of optical carrier and sidebands spaced by  $f_{\text{RF1}}$  and  $f_{\text{RF2}}$ , as illustrated in the inset from Fig. 3.4. It means both RF<sub>1</sub> and RF<sub>2</sub> are transmitted in the optical domain using the same laser wavelength. The  $\varphi$  term in Eq. 3.6 denotes the phase shift between the RF-driven signals.

In parallel, a media converter (MC<sub>1</sub>) receives video streams from a computer through the GbE interface and transmits them using the 1550 nm wavelength (also within the RF/video overlay band), which is combined to the 1560 nm optical carrier employing a CWDM coupler. The latter one properly offers a bidirectional channel for 1550/1310 nm wavelengths, as well as a transmission channel for the 1560 nm wavelength.

After 2-km fiber-optic transmission, a second CWDM coupler separates the optical carriers and launches them in two physical ways. The lightwave at 1550 nm goes through the first one, which connects a second media converter (MC<sub>2</sub>) for delivering the video stream to another computer. An additional wavelength (1310 nm) runs over such path on uplink for establishing a GbE full-duplex communication, in such a way the computers are visible to each other. The 1310 nm channel use is a requirement that come from the commercial media converter employed.

On the other hand, the 1560 nm carrier goes through the second path, which leads to a broadband photodetector. A variable optical attenuator (VOA) and an optical power monitor (OPM) are used for managing and monitoring the optical power at the PD input, respectively.

VOA and OPM support our experimental characterization and might be not required in a commercial deployment. Finally, the recovered RF signals are evaluated using a portable 50-GHz electrical spectrum analyzer (ESA). The results obtained with the described technique are reported on section 3.4 after the discussion on the challenges on the setup implementation.

### 3.3. RoF technique based on a dual-drive MZM

The analog RoF technique based on a DD-MZM, one of the main contributions of this thesis, consists of using the referred modulator for simultaneously modulating an optical carrier with two distinct RF-driven signals. Figure 3.5 presents the block diagram of the proposed approach, which takes the advantage of not requiring an external RF combiner, besides allowing independent bias voltages at the modulator upper and bottom arms. Since our goal is distributing 6 and 28 GHz RF signals on top of a GbE wired link, the schematic is similar to that from Figure 3.4, obviously replacing the diplexer and SD-MZM by DD-MZM.

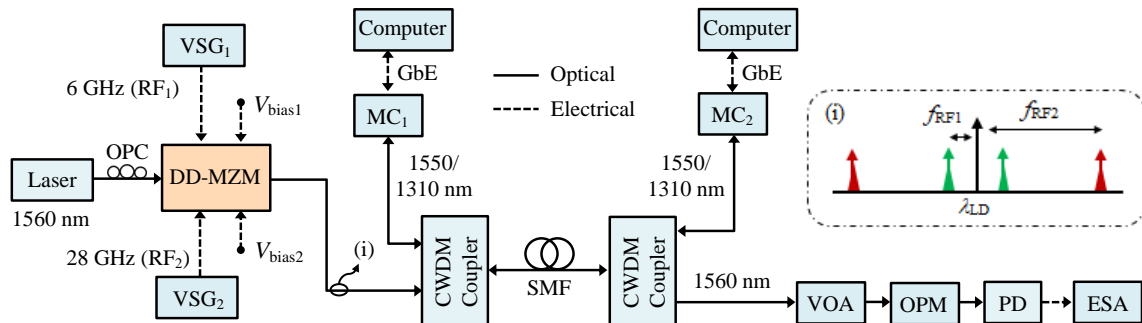


Figure 3.5 – Multi-band A-RoF technique based on a dual-drive Mach-Zehnder modulator.

In such approach, the electrical field at the DD-MZM output can be expressed as [140]

$$\begin{aligned}
 E_{\text{out}}(t) &= E_o \left\{ \cos \left[ \frac{\pi V_{e1}}{V_\pi} \right] + \cos \left[ \frac{\pi V_{e2}}{V_\pi} \right] \right\} \cos(\omega_o t) = \\
 &E_o \left\{ \cos \left[ \frac{\pi V_{m1} \cos(\omega_{\text{RF1}} t) + V_{\text{bias1}}}{V_\pi} \right] \right. \\
 &\left. + \cos \left[ \frac{\pi V_{m2} \cos(\omega_{\text{RF2}} t + \varphi) + V_{\text{bias2}}}{V_\pi} \right] \right\} \cos(\omega_o t), \quad (3.7)
 \end{aligned}$$

which also leads to an optical spectrum with optical carrier and sidebands spaced by  $f_{RF1}$  and  $f_{RF2}$ , as illustrates the inset from Fig. 3.5. However, Eq. 3.7 shows that  $E_{out}(t)$  might be managed as a function of  $V_{bias1}$  and  $V_{bias2}$ , which impact on the  $RF_1$  and  $RF_2$  electrical-to-optical conversion, respectively. This feature is in contrast to the SD-MZM-based RoF technique and enables reaching the desired DD-MZM operation point for both  $RF_1$  and  $RF_2$ .

The described methodology was experimentally investigated in case of properly biasing the modulator close to the quadrature point. The corresponding results are reported on section 3.4 and compared to that obtained with SD-MZM, taking into account the coexistence among all transmitted signals.

## 3.4. Performance analysis

### 3.4.1. Challenges and setup

The challenges on experimentally evaluating the analog radio over fiber techniques based on SD-MZM and DD-MZM are listed as follows:

- At this research stage, WDM couplers were not available in the laboratory. Therefore, we employed an optical splitter as optical coupler for performing the wavelength combinations. It imposes an insertion loss of 4 dB and the requirement of using an optical isolator at the MZM output. An optical circulator (OC) was employed for isolation purpose, due to the lack of an optical isolator. An optical power meter was connected to the third OC port for receiving any return signals. Hence, the 1310 nm optical carrier does not reach the modulator output;
- The splitter use allows the 1550 nm signal to reach the photodetector. An optical bandpass filter (OBF) was then employed for selecting the 1560 nm optical carrier with sidebands to be individually photodetected;
- The SD-MZM and DD-MZM available in the laboratory are from different manufactures and have distinct characteristics. SD-MZM is the FTM7939EK modulator from Fujitsu, which presents 8-dB insertion loss and 38-GHz minimum bandwidth (assuming the -3 dB point) [120], whereas DD-MZM regards the Photline MZDD-LN-10 modulator, which presents 4-dB insertion loss and 10-GHz minimum bandwidth [141]. This issue is expected to impact the results, mainly

because  $RF_2$  is centered at 28 GHz, i.e. beyond the 3-dB DD-MZM bandwidth. To deal with such limitation, we measured the transmission coefficient ( $S_{21}$ ) using the schematic from Figure 3.6(a), in which a network analyzer generates the RF-driven signal at 0 dBm and measures the photodetected RF signal from 300 kHz to 30 GHz. Figure 3.6(b) presents the system frequency response for both SD-MZM and DD-MZM, important to understand the next section results.

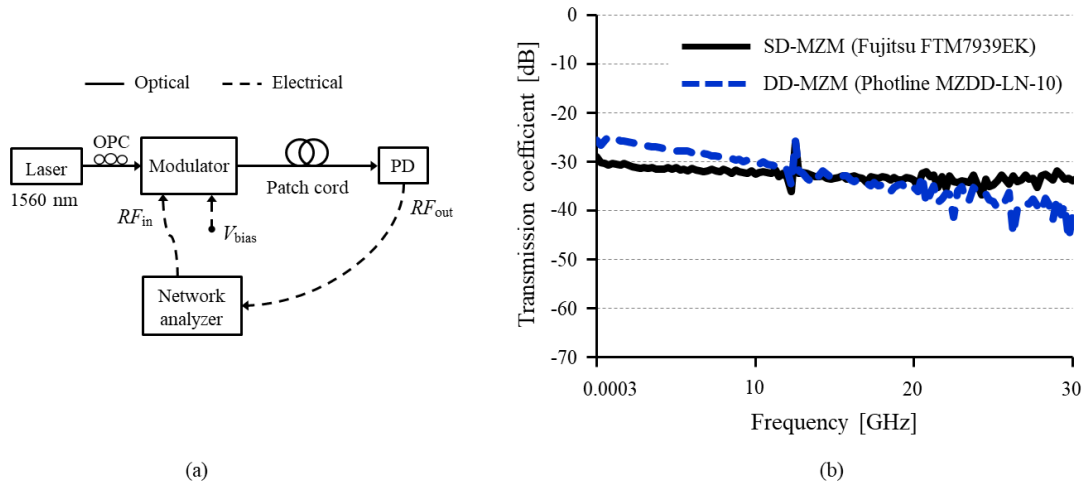


Figure 3.6 – Frequency response of the RoF system: (a) Schematic for realizing the  $S_{21}$  measurements; (b)  $S_{21}$  results for SD-MZM and DD-MZM.

Figure 3.7 presents the setup employed to investigate the A-RoF techniques, in which one can observe the optical switching between SD-MZM and DD-MZM, as well as the incorporated optical circulator, power meter, bandpass filter and splitters. LD and VSGs were set to provide 10 dBm power levels. Appendix A lists all devices and equipment employed in the experimental setups throughout this work, including model and manufacturer information.

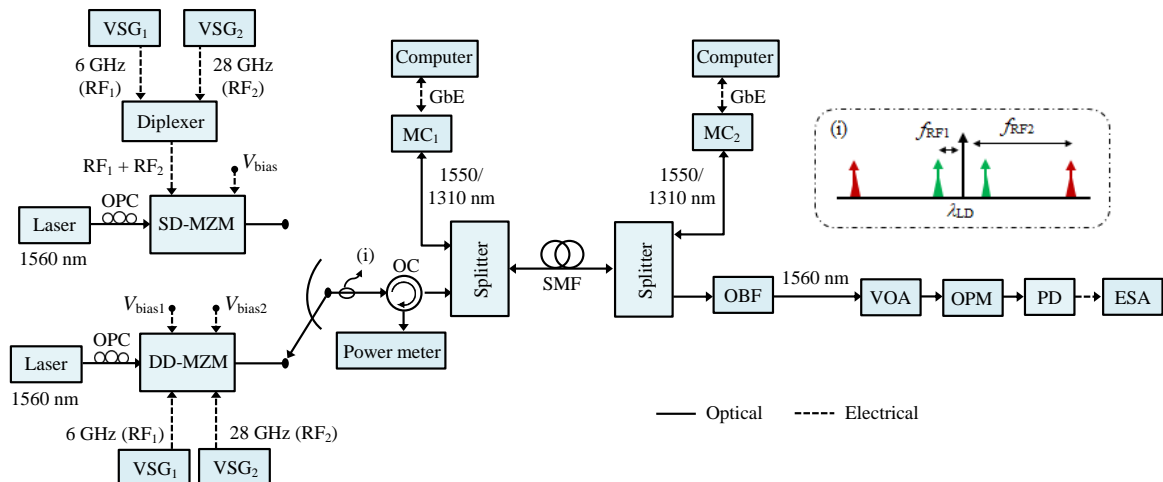


Figure 3.7 – Experimental setup for evaluating the A-RoF techniques based on SD-MZM and DD-MZM.

### 3.4.2. Experimental results

Figure 3.8 reports the SNR at the photodetector output for both analog RoF techniques. This experimental analysis takes into consideration the RF signals coexistence and the photodetector input power, which was varied from  $-16$  to  $-8$  dBm. Higher optical power levels at PD were not achieved in the experimental setup.

As reported in Figure 3.8(a), the SNR obtained with the SD-MZM-based approach reached values from 28.5 to 30 dB when transmitting only the 6 GHz RF-driven signal, and did not change significantly by turning RF<sub>2</sub> and the GbE communication on. In contrast, RF<sub>1</sub> transmission negatively influenced the SNR of the 28 GHz RF signal. For instance, SNR achieved 27 dB at 28 GHz in case of ensuring optical power = -9 dBm and individually transmitting RF<sub>2</sub>. However, a degradation of 7.5 dB was observed in the referred parameter when the 6 GHz RF-driven signal was turned on. Playing the video stream transmission did not impact the signal-to-noise ratio at 28 GHz. One can also note the obtained SNR at 28 GHz is lower than that achieved at 6 GHz for all considered optical power levels. It occurs as a consequence of the modulator and photodetector frequency response reported in Figure 3.6(b) (solid line), as well as the additional power losses imposed by the RF cables as the frequency increases. It is worth mentioning that SNR values around 30 dB for frequencies  $\leq 6$  GHz are in agreement with those from similar RoF techniques [71]. Although we did not find a coexistence analysis including the 28 GHz frequency band in the literature, it will be demonstrated on Chapter 5 that SNR of about 25 dB is sufficient for establishing communication in accordance with the 3GPP EVM<sub>RMS</sub> requirements. Therefore, the 7.5 dB SNR degradation at 28 GHz might compromise the RoF system performance and hinder the 6 and 28 GHz RF signals coexistence in case of using SD-MZM.

From Figure 3.8(b), one can observe the SNR results in case of employing DD-MZM. The SNR parameter of the 6 GHz RF signal achieved 37 dB and did not suffer significant degradations when RF<sub>2</sub> and the GbE communication were turned on. One can also note the achieved SNR is 7 dB higher than that obtained with the previous technique at this frequency. It is explained by the measured transmission coefficient using DD-MZM (dashed line in Figure 3.6(b)), which is above the solid line at 6 GHz probably due to the DD-MZM lower insertion loss. Despite the lower E/O conversion efficiency at 28 GHz, as a consequence of exceeding the modulator bandwidth specification in accordance with Figure 3.6(b), SNR degradation in this frequency due to the RF<sub>1</sub> transmission was reduced, i.e. assuming 1.9 dB

in case of ensuring optical power = -9 dBm. The DD-MZM independent RF inputs and bias voltages are the responsible for this result, since the electrical RF combiner is eliminated and there is a greater degree of freedom on managing  $E_{out}(t)$  to reduced nonlinearities at both 6 and 28 GHz frequencies. Again, playing the video stream transmission did not impact SNR at 28 GHz. The obtained results indicate a promising direction on employing DD-MZMs to support multi-band A-RoF systems. Therefore, DD-MZM was chosen for the three 5G system implementations described in the next chapters.

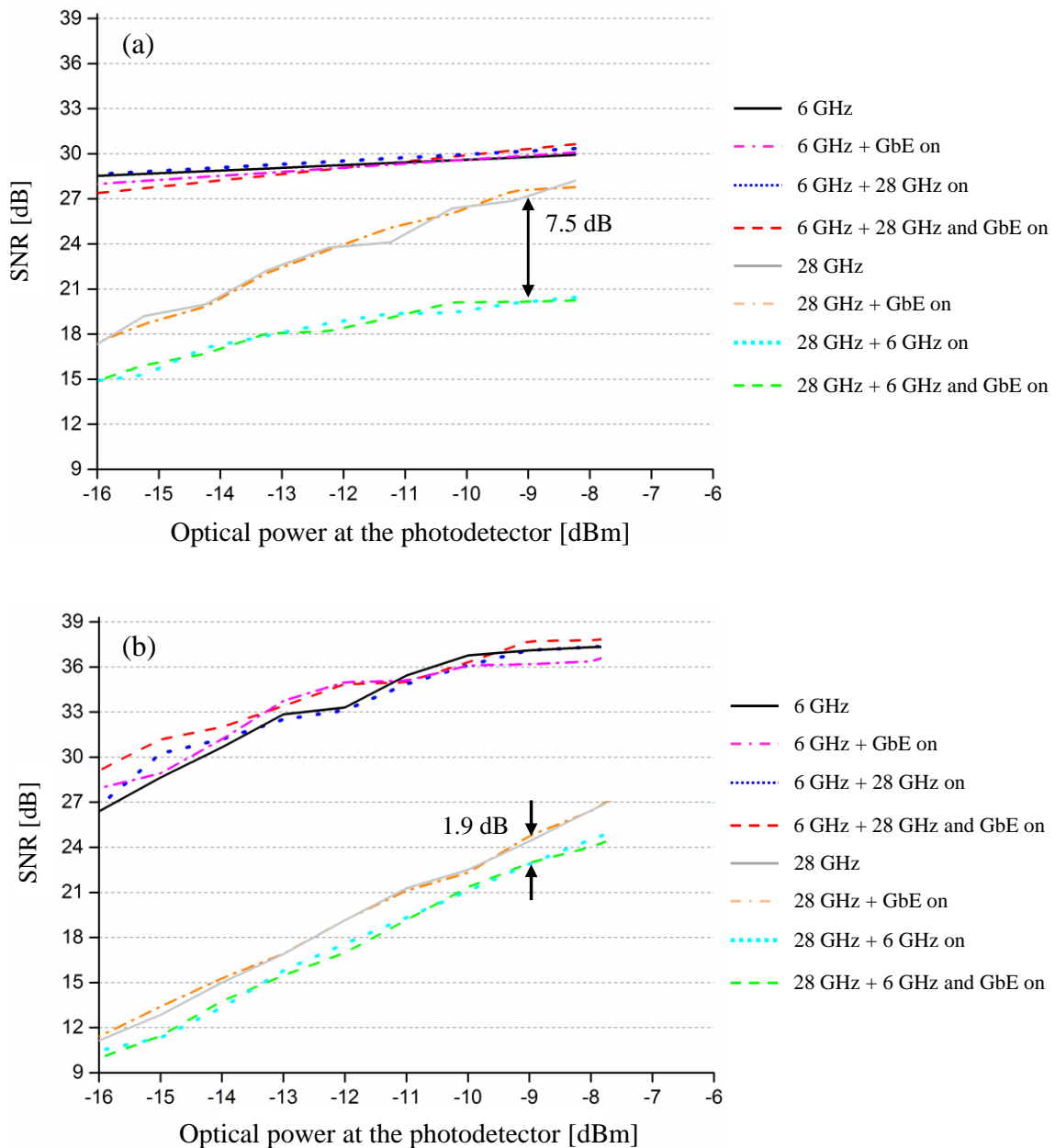


Figure 3.8 – SNR of the received 6 and 28 GHz RF signals as a function of the photodetector input power:  
 (a) RoF technique based on SD-MZM; (b) RoF technique based on DD-MZM.

## 4. Implementation 1: Integration of the 5G transceiver in a WDM overlay system

As stated earlier, 5G is expected to deal with challenge scenarios and, therefore, innovative technical solutions are required for both radio equipment and transport network. A possible 5G NR innovation refers to the applied waveform, whereas trends on network planning include RoF-based C-RAN.

New waveforms have been considered as candidate during the 5G NR design, and consequently, its transmission in RoF links has also been investigated. Tian et al. demonstrated the distribution of GFDM waveform over 1-km SMF using external modulation based on SD-MZM, as well as the need for approximately -8 dBm received optical power to ensure  $BER = 10^{-3}$  [62]. A FBMC signal transmission over fiber also using external modulation was reported in [63], in which EVM below 12.5% was achieved at 53 GHz for received optical power levels higher than -1 dBm. Additionally, Delmade et al. reported the distribution of OFDM, UF-OFDM and GFDM waveforms through 25-km intermediate frequency over fiber link using direct modulation [65]. In an initial step, such signals were distributed independently and evaluated in terms of EVM as a function of the received optical power. Next, OFDM and UF-OFDM waveforms were digitally added and transmitted together onto carrier frequencies below 2.25 GHz. The authors demonstrated the requirement of about -16 dBm received optical power to meet the 12.5% EVM limit (assuming 16-QAM) in the 4G/5G coexistence scenario, which imposed 5-dB power penalty over that with individual waveform transmission. These remarkable works addressed waveform generation using arbitrary waveform generator (AWG), signal transmission in a single spectral band and digital performance investigation as a function of the received optical power.

Regarding the transport network, RoF-based 5G analog fronthaul supporting multiple spectral bands has been expected to be deployed over passive optical networks. One of the proposed solutions in the literature addressing this issue refers to the WDM-PON, as reported in [61, 84]. The corresponding architectures consider independent RoF links, each one addressing a radiofrequency and operating with specific optical wavelengths, sharing the feed fiber. Another promising solution for enabling multi-band and multi-service fronthaul is using WDM-overlay, although it has not been widely exploited in the 5G context so far. For instance, Lee et al. successfully demonstrated a TDM-PON operating at 1490/1310 nm with five video channels (444–470 MHz) overlay at 1553.5 nm [87]. In such approach, the video

signals directly modulated an optical carrier from a DFB laser to be launched into the fiber jointly with the 1.25 Gbit/s TDM-PON data stream. The BER results indicated the TDM-PON error-free operation as a function of the video overlay usage. Additionally, N. Cheng proposed four WDM overlay schemes on top of TWDM-PON towards converged broadband services [88], whereas Shahpari et al. reported a field trial concerning a coexistence scenario with ultra-dense WDM-PON, GPON, NG-PON2 and RF (180–780 MHz) video overlay technologies [89]. The authors in [89] demonstrated that, for wavelength spacing higher than 7 nm, there were no significant interferences in the WDM-PON from the RF video overlay system. On the other hand, 3 nm wavelength spacing imposed 2 dB power penalty in the 10 Gbit/s WDM channel receiver sensitivity to maintain  $BER = 3.8 \times 10^{-3}$ .

This Chapter presents the integration of the 5G transceiver designed at Intel in a WDM overlay system using a DD-MZM towards multi-band 5G networks. It comprises the integration of GPON and RoF technologies in the same network infrastructure, with the aim of taking advantage of the existent optical network for 5G systems implementation. The referred RoF-based fronthaul architecture is illustrated in Figure 4.1, in which we propose to simultaneously distribute and transmit three data signals, namely: (a) GFDM signal generated by the 5G transceiver at 735 MHz, for covering remote areas as supercell (up to 100 km-reach) rural applications; (b) 26 GHz digital modulated signal for enabling eMBB; (c) baseband signal from a GPON for fiber-to-the-home applications. The goal is enabling

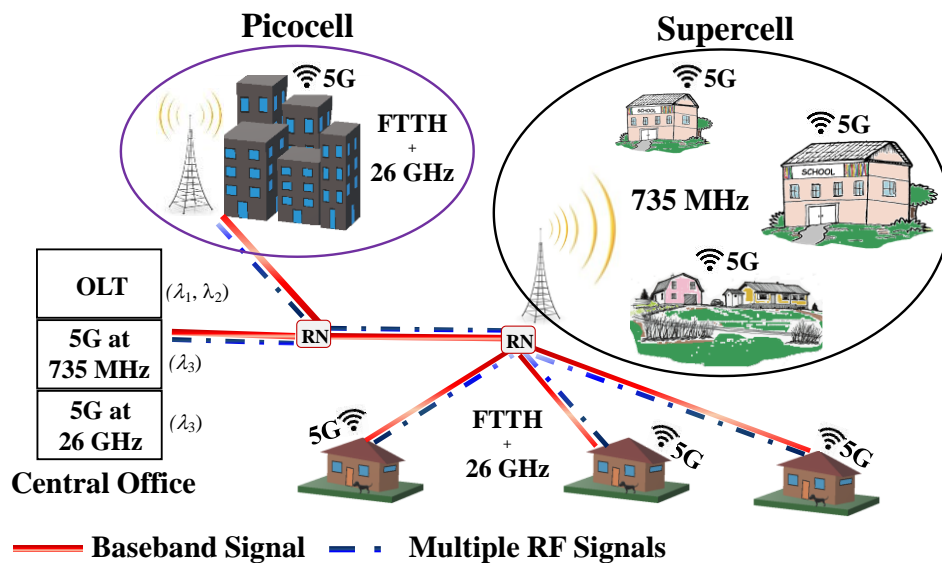


Figure 4.1 – Illustration of the 5G fronthaul using RoF technology.

multiple services, such as Internet access and broadband indoor mobile communications, as well as increasing wireless coverage in remote areas. We believe the proposed solution can further allow a significant CAPEX costs reduction and a network capillarity increment. For instance, in small cities, the telecommunication companies could rent the available optical infrastructure from FTTH Internet service providers as fronthaul for their 5G systems, rather than deploying a new optical network. It is worth mentioning the current proposal does not include F-OFDM signal transmission because this waveform was not implemented in the 5G transceiver in this research stage.

The contributions over the state of the art are the following ones: (a) the use of a 5G transceiver instead of arbitrary waveform generators to provide a 5G candidate waveform; (b) the employment of the analog RoF technique based on DD-MZM, which allows mitigating RF interferences in a coexistence scenario as reported in Chapter 3; (c) the simultaneous distribution of two 5G distinct bands, including the GFDM waveform, over a GPON using RoF and WDM overlay technologies; (d) the performance analysis of the received RF signals as a function of RF-driven signals power; (e) the WDM overlay use to support 5G applications.

The current Chapter is structured in two sections. Section 4.1 describes in details the proposed RoF-based fronthaul architecture for multi-band 5G systems, as well as the experimental setup. Section 4.2 presents the experimental performance analyses and results of GFDM, 26 GHz and baseband signals running over the same optical network infrastructure.

## 4.1. The proposed architecture

Figure 4.2 depicts a block diagram of the proposed RoF-based fronthaul architecture, exploiting a WDM overlay system. The scheme has been divided into two main parts: central office and remote unit. At the central office, the baseband signal running over GPON is provided by using an Ethernet Tester (ET<sub>1</sub>) and an OLT at 1490 nm (the GPON downlink wavelength), which is also connected to a server for providing Internet services. The 5G transceiver generates the first RF-driven signal (RF<sub>1</sub>), corresponding to a 100 Mbit/s GFDM signal at 735 MHz, and the VSG provides a 26 GHz wideband signal, giving rise to the second RF-driven signal (RF<sub>2</sub>). Both RF<sub>1</sub> and RF<sub>2</sub> are modulated by using DD-MZM, which is fed by a 1560 nm continuous wave (CW) optical carrier and biased with different bias voltage. Once again, the choice for the 1560 nm wavelength allows addressing the RF/video

overlay band specified by ITU-T and the channel grid of the optical components available in the laboratory. An optical polarization controller ensures the suitable light polarization state at the DD-MZM optical input. Two optical carriers (1490 and 1560 nm) are then combined using a WDM coupler to be launched at the same optical fiber. As reported on Chapter 3, DD-MZM mitigates RF interferences arising from the non-linearity of the modulation process, since  $RF_1$  and  $RF_2$  independently drive the modulator using its upper and bottom electrical inputs, with distinct and optimized bias voltages.

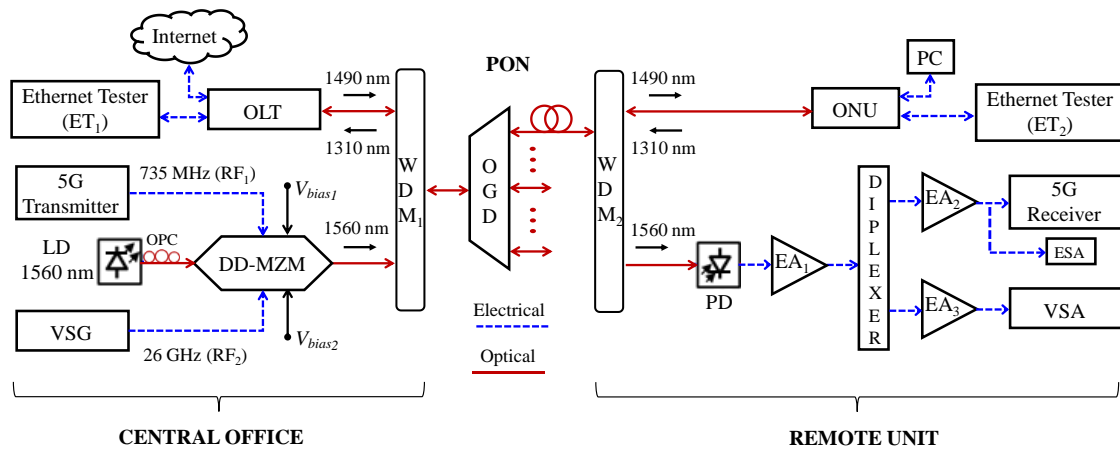


Figure 4.2 – Block diagram of the RoF-based fronthaul architecture for multi-band 5G systems: LD-laser; OLT-optical line terminal; VSG-vector signal generator; OPC-optical polarization controller; DD-MZM-dual-drive Mach-Zehnder modulator; OGD-optical general distributor; PD-photodetector; ONU-optical network unit; EA-electrical amplifier; ESA-electrical spectrum analyzer; VSA-vector signal analyzer; PC-personal computer.

The optical general distributor (OGD) is one of the optical components of a GPON and is applied for signal distribution. At the remote unit, there is a second WDM coupler to separate the optical carriers into different fibers. The 1490 nm carrier is received by an ONU and delivered to a second Ethernet Tester ( $ET_2$ ) in the loopback function, i.e. configured to route incoming data to the output port without any processing. In this way, the baseband signal is launched back into the system at 1310 nm (the GPON uplink wavelength) and throughput and latency are measured by  $ET_1$ .

Finally, the optical carrier at 1560 nm from the second output port of the WDM coupler is converted to the electrical domain by using a *p*-intrinsic-*n* (PIN) photodetector. An Erbium doped fiber amplifier (EDFA) might be used before PD to compensate the DD-MZM, OGD and WDM couplers insertion losses. Both RF signals feed the first amplification stage, which is a wideband electrical amplifier ( $EA_1$ ). A diplexer separates the two signals and each one is further amplified by a second stage of amplification ( $EA_2$  and  $EA_3$ ). The 735 MHz

GFDM signal is analyzed by the 5G receiver block, whereas the 26 GHz signal is evaluated by a vector signal analyzer (VSA). In a fiber-wireless network, these two RF signals would be radiated by using antennas after EA<sub>2</sub> and EA<sub>3</sub>.

Figure 4.3 displays a photography of the experimental setup, which is in accordance with the schematic from Figure 4.2. Two TSW900ETH Ethernet testers from WISE provide 1 Gbit/s to the OLT electrical interface. A 20028S OLT from Parks transmits and receives baseband optical signals at 1490 nm and 1310 nm, respectively. The 5G transceiver has been set to operate in continuous data transfer mode and 5/6 code rate with polar coding to generate a 100 Mbit/s GFDM signal with 256-QAM modulation at 735 MHz (RF<sub>1</sub>). A M9505A broadband arbitrary waveform generator from Keysight generates baseband 16-QAM signals and a PSGE8267D vector signal generator, also from Keysight, upconverts it to 26 GHz (RF<sub>2</sub>). The CW laser has been set to operate at 1560 nm with 11 dBm optical power. Both DD-MZM upper and bottom arms are biased close to the quadrature point by applying the DC voltages  $V_{\text{bias1}}$  and  $V_{\text{bias2}}$  of 2.8 V and 2.9 V, respectively. In addition, a WDM coupler (WDM<sub>1</sub>) from Haphit, with an insertion loss of 2 dB, has been used to couple the modulated optical signal from DD-MZM and the one from OLT. The resultant signal is launched into a GPON. The geographically-distributed optical network is composed of 27 km of underground and bend-insensitive fiber-optic cables (inside the buildings). In this way, we could experimentally evaluate the integration of the 5G transceiver in a WDM overlay system, under real channel conditions.

At the remote unit, WDM<sub>2</sub> decouples the baseband and RF-modulated optical signals. ONU receives the -20 dBm optical power at 1490 nm and converts it to Ethernet for feeding ET<sub>2</sub>. The returning traffic is inserted into the network by using the ONU upload wavelength at 1310 nm and ET<sub>1</sub> realizes the performance analysis, by means of measuring throughput and latency. A second ONU electrical port is connected to a personal computer for Internet and video stream access. In parallel, a XPDV2150RA photodetector from u2t receives 3 dBm optical power at 1560 nm and after EA<sub>1</sub>, a Marki DPX-1721 diplexer separates the resultant 735 MHz and 26 GHz signals, which are properly amplified by EA<sub>2</sub> and EA<sub>3</sub> respectively. We have used a Keysight FieldFox Microwave Analyzer N9952A and a vector signal analyzer Z-Series DSAZ632A for the RF signals analyses. GFDM performance has been evaluated at the 5G receiver.

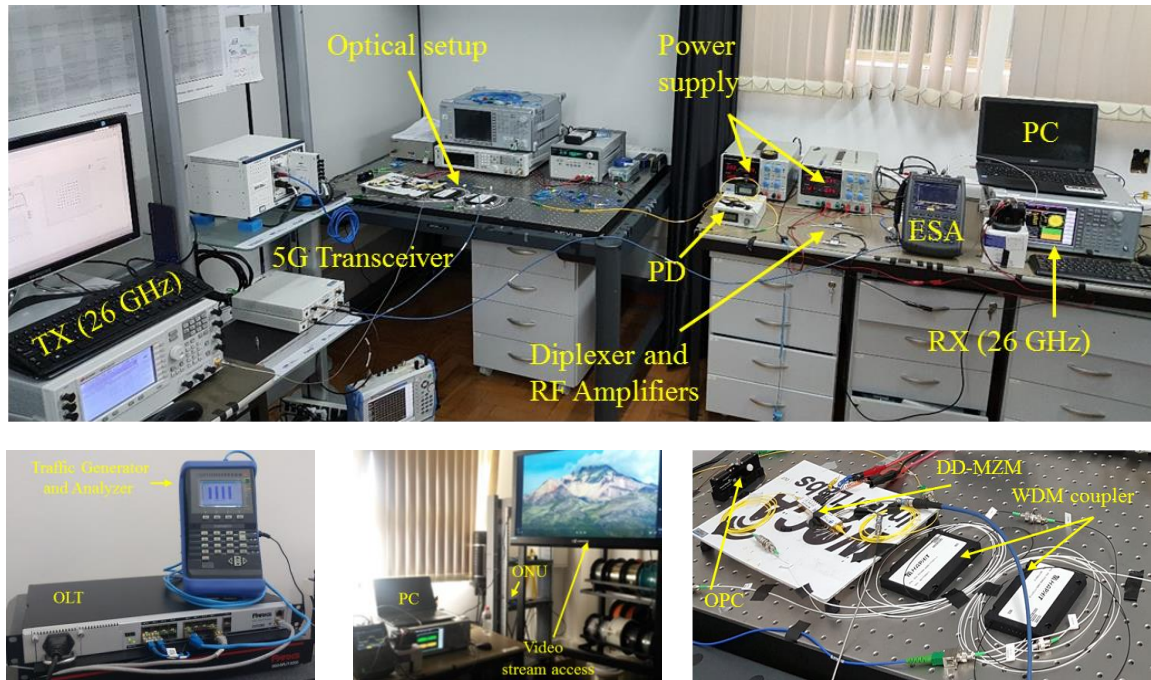


Figure 4.3 – The experimental setup.

The main challenges for implementing the described setup are listed as follows:

- At the beginning of this step, there was no GPON deployed in the laboratory, despite the available geographically-distributed fiber-optic infrastructure. To solve this issue, a partnership was established with PARKS company, which provided the GPON equipment (OLT and ONUs) and a training course. A partnership was also established with Fibracem company, which donated fiber-optic cables to support the GPON implementation by connecting a cluster of research laboratories. Therefore, before working on the complete experimental setup from Figure 4.3, it was necessary a dedicated effort to the GPON deployment and operation;
- Once the innovative 5G transceiver was developed, it has been constantly upgraded and employed for several field trials and demonstrations, even outside Brazil. Therefore, our experiment had to be carried out in short time window in which the transceiver was available for this purpose.
- Interfacing the M9505A arbitrary waveform generator with the PSGE8267D vector signal generator for providing the desired 26 GHz wideband signal for the first time was not a simple task. The technical support from Keysight was essential to overcome such challenge.

- Configuring the Ethernet testers for our purpose and interfacing them with OLT demanded study, since we had no previous experience with such traffic generators. Knowledge was acquired in a hands-on process in parallel to the setup implementation.

## 4.2. Experimental results

This subsection presents the experimental results of the proposed RoF-based multi-band 5G system using WDM overlay. The investigation addresses five different scenarios for the network performance analysis.

Scenario 1 (S1) considers the back-to-back (B2B) configuration for both RF and baseband signals, namely: RF transmitters were directly connected to the RF receivers; OLT, excited by ET<sub>1</sub>, was directly connected to ONU, which was attached to ET<sub>2</sub>. Scenario 2 (S2) arises from activating the GPON data stream and GFDM-based signal at 735 MHz, thus transporting them through the optical network. Scenario 3 (S3) regards the transportation of the baseband and 26 GHz signal over the WDM overlay system. Scenario 4 (S4) comprises baseband and both RF signals, transported simultaneously through the proposed architecture. Scenario 5 (S5) consists of turning the baseband signal from GPON off and keeping both RF signals active.

Scenario 4 is the focus of our analysis because it takes into account the coexistence of the baseband and RF signals. A comparison between S4 and S1 has been realized. Scenarios 2, 3 and 5 have been briefly investigated, with the aim of certifying the coexistence of GPON and the multi-band RoF approach.

The optical spectrum at the DD-MZM output for S4 is reported in Figure 4.4. One can note the presence of the optical carrier at 1560 nm, as well as the upper and lower sidebands of the first and second order from RF<sub>2</sub> (26 GHz). The first order sidebands are dominant, since they are approximately 30 dB above the second order ones. The contribution of the GFDM-based RF<sub>1</sub> (735 MHz) is not visible due to the optical spectrum analyzer (MS9740A) resolution, which is 0.07 nm. In any case, the obtained spectrum is in agreement with the expected form in case of biasing MZM at the quadrature point. This indicates there is no apparent distortion for the RF<sub>1</sub> and RF<sub>2</sub> simultaneous modulation.

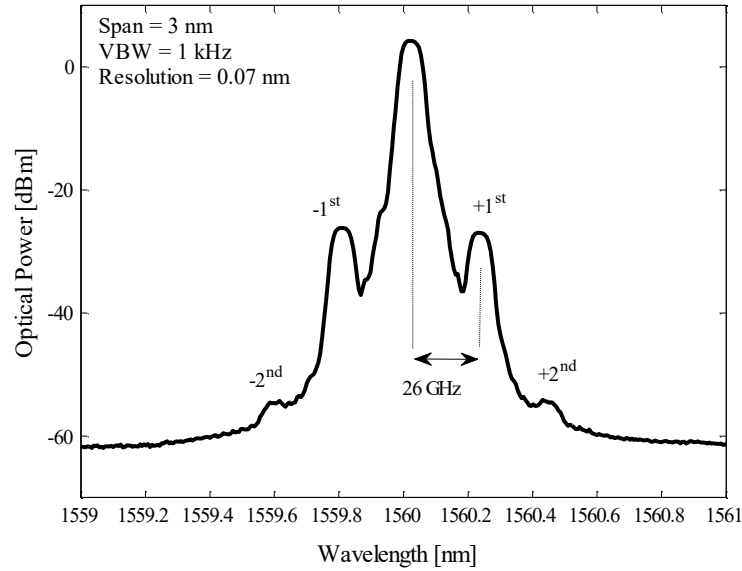


Figure 4.4 – Measured optical spectrum at the DD-MZM output.

### 4.2.1. GFDM analysis

The GFDM digital performance has been evaluated in terms of MER, which is the figure of merit used by the 5G receiver. MER is a performance metric to quantify the digital modulation quality, defining the dispersion of the QAM symbols. In practice, MER and EVM are different ways of representing the same measurement. Such parameters are closely related and one can generally be computed from the other, as reported in the Appendix B [142, 143]. MER has been adopted as the 5G prototype performance metric to take benefit of the CRR team background on digital TV systems, which commonly define MER requirements [142, 144]. As an example, typical MER values from digital TV transmitters range from 34 to 43 dB (the best case) depending on the transmission power and network configuration [145, 146]. It is worth highlighting that the 5G NR standard specifying EVM limits [91] was launched after the 5G prototype initial design.

Figure 4.5(a) presents the performance analysis of the GFDM-based 5G transceiver, integrated with the fronthaul, as a function of RF power. B2B configuration demonstrates the developed prototype is able to offer MER of at least 40 dB from -20 dBm to 10 dBm power levels. By evaluating Scenario 4 without RF amplifiers, i.e. without adding RF gain and noise, one can note that there is no significant penalty (maximum of 0.7 dB) in the received MER for RF-driven signals up to -5 dBm. For higher  $RF_1$  power levels ( $P_{RF1}$ ), MER decreases due to modulation and photodetection process, which starts to generate undesired intermodulation components [44]. It is worth mentioning the received electrical power is 30 dB below from

that of B2B, which means the RoF system imposes a power loss of 30 dB. This power loss, which is not shown in Figure 4.5(a), has been experimentally observed by measuring the photodetected RF power ( $P_{\text{RFout}}$ ) and comparing it with the RF-driven power ( $P_{\text{RFI}}$ ) at the MZM input. The attenuation imposed by the fiber-optic link and E/O and O/E conversion process justifies the fact of  $P_{\text{RFout}}$  is 30 dB below from that at the MZM input.

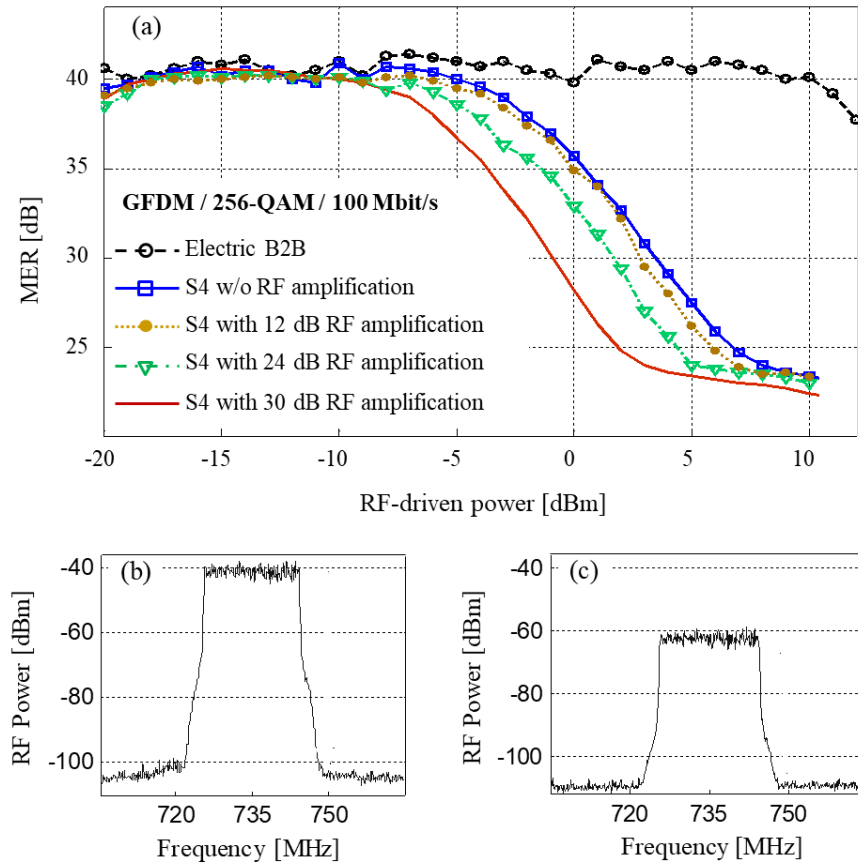


Figure 4.5 – GFDM-based 5G transceiver performance at 100 Mbit/s: (a) MER as a function of the RF-driven power and RF amplification; (b) Electrical spectrum from the B2B configuration; (c) Electrical spectrum from the integrated RoF and GPON with electrical amplification of 12 dB.

The penalties on the MER parameter appear at a lower value of input power when electrical amplifiers are employed for increasing the RF output power ( $P_{\text{RFout}}$ ). Degradations are observed for  $P_{\text{RFI}}$  higher than -6 dBm and -7 dBm for 12 and 24-dB RF amplification, respectively. For  $P_{\text{RFI}}$  equals -10 dBm, a SNR of 60 dB has been obtained in S1, whereas this parameter reached 47 dB in S4 with RF amplification of 12 dB, as reported in Figures 4.5(b) and 4.5(c). Moreover, there were no penalties in the out-of-band emission, which is a remarkable advantage of using GFDM for 5G applications, as previously mentioned.

A comparison between S1 and S4 for  $P_{\text{RFout}} = P_{\text{RF1}}$ , i.e. a condition in which the photodetected RF power becomes equal to the RF-driven power by applying 30 dB RF amplification for the GFDM signal, allows for investigating the impact of integrating the 5G transceiver with a GPON without 30 dB power penalty. According Figure 4.5(a), when the RF amplification of 30 dB is employed, MER keeps close to 40 dB for  $P_{\text{RF1}}$  up to -9 dBm and suffers additional degradation for higher power levels, e.g. 11.9 dB regarding the B2B for  $P_{\text{RF1}} = 0$  dBm, due to the resultant noise figure ( $\approx 5$  dB) and nonlinear distortions from the amplification stages. These distortions have been reduced by the digital pre-distortion, as can be seen in Figure 4.6(a). One can observe an improved SNR from 25.4 to 36.3 dBc. Figures 4.6(b) and 4.6(c) show the MER performance with and without DPD, where it can be seen that DPD introduces a gain of 10.1 dB in the achieved MER.

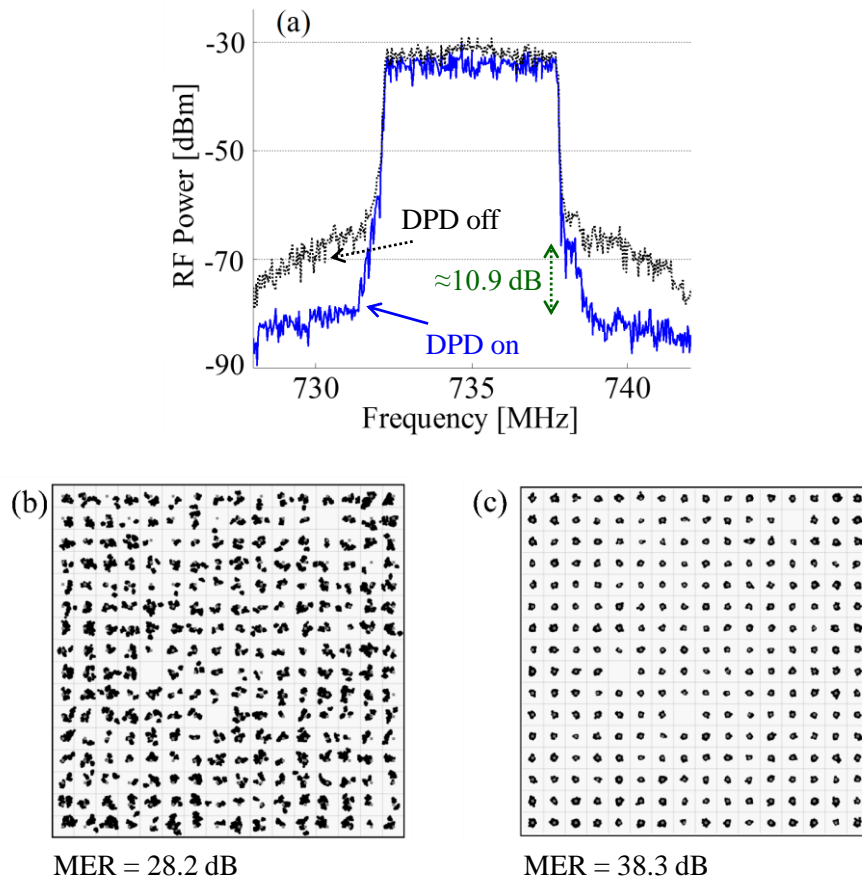


Figure 4.6 – DPD impact on Scenario 4 for  $P_{\text{RF1}} = P_{\text{RFout}} = 0$  dBm: (a) Received RF spectra; (b) Constellation with DPD off; (c) Constellation with DPD on.

In addition, DPD has also reduced the distortion level from modulation and photodetection process, since the resultant MER (38.3 dB) is 2.6 dB higher than that of

scenario 4 without RF amplification and DPD. Considering 30 dB RF gain at  $P_{RF1} = 0$  dBm compared to B2B configuration, the MER parameter has been increased from 28.2 dB (DPD off) to 38.3 dB (DPD on). The presented results, i.e. MER increasement with DPD on, have been kept unchanged for Scenarios 2 and 5, indicating the GFDM over fiber signal is able to coexist with GPON and RoF-based 26 GHz signals without penalties in the proposed architecture. Moreover, reaching  $MER > 38$  dB at the remote unit might be considered as an attractive achievement, since this MER value is in accordance with that expected from commercial transmitters.

The performance of the GFDM-based 735 MHz signal has been investigated at distinct network access points ( $AP_1$ ,  $AP_2$  and  $AP_3$ ), with the purpose of analyzing a point-to-multipoint signal distribution, which is a key feature of PON. The fiber distance between the central office and access point was 0.5, 2.0 and 12.5 km for  $AP_1$ ,  $AP_2$  and  $AP_3$ , respectively. Table 4.1 reports the measured  $P_{RFout}$  and MER for all APs, assuming 12-dB RF amplification. The received RF power has been reduced because of the optical link attenuation, which is the sum of the optical fiber attenuation ( $\approx 0.2$  dB/km) with the connectors and splicers losses [44]. The measured RF power difference between  $AP_1$  and  $AP_3$  was 7 dB. In any case, in spite of the power reduction, MER has been kept around 40 dB, as in the B2B configuration, for the three evaluated APs. The RoF-based fronthaul on top of GPON has allowed  $EVM_{RMS}$  below 0.8%, which does not compromise the 735-MHz GFDM wireless transmission at APs. As a conclusion, the PON capillarity might be explored toward 5G systems implementation.

Table 4.1 – GFDM point-to-multipoint distribution in the WDM overlay system.

	$AP_1$	$AP_2$	$AP_3$
Fiber length [m]	500	2,000	12,500
$P_{RFout}$ [dBm]	-32	-36	-39
MER [dB]	40.1	39.9	39.6

#### 4.2.2. 26-GHz analysis

The 24.25–27.5 GHz frequency range, also referred as 26 GHz in the literature, has been identified as a 5G pioneer band in the mm-waves spectrum although the carrier

frequencies are below 30 GHz [22, 23]. Based on such terminology, the 26 GHz RF-driven signal ( $RF_2$ ) has been considered within the mm-wave band in this work.

The  $RF_2$  performance in the proposed fronthaul architecture has been evaluated by analyzing the measured EVM in the receiver side. Our goal was exploiting the available bandwidth from this frequency range for Gbit/s throughput. Therefore, we set as the target to attain from 100 Mbit/s to 1 Gbit/s using 16-QAM, which results in occupied bandwidth up to 287.5 MHz. The 16-QAM modulation order was chosen for robustness.

Figure 4.7 reports the EVM parameter as a function of  $RF_2$  power levels ( $P_{RF2}$ ) and bitrate in scenario 4. It is worth mentioning  $P_{RF1}$  has been set to 0 dBm with benefit of digital pre-distortion and the cascaded  $EA_1$  and  $EA_3$  have provided a total RF gain of 50 dB for the 26 GHz signal. One can identify the  $P_{RF2}$  optimum values that improve the digital performance, namely: -2 dBm, 0.5 dBm and 1 dBm for 100 Mbit/s, 500 Mbit/s and 1000 Mbit/s, respectively. For these  $RF_2$  power levels,  $EVM_{RMS}$  degradation imposed by S4 relative to B2B was 1.1% for 100 Mbit/s and 2.5% for 1 Gbit/s.  $EVM_{RMS}$  between 2.18% and 5.70% has been observed when the bit rate has been increased from 100 Mbit/s to 1 Gbit/s. The 12.5% 3GPP- $EVM_{RMS}$  requirement for 16-QAM [91] has been met with at least 6.8% margin, in such way wireless transmission is possible at remote unit.

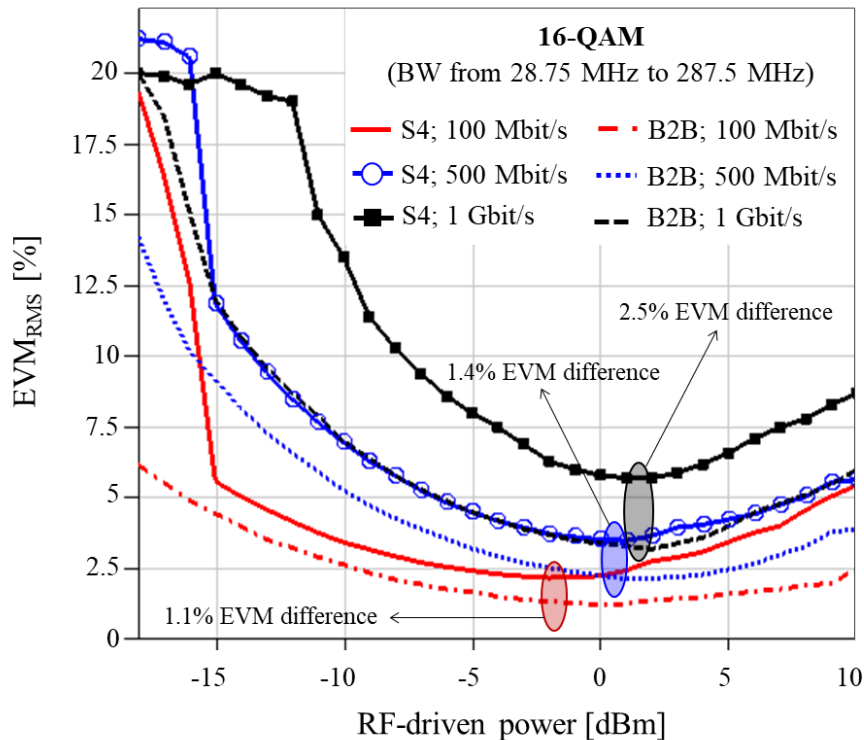


Figure 4.7 – EVM as a function of the RF-driven power and bitrate for the 26 GHz signal.

From Figure 4.7 one can also observe that  $EVM_{RMS}$ , measured with the vector signal analyzer, varied as a function of the bit rates in addition to the RF power. This can be justified by the strategy used to attain from 100 Mbit/s to 1 Gbit/s throughput. Such strategy was fixing the modulation order as 16-QAM and increasing the RF<sub>2</sub> bandwidth, since a large amount of spectrum is available in the 26 GHz band. Therefore, as the signal bandwidth increased, SNR and symbols energy decreased, impacting the EVM. The abrupt  $EVM_{RMS}$  degradation for  $P_{RF2} < -12$  dBm in scenario 4 occurs due to the vector signal analyzer sensibility, a condition in which the symbols are not identified in the constellation and VSA displays  $EVM_{RMS}$  close to 20%.

Figures 4.8(a), 4.8(b) and 4.8(c) report the performance of the received 1 Gbit/s RF signal in terms of spectrum, constellation and eye diagram, respectively. One can note spectrum with no apparent distortion, well-defined symbols in the constellation and open eye diagram. Regarding the performance comparison among scenarios 3, 4, and 5, there were no significant penalties among them, for RF-driven powers up to 5 dBm, which reinforce the successful coexistence of GPON data stream and RF signals in the proposed RoF-based WDM overlay network. A possible interference on the 26 GHz signal is due to simultaneous modulation with GFDM and it was noticed only for  $P_{RF1}$  higher than 5 dBm. In that case, the  $EVM_{RMS}$  parameter has degraded from 5.7 to 8.0%.

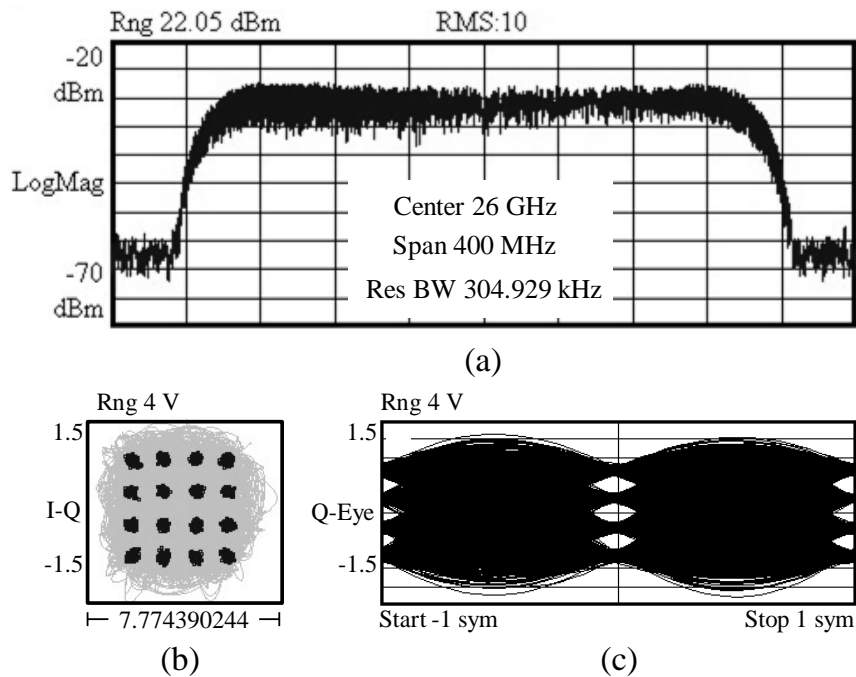


Figure 4.8 – Performance of the received 26 GHz RF signal at 1 Gbit/s for  $P_{RF2} = 1$  dBm: (a) RF spectrum; (b) Constellation; (c) Eye diagram.

The obtained results of the 26 GHz point-to-multipoint analysis are summarized in Table 4.2, which presents  $P_{\text{RFout}}$  and  $\text{EVM}_{\text{RMS}}$  as a function of the distance between the central office and access point. As reported on Chapter 2, the RoF distribution at high frequency, including 26 GHz, suffers with periodic power fading due to the optical fiber chromatic dispersion. We have overcome this drawback by setting APs as far as possible of the fading nodes, which are the optical fiber lengths in which the RF power is minimum. In commercial networks, this solution may not be viable due to the operational issues from the provider; however other strategies can be used for overcoming the power fading, e.g. dispersion compensation or optical single-sideband modulation. The 3GPP  $\text{EVM}_{\text{RMS}}$  limit of 12.5% has been met with margin in all access points, reinforcing the possibility of implementing multi-band 5G system over the PON capillarity. It is worth mentioning that digital pre-distortion has not been applied in this analysis, once the 26 GHz signal comes from a commercial vector signal generator with the DPD feature unavailable at this time. Using DPD could further enhance the RF<sub>2</sub> digital performance and  $\text{EVM}_{\text{RMS}}$  margins at APs, enabling more robustness or wireless coverage extension. This will be demonstrated on Chapter 5.

Table 4.2 – 26-GHz point-to-multipoint distribution in the WDM overlay system.

	AP <sub>1</sub>	AP <sub>2</sub>	AP <sub>3</sub>
Fiber length [m]	500	2,000	12,500
$P_{\text{RFout}}$ [dBm]	-48.7	-51.4	-55.2
$\text{EVM}_{\text{RMS}}$ [%]	5.75	6.27	7.92

### 4.2.3. GPON analysis

Figure 4.9 reports the throughput and latency measurements of the baseband signal transmitted over GPON, as a function of the frame size and proposed scenarios. The larger is the frame, the higher the throughput, which has been kept approximately the same in all evaluated scenarios for the corresponding frame sizes. It has been achieved more than 907 Mbit/s by using frames with 1518 Bytes, as can be observed in Figure 4.9(a). Similarly, baseband and RF signals coexistence in the WDM overlay system does not affect the latency, since it has been kept approximately constant for all scenarios for the corresponding frame sizes. The maximum latency was only 128.1  $\mu\text{s}$  for the 1518 Bytes package, as showed in Figure 4.9(b). It is worth mentioning that the GPON throughput has been limited by the

Ethernet tester data rate (1 Gbit/s), since this traffic generator has provided the baseband signal to the OLT electrical interface. GPON has not achieved 1 Gbit/s, provided by the Ethernet tester, even for the back-to-back scenario (S1), due to the transmission protocol and frame encapsulation imposed by OLT, when using its electrical interface. The throughput and latency measurements by taking the point-to-multipoint distribution into consideration have also been considered successful, since they were in agreement with the expected behavior of a GPON. Additionally, the GPON impact-free operation as a function of the investigated scenarios, which apply RF overlay using WDM, is in accordance with the results presented in [87, 89].

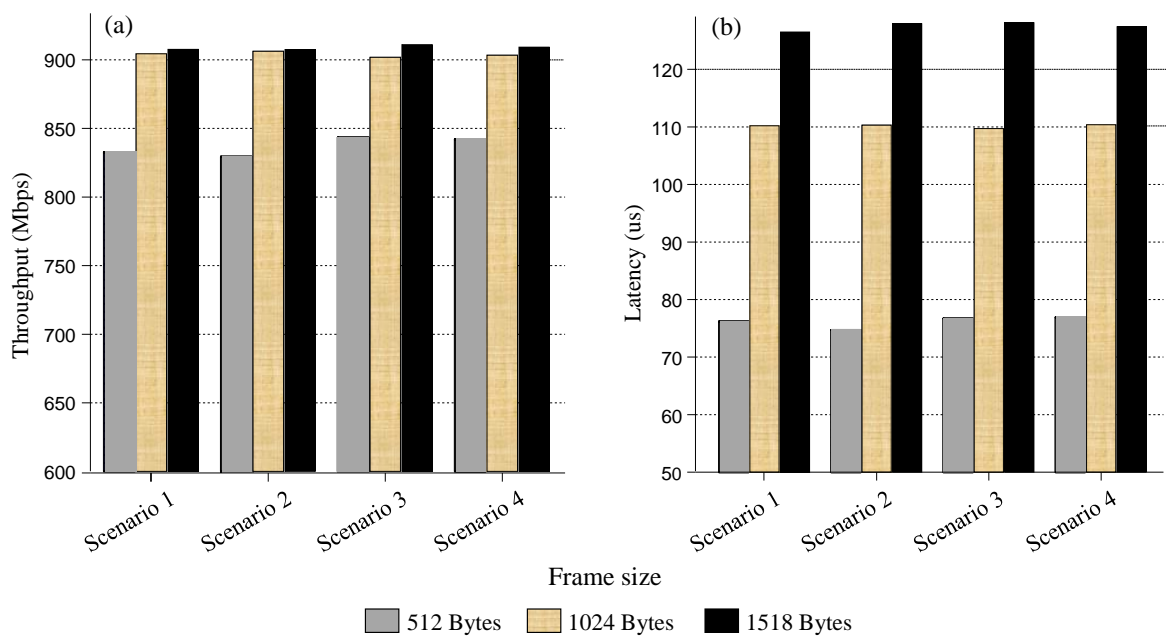


Figure 4.9 – GPON performance as a function of frame sizes and scenarios: (a) Throughput; (b) Latency.

## 5. Implementation 2: DSP-based flexible-waveform and multi-application 5G fiber-wireless system

Remarkable studies have been published in recent years related with multi-application and fiber-wireless (FiWi) systems for 5G. The publications deal with different technological aspects, ranging from RoF-based multi-service delivery to new waveforms and mm-waves FiWi transmissions. The coverage of diverse applications using the same fiber has been addressed in [70], although still out of the 5G context. The authors reported a three-band transport system based on direct and external modulation to provide RoF (at 6 GHz), FTTx (baseband) and CATV (channels 2-78) integrated services. It was demonstrated 1 dB power penalty between RoF and FTTx applications for reaching  $BER < 10^{-5}$ , as well as carrier-to-noise ratio (CNR) higher than 50 dB for CATV signals after 80-km fiber-optic link. Additionally, an analog intermediate frequency over fiber fronthaul link able to provide simultaneous 4G and 5G services was presented in [65]. Such applications were investigated by directly modulating an optical carrier with LTE and UF-OFDM signals, and as discussed on Chapter 4, the 12.5% EVM limit (assuming 16-QAM) was met in the 4G/5G coexistence scenario. Both the above mentioned works focused on the radio over fiber link and did not explore wireless transmission after the photodetection process.

Regarding FiWi systems, Bi et al. investigated the F-OFDM waveform transmission through 20-km optical fronthaul followed by a 6 GHz wireless link [76]. The authors reported 16- and 64-QAM EVM results close to 4% for received optical power levels higher than -23 dBm, but did not mention the accomplished distance. A mm-wave (57-64 GHz) FiWi system with Gbit/s throughput was presented in [80], in which 7-km IFoF fronthaul link with 5-m wireless transmission after electrical upconversion at the RRU were combined. An aggregate capacity of up to 24 Gbit/s exploiting 7.2-GHz electrical bandwidth over the FiWi channel was achieved, as well as EVM values about 7.0% and 7.5% for QPSK and 16-QAM signals, respectively. Moreover, Morant et al. demonstrated a FiWi system supported by photonic beamforming, in which multi-beam capability was confirmed by providing 26.0- and 17.6-GHz signals simultaneously [81]. The network enabled also to modify the 26-GHz beam steering as a function of the laser wavelength. EVM after 16-QAM wireless transmission reached about 7% for -3 dBm optical power level at the photodetector. It is worth mentioning that previous works rely on using technical solutions compatible with 5G, e.g. mm-waves and new waveforms, but do not employ the 5G NR standard.

This Chapter is a progress on the previous one and presents the implementation of a DSP-based flexible-waveform and multi-application 5G FiWi system. Figure 5.1 illustrates our proposal, in which a RoF-based fronthaul uses a PON infrastructure for integrating 5G systems operating over multiple frequency bands, as well as machine-to-machine (M2M) and fiber-to-the-home applications. The Internet/mobile integration physically occurs into the central office, which accommodates OLT and BBUs. The RF signals are simultaneously distributed via optical links at the same wavelength ( $\lambda_1$ ), between BBU and RRHs, before being radiated in downlink, obviously after direct detection and electrical amplification. In this way, we believe that one or more 5G mobile services can be further exploited by telecom providers, as a function of the user demands, resulting in flexibility and CAPEX costs reduction, as well as saving time deployment. An extra wavelength could be allocated for uplink communication from RRH to BBU.

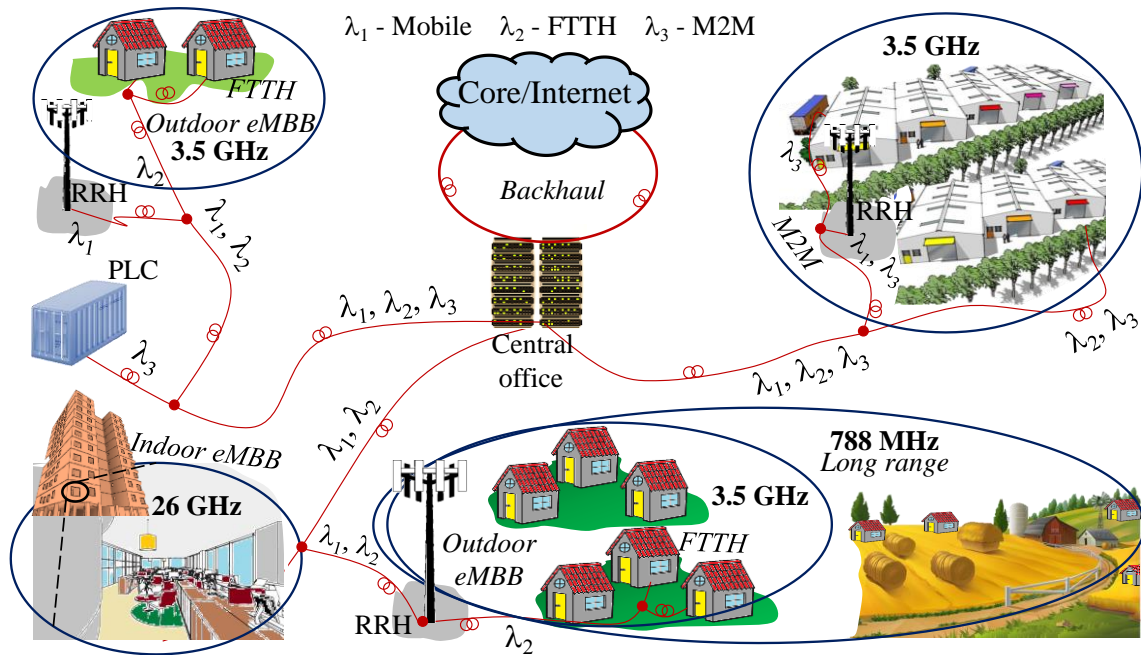


Figure 5.1 – Multi-application 5G fiber-wireless system proposal.

The following 5G applications are going to be considered in our demonstration: transmission of OFDM, GFDM and F-OFDM signals generated by our evolved DSP-based 5G transceiver at 788 MHz toward long range cells (up to 100-km reach [29]) for remote or rural mobile access; transmission of the 5G NR standard at 3.5 GHz toward macrocells (radius >1 km [147]) for enabling eMBB; transmission of an extended-bandwidth 26-GHz digital modulated signal toward indoor femtocells (radius < 50 m [147]) with multi-Gbit/s

throughput. The second wavelength ( $\lambda_2$ ) in Figure 5.1 concerns the existing FTTH application, whereas M2M can be exploited at  $\lambda_3$  for industrial automation purposes according to PROFINET [148], which is the leading Industrial Ethernet Standard in the market. This vertical might be applied to connect industrial clusters and programmable logic controllers (PLCs) in a M2M environment, enabling remote sensing and/or RRH monitoring [148, 149]. It is worth mentioning that two extra wavelengths are allocated for the FTTH and M2M uplink communication.

The contributions over the state of the art are the following ones: (a) the implementation of a multi-band Gbit/s FiWi system using the 5G NR standard in microwave and mm-waves; (b) the demonstration of 5G, FTTx and M2M applications running over the same architecture; (c) the Intel's 5G transceiver use to provide OFDM, GFDM and F-OFDM signals in a flexible way; (d) using digital pre-distortion in the 26 GHz band and analyzing the system performance as a function of the 3GPP  $EVM_{RMS}$  requirements for 5G NR.

The current Chapter is structured in two sections. Section 5.1 describes in details the proposed 5G fiber-wireless system, as well as the experimental setup. Section 5.2 reports the experimental results for distinct application cases, namely: 5G flexible waveform at 788 MHz for long-reach; 5G NR at 3.5 GHz for outdoor eMBB; 26-GHz femtocell for indoor eMBB; M2M application.

## 5.1. The proposed architecture

The operational principle of the proposed fiber-wireless system relies on applying analog radio over fiber technology and WDM overlay for assisting 5G communications. Basically, the approach concentrates the main pieces of hardware at the BBU pool and jointly transports all RF signals up to densely distributed and simplified RRHs, using a DD-MZM and exploiting the existing passive optical network capillarity. Figure 5.2 depicts a block diagram of the implemented FiWi system. The topology is a progress over that from Figure 4.2, since takes into account three 5G predicted bands (700 MHz, 3.5 GHz and 26 GHz) and wireless transmission after the fiber-optic link. Other improvements are using a PON from a local Internet service provider as transport network and adding the PROFINET-based machine-to-machine application.

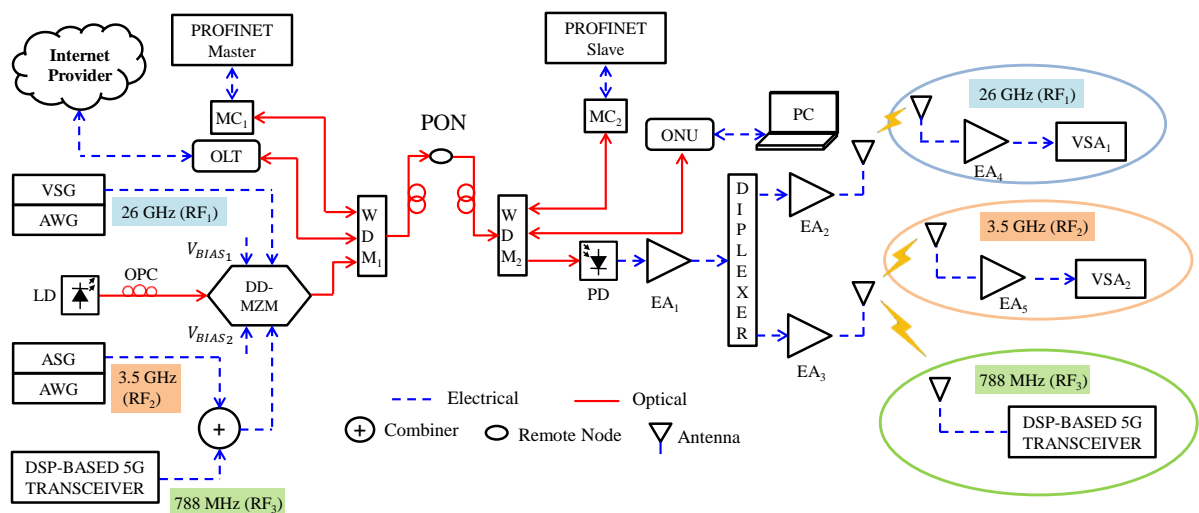


Figure 5.2 – Multi-band FiWi 5G architecture based on RoF and WDM-overlay: OLT - optical line terminal; VSG - vector signal generator; ASG - analog signal generator; MC - media converter; DD-MZM - dual-drive Mach-Zehnder modulator; OPC - optical polarization controller; ONU - optical network unit; EA - electrical amplifier; VSA - vector signal analyzer; PC - personal computer.

The baseband Internet service running at 1490 nm (downlink) and 1310 nm (uplink) is provided by a local Internet service provider called Vivavox (<http://www.vivavox.com.br>), using its PON components, OLT and ONU. Moreover, a baseband M2M application running at 1550 nm is proposed for industrial automation using a PROFINET pair (master and slave) and media converters. Due to the fact our media converters employ also the 1310 nm wavelength, M2M communication and Internet distribution are not simultaneously turned on in the experimental setup, which is ready to support these applications in separated wavelengths.

An AWG combined with a VSG provides a 64-QAM wideband signal at 26 GHz, giving rise to the first RF-driven signal ( $RF_1$ ). This one will be later replaced by a standardized 5G NR signal at the same frequency. The second RF-driven signal ( $RF_2$ ), corresponding to the 5G NR standard at 3.5 GHz, is set up using an AWG with an analog signal generator (ASG). In addition, the DSP-based 5G transceiver generates the third RF-driven signal ( $RF_3$ ), corresponding to the flexible waveform (OFDM, GFDM or F-OFDM) at 788 MHz with 64 and 256-QAM frames. In the current architecture, vector signal generation includes arbitrary waveform generation assisted by digital pre-distortion, upconversion and amplification stages. Both  $RF_2$  and  $RF_3$  are added through a RF combiner and then modulated jointly with  $RF_1$  by using a single DD-MZM, which is fed by a 1560 nm optical carrier and biased close to the quadrature point, by applying  $V_{bias1} = 6.1$  V and  $V_{bias2} = 1.0$  V.

The distinct wavelengths are combined using the WDM coupler and launched to the SMF-based fiber-optic infrastructure from Vivavox, in the city of Santa Rita do Sapucaí-MG, Brazil. The optical signals are launched back at Inatel's laboratory, by implementing a loop at a network node located 1 km away. At the link end, a second WDM coupler separates the optical carriers into different fibers. The 1550 nm signal goes to MC<sub>2</sub>, which feeds the PROFINET slave. The 1490 nm optical carrier is received by an ONU and delivered to a personal computer, whereas the 1560 nm signal goes to the remote radio unit. The uplink signals from the machine-to-machine and Internet applications are individually launched into the system at 1310 nm by means of the second WDM coupler.

Finally, the optical carrier at 1560 nm from the second WDM coupler output reaches the XPDV2150RA photodetector. The three recovered RF signals pass through the first electrical amplification stage, which is a broadband electrical amplifier (EA<sub>1</sub>). A diplexer separates the RF signals as follows: one output delivers RF<sub>1</sub> and another one jointly provides RF<sub>2</sub> and RF<sub>3</sub>. All RF signals are further amplified by a second electrical amplification stage (EA<sub>2</sub> and EA<sub>3</sub>) to be radiated by appropriated antennas. The 26-GHz signal is transmitted and received by 25 and 12 dBi-gain horn antennas, respectively. Next, it is amplified by the fourth amplification stage (EA<sub>4</sub>) and then evaluated by the VSA<sub>1</sub>. In parallel, RF<sub>2</sub> and RF<sub>3</sub> signals are transmitted by the commercial antenna (AARONIA HyperLOG 7040, with 5-dBi gain at both 788 MHz and 3.5 GHz frequencies) and separately received by identical antennas. The 5G NR signal at 3.5 GHz goes through the fifth amplification stage (EA<sub>5</sub>) and is evaluated by the VSA<sub>2</sub>, whereas the 788-MHz signal is analyzed by the 5G receiver block. It is worth mentioning the possibility of improving the system performance by separating the higher and lower frequencies before the EA<sub>1</sub> for reducing the total noise figure, since broadband electrical amplifiers typically present high noise level. This strategy was not adopted in the current work due to the hardware limitations in our laboratory.

The optical ring from Vivavox Internet service provider was 2 km long, i.e., 1 km from the laboratory to the network node followed by 1 km from the network node to the laboratory. In this way, we experimentally evaluated the integration of the 5G FiWi system in a commercial PON, under real channel conditions of temperature, humidity and pressure. Figures 5.3 and 5.4 display photographs of the FiWi system implementation for indoor and outdoor environments, respectively. The main optical and electrical power levels in the experimental setup are reported in Table 5.1.

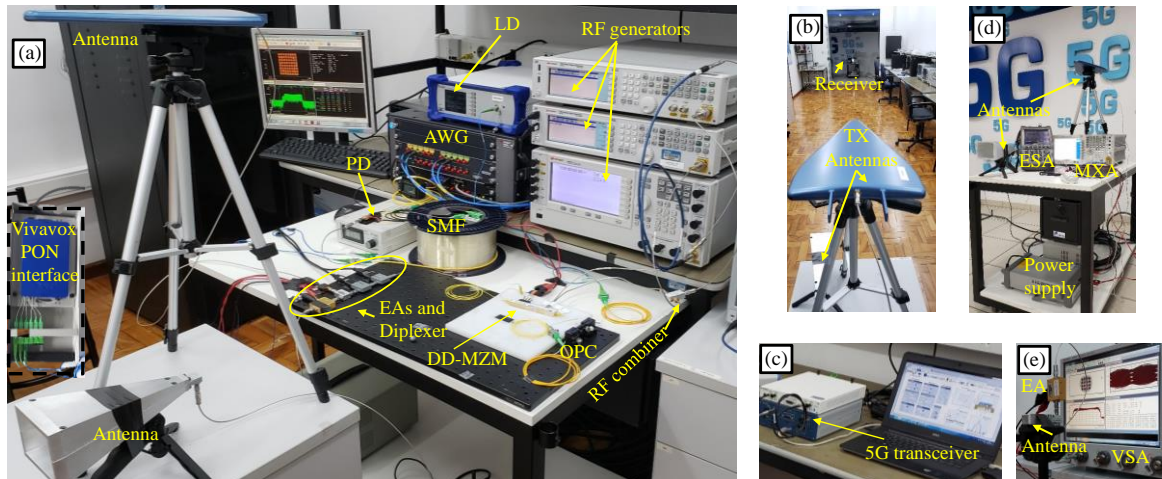


Figure 5.3 – Photographs of the FiWi system implementation in indoor environment: (a) The experimental setup; (b) A wireless link view; (c) The 5G transceiver; (d) The receiver side; (e) Zoom-in-view of the receiver side.

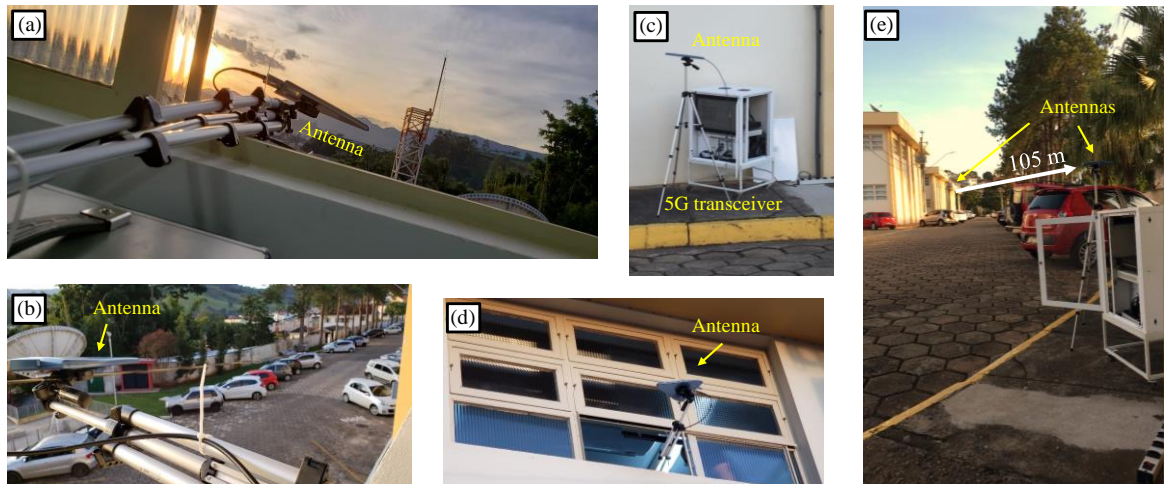


Figure 5.4 – Photographs of the FiWi system implementation in outdoor environment: (a) and (d) The transmitting antenna; (b) The wireless link view from RRU; (c) The 5G transceiver; (e) The wireless link view from the receiver side.

Table 5.1 – Optical and electrical power levels.

Setup stage	Power (dBm)
Laser output	14
DD-MZM output	5.76
DSP-based 5G transceiver output	-5
VSG output	2
ASG output	0
WDM <sub>1</sub> output	4.5
PD input power	-0.5
Radiated power at 788 MHz	2
Radiated power at 3.5 GHz	0.78
Radiated power at 26 GHz	23
Received channel power at 788 MHz (105 m away)	-63
Received channel power at 3.5 GHz (13 m away)	-21
Received channel power at 26 GHz (10 m away)	-13

## 5.2. Experimental results

Three different configurations have been analyzed for evaluating the proposed DSP-based 5G FiWi system architecture, namely: B2B; RoF; FiWi. The first one considers an all-electrical setup, in which the transmitters are directly connected to the receivers using electrical cables. RoF includes the transport of three RF signals through the optical links and electrical amplification stages after the photodetection. FiWi adds wireless transmissions to the RoF configuration. Each usage case has been evaluated according to particular parameters, such as MER, EVM, and throughput.

The electrical spectrum at the photodetector output is presented in Figure 5.5. One can note the presence of the three RF signals at 788.0 MHz, 3.5 GHz and 26.0 GHz. The magnitude difference among them comes either from the electro-optical response of DD-MZM and PD and their bandwidth, i.e. 6, 100 and 200 MHz, as indicated in the zoom-in-views. In a first look, the 26 GHz spectral component seems to be closely to the noise level. However, this is just a consequence of the span (26.5 GHz) set on the electrical spectrum analyzer for viewing RF<sub>1</sub>, RF<sub>2</sub> and RF<sub>3</sub> simultaneously. The zoom-in-view at 26 GHz proves that such spectral component refers to RF<sub>3</sub> with 200 MHz bandwidth. In conclusion, the obtained spectrum is as expected for biasing MZM at the quadrature point since there are no undesired spectral components and no apparent distortion after the simultaneous modulation in the optical domain. From this stage, the RF signals can be properly amplified and radiated, as a function of the desired application.

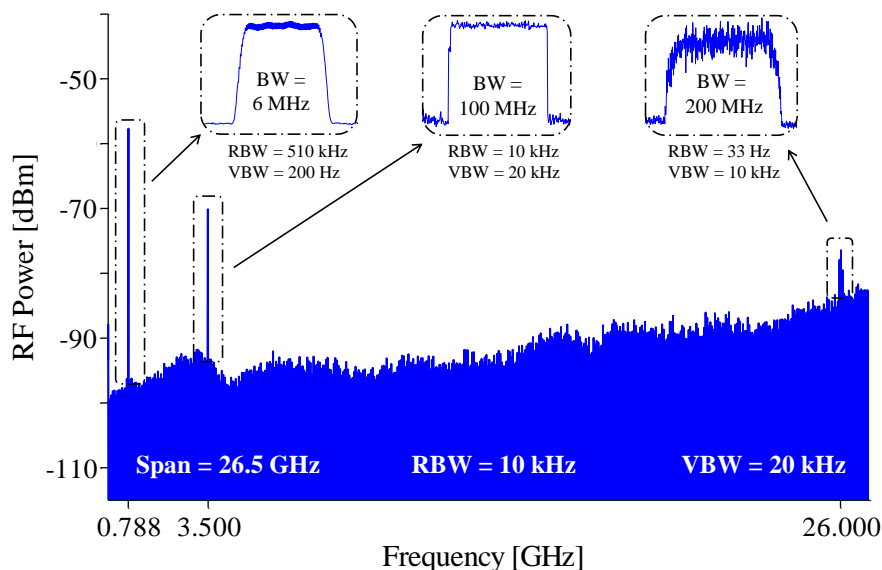


Figure 5.5 – Measured electrical spectrum at the PD output for  $\lambda_1$ .

### 5.2.1. 5G flexible waveform at 788 MHz: Long-reach

Figure 5.6 reports the electrical spectrum of our DSP-based transceiver operating in the single-input single-output (SISO) mode, after the photodetection process as a function of waveform. As expected, GFDM and F-ODFM have presented lower out-of-band emission in comparison with OFDM, which reinforces the advantage of using these innovative waveforms for favoring the coexistence with the 3GPP legacy systems. Despite the similar behavior, F-OFDM has provided OOB emission slightly lower than GFDM for the current channel power condition, as shown in the zoom-in-view.

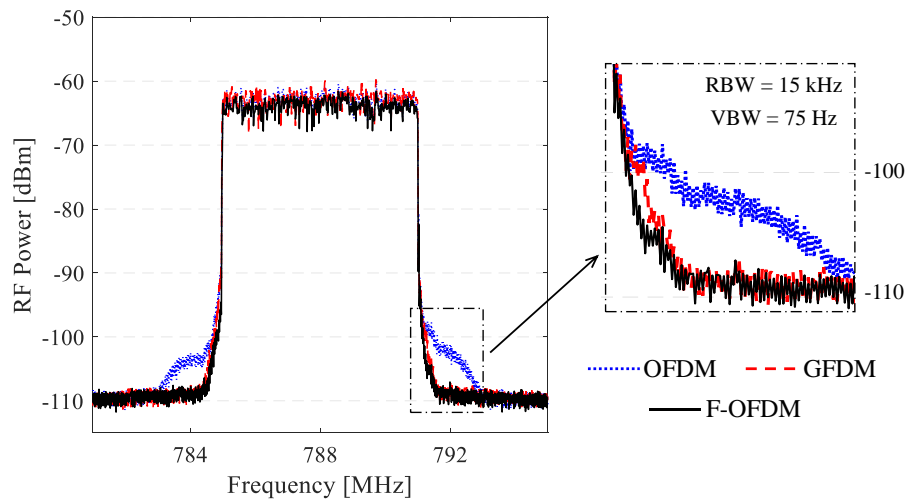


Figure 5.6 – OFDM, GFDM and F-OFDM electrical spectra before radiation.

A digital performance analysis as a function of the selected waveform for B2B, RoF and FiWi configurations is presented in Figure 5.7. As stated earlier, MER is the figure of merit used by the DSP-based 5G transceiver. B2B analysis demonstrates its current version is able to provide MER closely to 36 dB, regardless of the employed waveform. The RoF system including electrical amplification does not significantly modify this behavior, since MER remained above 35 dB for OFDM, GFDM and F-OFDM. In the FiWi system, MER decreased to 30.9 dB for 256-QAM F-OFDM due to the wireless propagation. Nevertheless, F-OFDM has ensured 29 Mbit/s throughput for a 105-m wireless link. By switching to 64-QAM toward robustness, MER increases to 34.4 dB at cost of 5-Mbit/s throughput reduction. The received 256 and 64-QAM F-OFDM constellations are presented in Figure 5.8. The coexistence with the 3.5 and 26 GHz signals has not affected the discussed results.

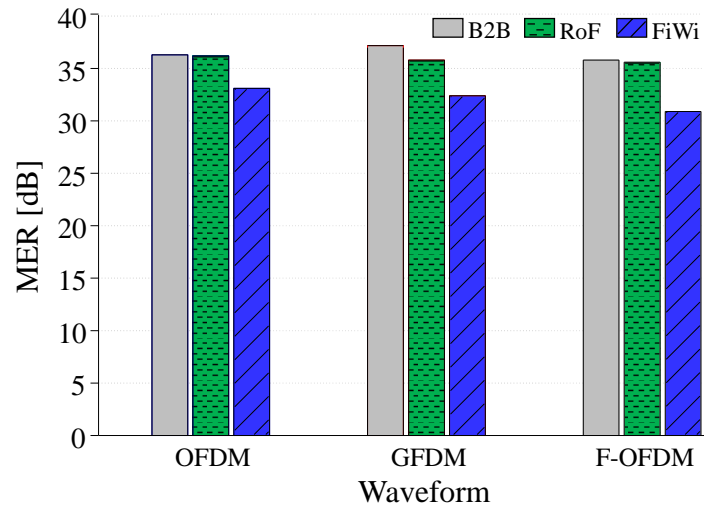


Figure 5.7 – MER analyses for the OFDM, GFDM and F-OFDM waveforms.

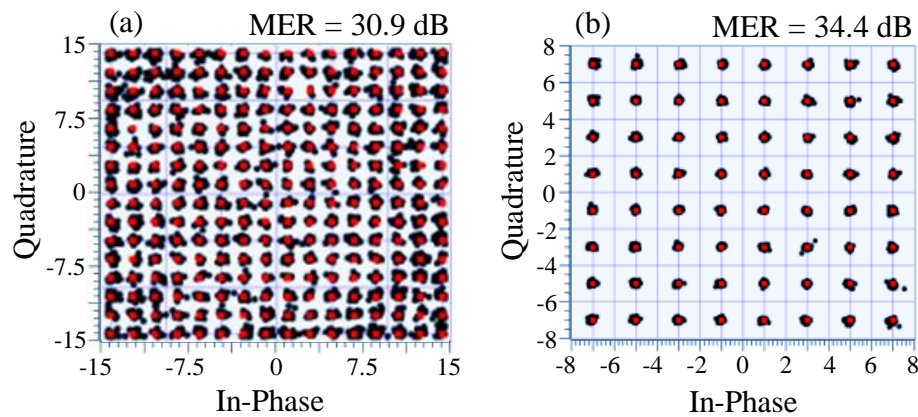


Figure 5.8 – Received 256- and 64-QAM F-OFDM constellations.

### 5.2.2. 5G NR at 3.5 GHz: Outdoor eMBB

The Signal Studio software from Keysight has been used to generate the standardized 5G NR signal, according to 3GPP Release 15 [90]. The resource block (RB) scheme has been configured according to the New Radio test model presented in [150], as illustrated in Figure 5.9. A 10-ms frame is subdivided into 20 time slots. Each time slot consists of a logical downlink or uplink shared channel (DL-SCH and UL-SCH). The conformance test is TDD (time division duplex)-based, hence 16 slots have been allocated to DL-SCH and 4 slots to UL-SCH. Among the 16 DL-SCHs, 14 have been configured to transport 64-QAM symbols and 2 to transport 256-QAM symbols. At each shared channel, a group of demodulation reference signal (DMRS) has also been implemented. In the frequency domain, each time slot is composed of 12 subcarriers.

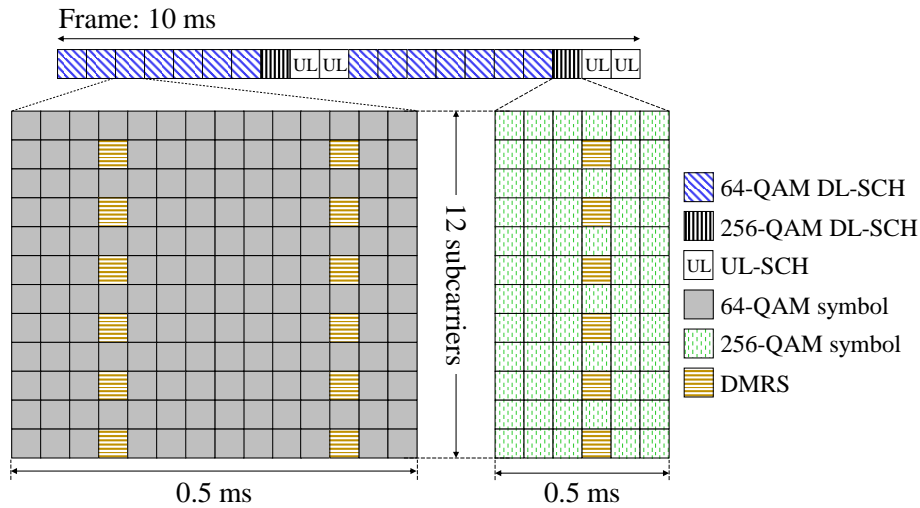


Figure 5.9 – The 5G NR resource block scheme.

The system downlink performance has been evaluated using three distinct bandwidths. The number of allocated resource blocks ( $N_{RB}$ ) is bandwidth dependent, i.e. 51, 162 and 273 for 20, 60 and 100 MHz bandwidth, respectively. Based on the resource block scheme, the 5G NR downlink effective throughput ( $R_b$ ) can be expressed as:

$$R_b = \frac{(a \times K - N_{64DMRS}) \times Q_{64QAM} \times N_{64SCH} \times N_{RB}}{T_{frame}} + \frac{(b \times K - N_{256DMRS}) \times Q_{256QAM} \times N_{256SCH} \times N_{RB}}{T_{frame}} \quad (5.1)$$

in view of 64- and 256-QAM symbols. The coding rate and overhead due to signaling information were not considered. Table 5.2 presents the variables used for the 5G NR throughput calculations: 72.22 Mbit/s for 20 MHz bandwidth; 229.39 Mbit/s for 60 MHz bandwidth; and 386.57 Mbit/s for 100 MHz bandwidth.

Table 5.2 – Variables for throughput calculation.

Variable	Quantity	Value
$a$	Number of 64-QAM symbols per subcarrier	14
$b$	Number of 256-QAM symbols per subcarrier	6
$K$	Number of subcarriers	12
$N_{64DMRS}$	Number of 64-QAM DMRS symbols per RB	12
$N_{256DMRS}$	Number of 256-QAM DMRS symbols per RB	6
$Q_{64QAM}$	Number of bits per 64-QAM symbol	6
$Q_{256QAM}$	Number of bits per 256-QAM symbol	8
$N_{64SCH}$	Number of 64-QAM DL-SCH channels	14
$N_{256SCH}$	Number of 256-QAM DL-SCH channels	2
$N_{RB}$	Number of allocated RB	51, 162, 273
$T_{frame}$	Frame periodicity	10 ms

Figure 5.10 presents the measured EVM results as a function of bandwidth for 13 m wireless link, which has not been extended due to operational issues as the laboratory layout. It is important to highlight 3GPP  $EVM_{RMS}$  requirements for 5G are 8% and 3.5% for 64- and 256-QAM, respectively [91]. For 64-QAM, one can observe an attractive RoF and FiWi digital performance, meeting the 3GPP  $EVM_{RMS}$  requirements with margins of at least 5.8% (8%-2.2%) and 4.1% (8%-3.9%) respectively. These margins could be properly exploited to extend the wireless and/or optical links, as well as to the robustness purpose. A similar conclusion might be raised for 256-QAM in RoF configurations for all considered bandwidths. On the other hand, the EVM performance for the FiWi with 60 and 100 MHz bandwidth has exceeded 3GPP requirements by 0.7% and 0.2%, respectively. Increasing the RF transmitted power and/or using pre-distortion equalization techniques are potential strategies to be further evaluated for overcoming this performance reduction.

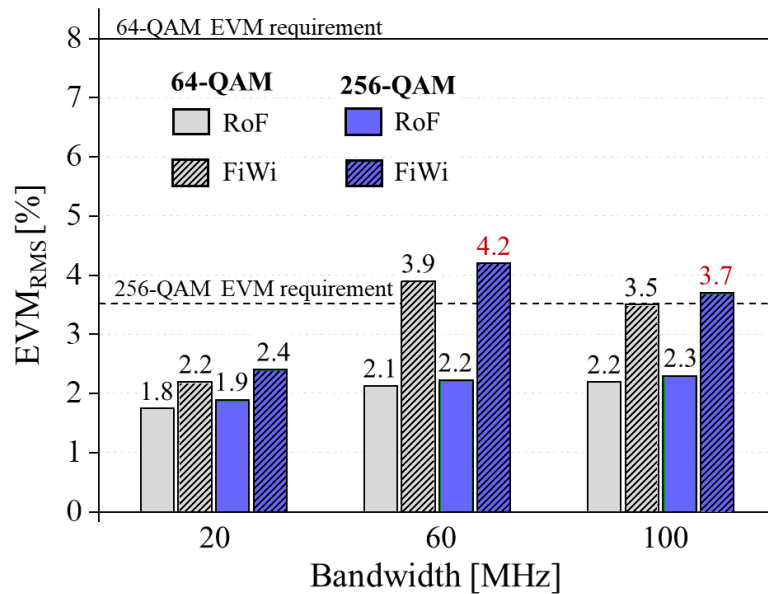


Figure 5.10 – 5G NR performance at 3.5 GHz, as a function of bandwidth.

Figure 5.11 reports the received 5G NR spectra and their respective constellations. It is possible to identify the symbols in the constellation from the B2B and RoF configurations. The dark orange constellation is the 256-QAM, whereas the light orange is the 64-QAM. On the other side, Figure 5.11(c) presents the performance evaluation for FiWi, in which performance degradation in magnitude and phase is observed in both spectrum and constellation. The received RF power was -3.8, -5.3 and -21 dBm for B2B, RoF and FiWi, respectively. The presence of multiple signals in the same system did not impose any performance degradation.

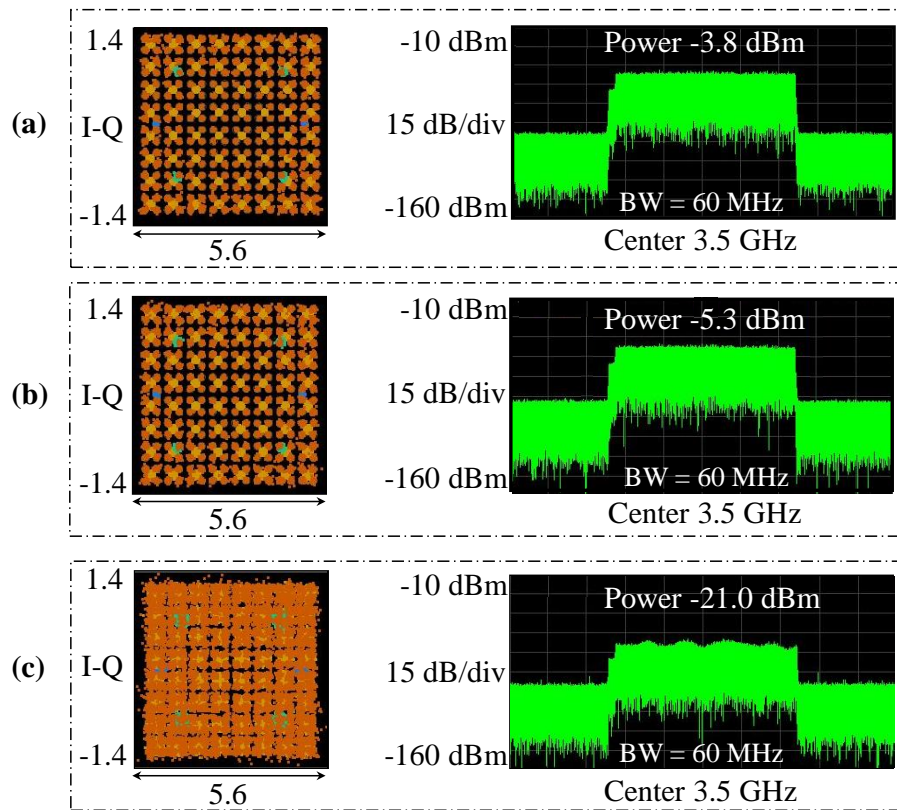


Figure 5.11 – The 5G NR spectra and constellations for 60 MHz bandwidth: (a) B2B; (b) RoF; (c) FiWi.

### 5.2.3. 26-GHz femtocell: Indoor eMBB

The investigation of the indoor enhanced mobile broadband scenario has been conducted at 26 GHz up to 10 m range, considering the following configurations: 16 and 64-QAM modulation formats; 200, 400 and 800 MHz bandwidth; DPD usage. Figure 5.12 reports the  $EVM_{RMS}$  for FiWi at the femtocell edge, as a function of configuration and compared to the 3GPP requirements [91]. Using 200 MHz bandwidth enabled throughput of 600 Mbit/s and 1.0 Gbit/s for 16 and 64-QAM, respectively. Particularly for FiWi without DPD,  $EVM_{RMS}$  surpassed the 3GPP requirements of 12.5% and 8.0% for 400 and 800 MHz bandwidth. On the other hand, by applying DPD, the digital performance has increased significantly and  $EVM_{RMS}$  efficiently met the 3GPP requirements for all evaluated cases. For instance,  $EVM_{RMS}$  in FiWi was reduced from 12.8 to 3.3% when transmitting 16-QAM with  $BW = 400$  MHz. DPD has also made possible  $EVM_{RMS}$  and bitrate of 3.0% and 2 Gbit/s, respectively, for 64-QAM. Additionally, 2.6 Gbit/s throughput and  $EVM_{RMS}$  of 4.2% were achieved for 16-QAM with  $BW = 800$  MHz. Finally, the DPD use has enabled 4 Gbit/s throughput and 3.9%  $EVM_{RMS}$  for transmitting 64-QAM with  $BW = 800$  MHz.

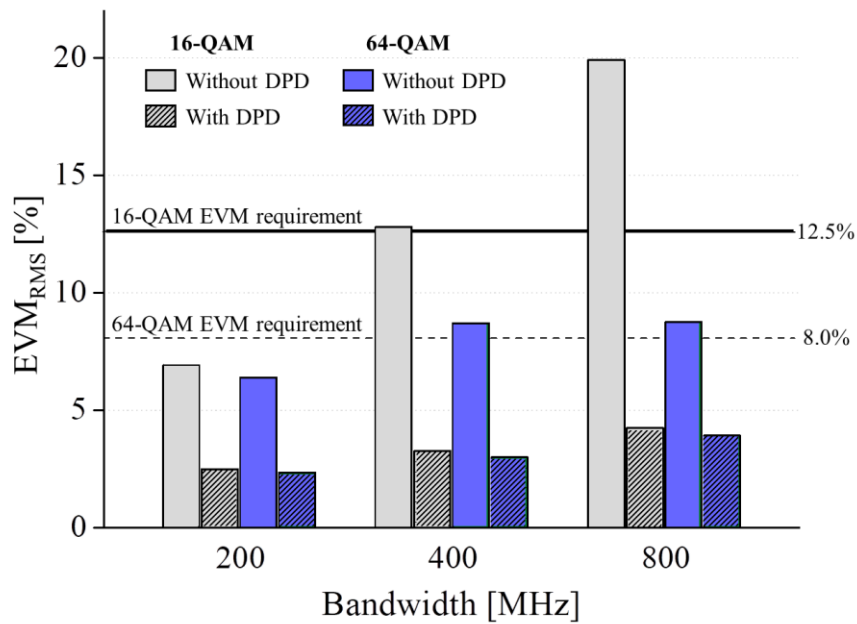


Figure 5.12 – EVM as a function of bandwidth, modulation and DPD usage.

Figure 5.13 reports the measured performance metrics at 26 GHz with 64-QAM and 800 MHz bandwidth, concerning a 4 Gbit/s throughput. This achievement is four times higher than our previous result from subsection 4.2.2. The 64-QAM constellation and eye diagram are appropriate for eMBB applications with SNR  $\approx$  25 dB and EVM<sub>RMS</sub> of 3.9%. The presented results did not suffer modification when turning the other RF signals off, which reinforce the possibility of coexistence.

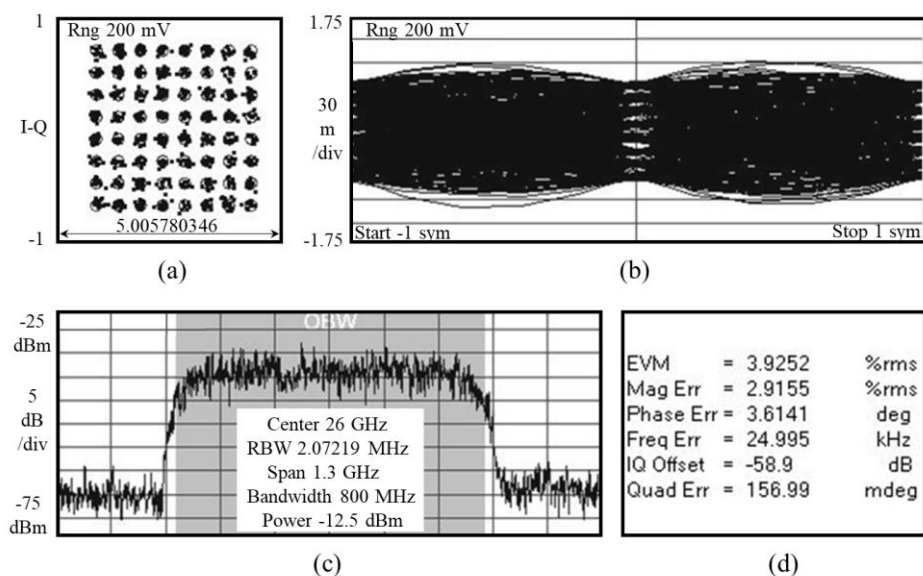


Figure 5.13 – Performance analysis of the 4 Gbit/s signal at 26 GHz for 10 m range:  
 (a) Constellation; (b) Eye diagram; (c) Electrical spectrum; (d) EVM<sub>RMS</sub>.

We have also investigated the indoor eMBB scenario using the 5G NR signal at 26 GHz. This signal has been generated by using the Signal Studio software from Keysight, instead of an arbitrary waveform generator as in the previous case. The 5G NR frame has been set with 10 ms and split into 80 time slots. All of them have been allocated with downlink shared channel; 49 slots have been configured to transport 64-QAM symbols and 31 slots to transport 16-QAM symbols, aiming to address multiple services. Each time slot carries 14 symbols, and 18 and 12 DMRS symbols per resource block have been considered for the 64 and 16-QAM, respectively. 5G NR signals with 26 and 60 resource blocks have been considered for evaluating the RoF and FiWi digital performance with 50 and 100 MHz bandwidth, respectively. By applying Equation (5.1), we have calculated the system throughput, reaching 164.95 and 380.65 Mbit/s for 50 and 100 MHz bandwidths, respectively.

Figure 5.14 presents the  $EVM_{RMS}$  performance analysis as a function of bandwidth for both RoF and FiWi scenarios; the latter one with a 10-m wireless link as a proof-of-concept. One can observe  $EVM_{RMS}$  kept lower than 5%, efficiently meeting the 3GPP requirements in all analyzed configurations. The margins for  $EVM_{RMS}$  degradation were at least 8.3% and 3.6% for 16- and 64-QAM, respectively. Once again, these margins could be properly used to extend the wireless and/or optical links, as well as to the robustness purpose. Figure 5.15 reports the received constellation diagram for the 5G NR signal with 100 MHz bandwidth. The constellation simultaneously presents well-defined 16 and 64-QAM symbols from the DL-SCH data, represented by dark and light orange circles, respectively. The other symbols observed in Figure 5.15 are from the demodulation reference signal and synchronism.

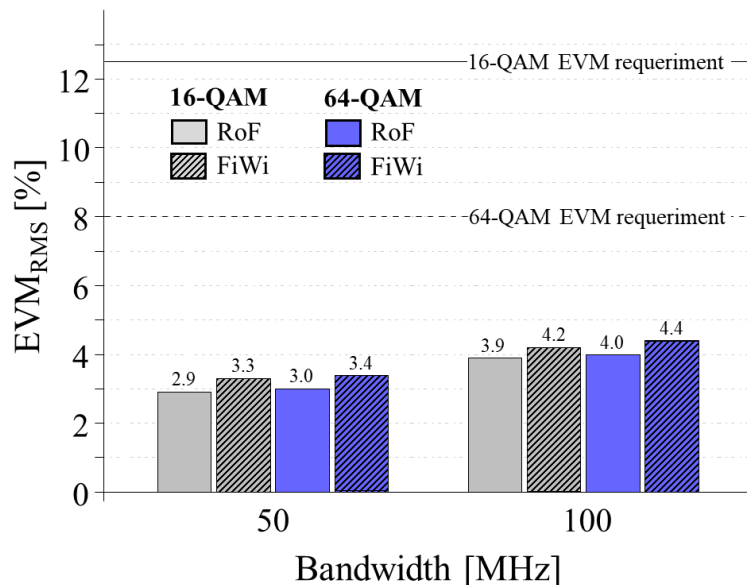


Figure 5.14 – 5G NR performance at 26 GHz as a function of bandwidth.

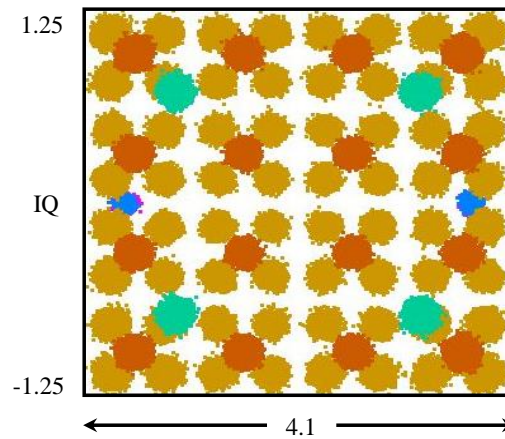


Figure 5.15 – The received 5G NR constellations from the FiWi system for 100 MHz bandwidth.

#### 5.2.4. M2M application

The M2M applicability of the proposed multi-band FiWi system has been implemented using PROFINET standard. A programmable logic controller and an input/output module have acted as the network master and slave, respectively, through 2 km optical link. The E/O and O/E conversions have been assured by using bidirectional media converters. The performance metric was the network latency, which has been measured using a digital oscilloscope. To do this, we have measured the delay between a digital input signal and a digital output signal. Figure 5.16 presents the M2M experimental setup photography, whereas Figures 5.17(a) and 5.17(b) report the delay measurements in the back-to-back and optical link configurations, respectively.

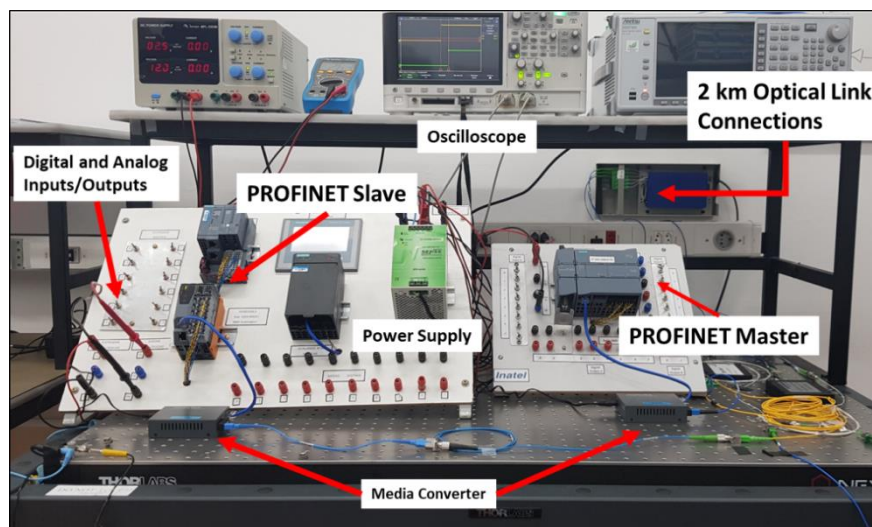


Figure 5.16 – The experimental setup for the M2M application.

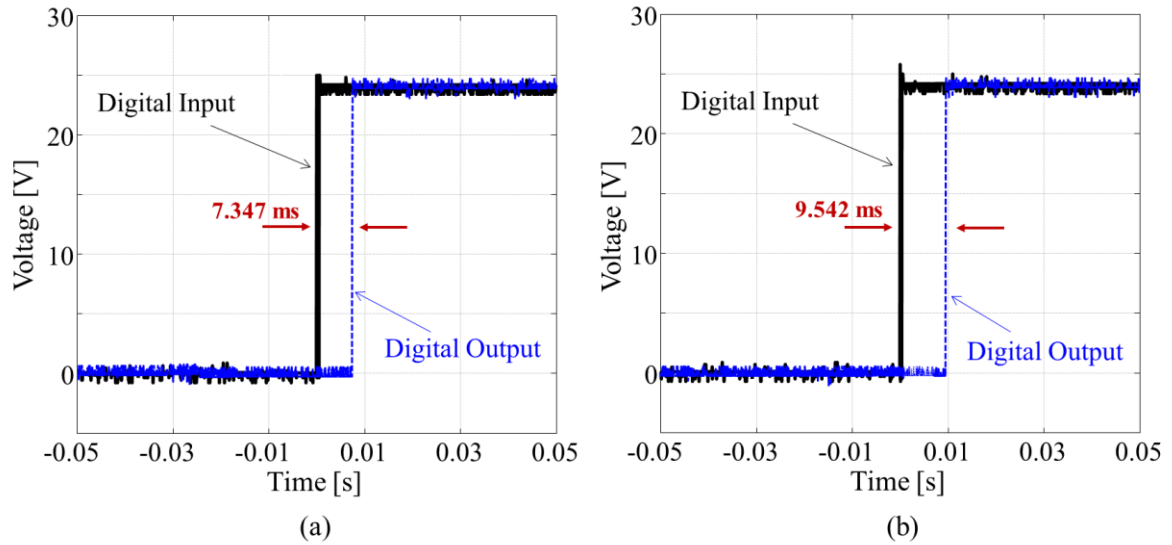


Figure 5.17 – M2M application: (a) B2B latency measurement; (b) optical link latency measurement.

The total measured delay was 7.347 ms for B2B and 9.542 ms for the optical link case. It is worth mentioning the digital signal needs to be sent from slave to master, be processed at 300  $\mu$ s cycle time and sent back to the slave in sequence. Therefore, the delay imposed by the system corresponds to the transmission from slave to master and back, from the master to slave, representing 4 km propagation into the optical fiber. As a consequence, the delay between master and slave in a one-way transmission is approximately 4.771 ms (9.542 ms/2). In any case, the time delay might be considered satisfactory, because the PROFINET latency requirement should not exceed 10 ms for real-time applications [149,151]. Therefore, our approach might be considered promising for replacing wired-based Ethernet links, which are limited to 100 m. As a conclusion, the discussed application stack known as a vertical in the Industry 4.0 literature, represents an attractive solution to ensure low-latency, long-range and electromagnetic immunity for control, automation and industrial environments.

## 6. Implementation 3: Multi-band 5G NR system with photonic-assisted RF amplification (PAA)

Two methods for increasing the RF power level delivered by the RoF link at the remote radio unit are commonly used. The first one concerns to the use of one or more EDFAs to boost the optical power at PD input and, consequently, the RF power reaching the transmitting antennas [152]. Meanwhile, high optical peak power could saturate and even damage the photodetector since this device typically tolerates a maximum optical power of 2 dBm. Even using high-power ( $\approx 10$  dBm) photodetectors, which are expensive (e.g. \$3,819.24 for DX30AF from Thorlabs), the RF power increment is still limited by the PD absolute maximum ratings. The second strategy makes use of electronic-based RF amplifiers after photodetection. However, these amplifiers are typically expensive (e.g. \$5,300.13 for SBUA-400-12-010-K from Fairview Microwave) and impose noise figure higher than 4 dB for mm-waves, in particular if broadband operation is desired [153]. Moreover, cascading electrical amplifiers at the remote radio unit brings complexity to the remote site.

As an alternative to the discussed methods, RoF systems can take advantages of photonics technology and nonlinear optics for enabling RF signal amplification in the optical domain, i.e. increasing the photodetected electrical power without requiring electrical amplifiers or high-power photodetectors [154-159]. The nonlinear four-wave-mixing (FWM) effect, although commonly unwanted in optical communications, has been demonstrated as useful for such application.

In [154], Wall and Foster introduced the concept of microwave amplification for analog fiber optic links using FWM, and demonstrated 9 dB photonics-assisted RF gain for frequencies up to 14 GHz. Afterward, we have described in detail and experimentally evaluated their innovative technique as a function of diverse optical and electrical parameters aiming to further enhance the RF gain [155]. Moreover, we have significantly optimized the setup and applied a special highly nonlinear fiber (HNLF) for developing an ultra-wideband photonics-based RF amplifier (PBRA), as a building block of a photonics-based RF front-end for 5G networks [156]. Its experimental analysis has demonstrated RF gain of 16 dB up to 38 GHz using the first FWM product, as well as distortion absence and low phase noise ( $-80$  and  $-90$  dBc/Hz at 1 and 100 kHz frequency offset, respectively). An additional investigation of the PBRA applicability for broadband communications has been reported in [157],

demonstrating 16-dB photonics-based RF gain for the entire bandwidth of a 2 Gsym/s signal at 20 GHz, with clear eye-diagrams and constellations.

Recently, a thermal and dynamic range characterization of the PBRA approach has been reported [158]. The experimental analysis from 300 kHz to 50 GHz took into account different figures of merit, such as RF gain, spurious-free dynamic range and RF output power stability as a function of temperature. The thermal characterization from -10 to +70°C has demonstrated a flat photonics-based RF gain over the entire frequency range under real operational conditions of a base station. Additionally, we have applied the RF amplification method under discussion to implement a 19-dB photonically-amplified FiWi Xhaul [159]. The proposed system allowed either eliminating two 12-dB electrical amplifiers at the remote radio unit without compromising EVM or increasing throughput in 2.4 times, attaining 12 Gbit/s.

This Chapter introduces the concept and reports the implementation of a multi-band 5G NR radio over fiber system with photonic-assisted RF amplification (PAA). Our goal with the latter one is addressing 5G applications at the same time as reducing or even eliminating RF amplification stages at the remote radio unit. The approach is based on analog RoF technology and four-wave-mixing, with the purpose of using fiber-optic links not only for distributing RF signals, but also using them as a multiband amplifying medium for all mobile generations.

The main contributions over the state-of-the-art are the following ones: a novel technique for providing PAA using only one laser and a piece of HNLF, which differs from previous works [154-159] that require an additional pumping laser and a tunable passband filter; a simultaneous distribution of LTE and three 5G signals, including the 5G NR standard at 3.5 GHz, with the benefit of the photonics-assisted broadband RF gain. Moreover, the new PAA approach provides the important advantages of straightforward integration to the transport network and simplicity, when compared with other PAA methods [154-159].

The current Chapter is structured in three sections. Section 6.1 describes the photonic-assisted RF amplification technique previously reported in the literature. Section 6.2 presents the architecture for implementing the multi-band 5G NR system with a new PAA technique. Finally, Section 6.3 reports the experimental results from the proposed topology.

## 6.1. Photonic-assisted RF amplification techniques

The photonic-assisted RF amplification technique has been idealized for fiber-wireless networks based on analog RoF technology, with the aim of providing wideband and flat RF gain regardless of frequency operation. Since the approach has commonly been presented as a black box, it has also been called photonics-based RF amplifier or PBRA [156, 158]. Figure 6.1 describes its schematic, which differs from conventional RoF (CRoF) system mainly due to the use of the following components: an additional laser; an additional polarization controller; an optical coupler; a span of highly nonlinear fiber; an optical tunable passband filter (OTPF) [157, 158].

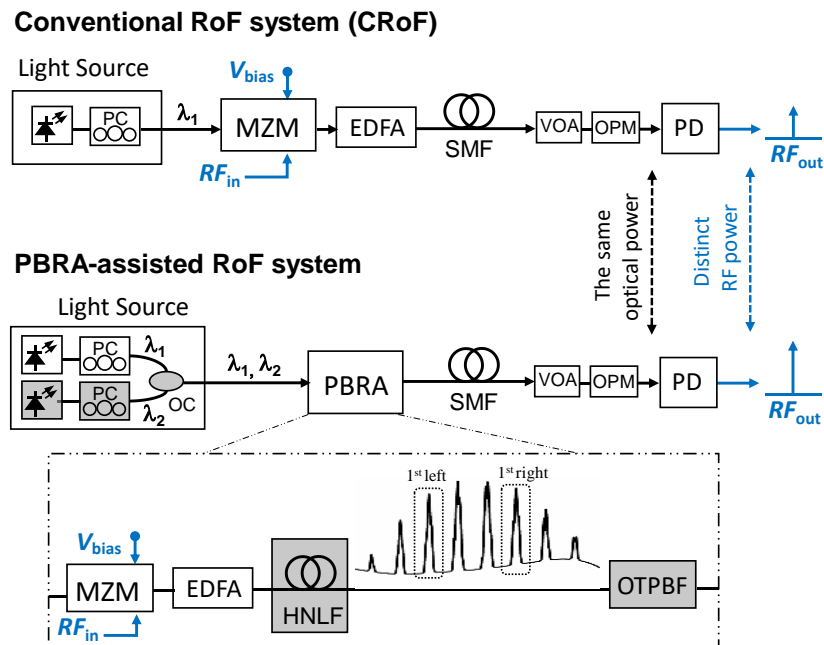


Figure 6.1 – The CRoF and PBRA-assisted RoF architectures. PC: polarization controller; MZM: Mach-Zehnder Modulator; SMF: single mode fiber; HNLF: highly nonlinear fiber; OTPBF: optical tunable passband filter; VOA: variable optical attenuator; OPM: optical power monitor; PD: photodetector.

In the PBRA-assisted RoF system, two non-coherent optical carriers ( $\lambda_1 = 1,555.35$  nm and  $\lambda_2 = 1,558.65$  nm), with 10 MHz linewidth, are co-polarized by using polarization controllers and then coupled by a fiber-optic coupler. A single-drive MZM modulates both continuous waves with the RF-driven signal ( $RF_{in}$ ) and an EDFA ensures 20 dBm optical power at the input of a special HNLF from Sumitomo Electric Industries®. The HNLF main parameters are the following: attenuation  $\alpha = 0.8$  dB/km; fiber length  $L = 470$  m; nonlinear

coefficient  $\gamma = 28 \text{ W}^{-1}\text{km}^{-1}$ ; zero-dispersion wavelength  $\lambda_0 = 1557 \text{ nm}$ ; dispersion slope  $S_0 = 0.023 \text{ ps/nm}^2/\text{km}$ . The modulated electrical field is amplified and launched to the HNLF for enhancing the nonlinear efficiency and generating FWM products. The two modulated optical waves transfer part of their energy to the new spectral components, as reported by the inset from Figure 6.1, which is a measurement of the optical spectrum at the HNLF output.

An OTPBF selects either the first left ( $\lambda_3 = 2\lambda_1 - \lambda_2 = 1552.05 \text{ nm}$ ) or right ( $\lambda_4 = 2\lambda_2 - \lambda_1 = 1561.95 \text{ nm}$ ) FWM product (highlighted in the inset) and launch it to the SMF-based fiber-optic link. A variable optical attenuator and an optical power monitor are in the schematic to precisely control and measure the received optical power, respectively. As a result, the PBRA-assisted RoF system provides photonics-based RF amplification by increasing the RF power level ( $RF_{\text{out}}$ ), when compared to the CRoF at the same photodetected optical power, e.g. 2 dBm [157]. As illustrated in Figure 6.2, the electrical power difference between PBRA and CRoF has been defined as the photonics-based RF gain, which attains about 16 dB and takes place because the total energy contained in the RF sidebands is comparatively higher in FWM products [156, 157]. It is worth mentioning the two optical waves ( $\lambda_1$  and  $\lambda_2$ ) from the light source block should be set close to the HNLF zero-dispersion wavelength and co-polarized, with the aim of enhancing the propagation phase matching and, consequently, maximizing the FWM efficiency [160].

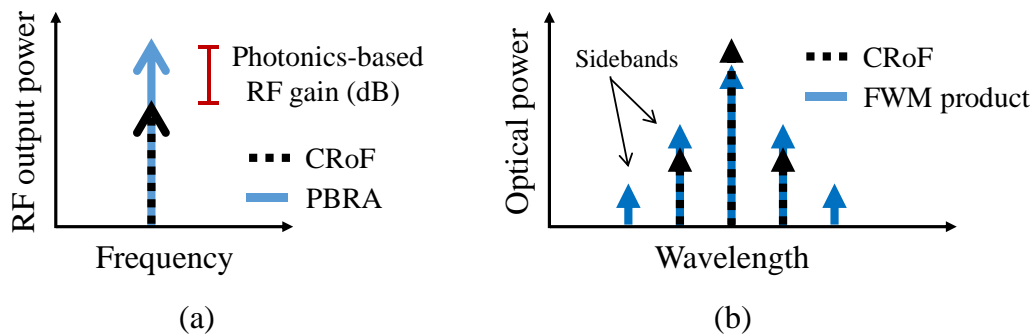


Figure 6.2 – The CRoF and PBRA comparison: (a) electrical spectra at the photodetector output; (b) optical spectra at the photodetector input.

The described approach has been enhanced in terms of performance and capability of being integrated with Xhaul, giving rise to an evolved PAA technique. The latter one is schematized in Figure 6.3 [159]. The principle of operation and physical mechanism behind the photonics-based RF gain has not been changed over the approaches presented in [154-158]. However, one can observe that contrary to the schematic from Figure 6.1, the

optical pump is now coupled to the data signal after the electro-optic modulation process. It brings two main advantages as follows: more efficiency on the pumping process, which becomes free from the MZM insertion loss and not limited by the modulator maximum input power; flexibility to implement PAA outside the central office and on different Xhaul segments, according with the provider demands. A 19-dB RF gain over CRoF has been obtained with such methodology [159]. The discussed architectures, in particular those published in [158] and [159], have been designed as part of the thesis contributions, being the basis for the new PAA approach that is going to be presented in the next section.

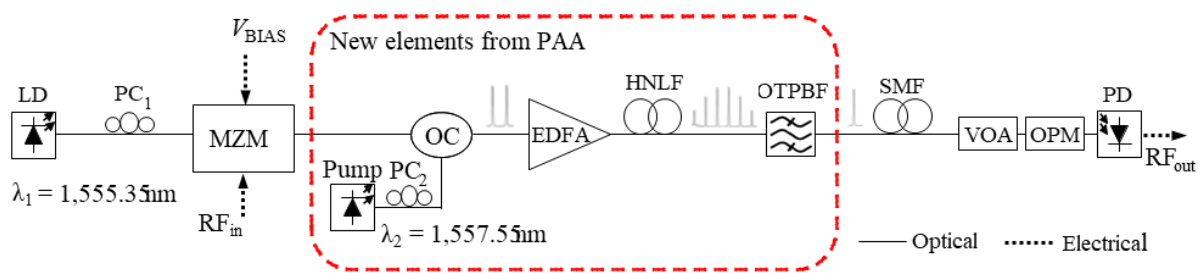


Figure 6.3 – PAA technique employing optical pumping after the electro-optic modulation process.

## 6.2. The proposed multi-band 5G NR system with PAA

Figure 6.4 depicts the block diagram of our multi-band RoF system with photonic-assisted RF amplification. We propose to simultaneously transmit four RF signals, namely: a F-OFDM signal ( $RF_1$ ) generated by the Intel's 5G transceiver at 788 MHz and designed for covering remote areas; an LTE signal at 2.7 GHz ( $RF_2$ ); a 5G NR signal at 3.5 GHz ( $RF_3$ ) in accordance with the 3GPP Release 15 for enhanced mobile broadband applications [90]; a 26 GHz digital modulated signal ( $RF_4$ ), aiming 5G frequency range 2, for gigabits per second indoor communications.

In the current approach,  $RF_1$  and  $RF_2$  feed the first RF input port of DD-MZM after being combined with an RF combiner. In parallel,  $RF_3$  and  $RF_4$  feed the second DD-MZM RF input port after being combined by a diplexer. A laser diode generates a 9 dBm optical carrier at  $\lambda_1 = 1,556.96$  nm, which is modulated by the RF-driven signals using DD-MZM. Both bias voltages ( $V_{bias1}$  and  $V_{bias2}$ ) are properly set between quadrature and null points for optimizing PAA. The modulated electrical field in the optical domain (Figure 6.4(i)) consists of an optical carrier and their sidebands spaced by the RF-driven frequencies, despite only the

26 GHz sidebands being visible due to the MS9740A optical spectrum analyzer 0.07 nm resolution. Up to this setup stage, there are no changes in the multi-band RoF scheme as a function of applying PAA, with the exception of properly adjusting the bias voltages. Such feature is already an important advantage over previous PAA approaches, which use optical pumping in an additional wavelength for favoring the FWM products generation.

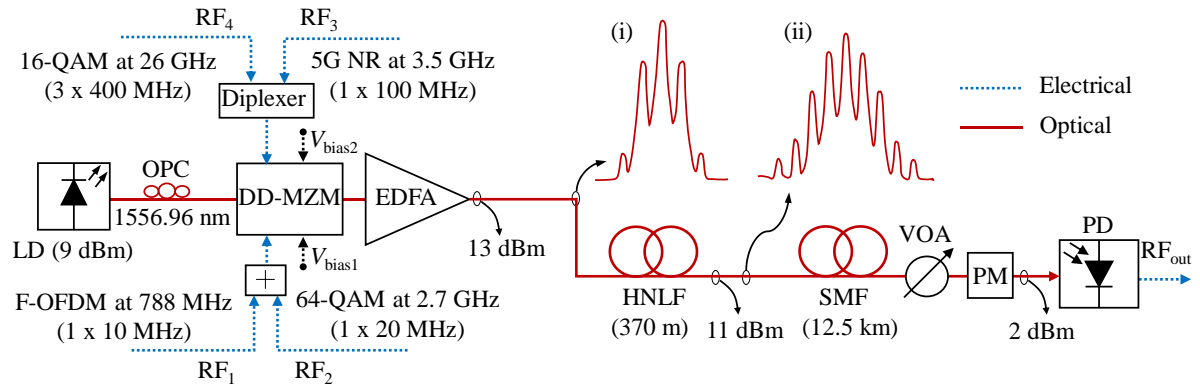


Figure 6.4 – Multi-band RoF system with photonic-assisted RF amplification.

The modulated optical signal is amplified by an EDFA, before being launched into the HNLF for stimulating FWM, which causes a modulation index increase (Figure 6.4(ii)), implying a photonic-assisted RF gain for all RF-driven signals. The EDFA employment aims to increase the total optical power at the HNLF input ( $P_{\text{HNLF}}$ ) and, consequently, enhance the FWM figure-of-merit defined as  $\gamma PL$  [155], in which  $\gamma$  is the fiber nonlinear coefficient and  $L$  is the fiber length. The  $\gamma PL$  product is significantly enhanced by using the Sumitomo HNLF, which provides  $\gamma = 28 \text{ W}^{-1}\text{km}^{-1}$  and  $L = 370 \text{ m}$ . The PAA performance is also affected by the phase matching condition, which is directly associated with the laser wavelength ( $\lambda_1$ ) and fiber zero-dispersion wavelength  $\lambda_0$  [160]. Since our HNLF has  $\lambda_0 = 1,557.00 \text{ nm}$ , the phase matching has been ensured by setting  $\lambda_1 = 1,556.96 \text{ nm}$ .

Finally, the resultant optical signal reaches a PIN photodetector, after being propagated through 12.5 km of single-mode fiber as proof of concept. The absence of optical filter is an additional advantage of the current approach over those from [154-159]. A variable optical attenuator and a power monitor enable the PD input power management. PAA provides then a higher RF power level ( $P_{\text{RFout}}$ ), when compared to a CRoF at the same optical power. As in [154-159], the photonic-assisted RF gain continues to be defined as the RF power level difference between our approach and a CRoF system for the same optical power at PD. It is worth mentioning the PAA gain depends on the FWM nonlinear efficiency and

modulation index, since the resulting higher RF power is due to the beating between the FWM products and sidebands. The current PAA technique might be also understood by the following theoretical analysis, in conjunction with the experimental results reported in the Figure 6.4 insets (i) and (ii).

The optical carrier electrical field might be defined as [161]

$$E_o(t) = E_o \cos(\omega_o t + \varphi_o), \quad (6.1)$$

where  $E_o$ ,  $\omega_o$  and  $\varphi_o$  are the optical carrier amplitude, angular frequency and phase, respectively. Similarly, the electrical field of sideband, which is a result of the modulation, can be expressed by

$$E_j(t) = E_j \cos(\omega_j t + \varphi_j), \quad (6.2)$$

in which  $E_j$ ,  $\omega_j$  and  $\varphi_j$  are the sideband amplitude, angular frequency and phase, respectively, and  $j$  is the sideband order. For instance, inset (ii) from Figure 6.4 reports an optical spectrum with  $j$  equal to  $\pm 4$ ,  $\pm 3$ ,  $\pm 2$ , and  $\pm 1$ . The PD output current is given by

$$I(t) = R|E(t)|^2 = R|E_o(t) + E_j(t)|^2, \quad (6.3)$$

where  $R$  is the PD responsivity. One can note the sidebands number and amplitude affect the PD output current. Assuming  $j = 1$  and PD with limited bandwidth, the current at the PD output can be expressed as [161]

$$I_{RF} = 2R\sqrt{P_0 P_1}[(\omega_o - \omega_1)t + (\varphi_o - \varphi_1)], \quad (6.4)$$

where  $P$  is the optical power level. Equation (6.4) shows that the resultant RF signal depends on the angular frequency and power of optical carrier and sidebands. Therefore, once the sidebands number and power level increment owing FWM, as can be seen by comparing the insets (i) and (ii) from Figure 6.4, photonics-based RF gain is attained.

As was aforementioned, the current PAA technique takes advantage of does not requiring optical pumping, additional wavelength and optical tunable filter. These features favor integrating PAA to the 5G fronthaul in a simple way, i.e. adding a piece of HNLFF to the RoF link. Experimental results of such integration are presented in the next section.

### 6.3. Experimental results

For the experimental investigation, we have properly set the RF-driven signal according to the envisaged application scenario.  $RF_1$  assumed 10-MHz bandwidth and was mapped into 64-QAM, resulting on 40 Mbit/s bit rate. BW of 20 MHz and 64-QAM were assigned to  $RF_2$  toward 120 Mbit/s throughput, whereas  $RF_3$  was mapped from 16- to 256-QAM symbol with 100-MHz bandwidth, enabling data rates from up to 680 Mbit/s.  $RF_4$  assumed 3x400-MHz 16-QAM sub-bands with 40 MHz guard-band for avoiding crosstalk [65], resulting in 4.8 Gbit/s data rate. It is worth highlighting the frequency, bandwidth and resource allocation of each RF-driven signal have been set based on the 4G and 5G standards. Furthermore, the power level of the RF-driven-signals ( $P_{RFin}$ ) has been set to -5 dBm, except for  $RF_4$ , which was +10 dBm to partially compensate the additional power losses from the RF cables (FMC2929085-12) and DD-MZM (Photline MZDD-LN-10) and PD (u2t XPDV2150RA) electro-optic frequency responses at 26 GHz. The optical power at the photodetector has been kept close to +2 dBm.

A vector signal generator from Rohde & Schwarz (Model SMBV100B) has been used to generate the standardized 5G NR signal ( $RF_3$ ), in such way the resource block scheme has been configured according to the NR test model presented in [150]. It has been set as following: 10 ms and 20 time slots subdivided frame; 264 resource blocks; 30 kHz subcarrier spacing.

Figures 6.5(a)–6.5(d) report the measured electrical spectra at PD output for  $RF_1$ ,  $RF_2$ ,  $RF_3$  and  $RF_4$ , respectively, for the multi-band RoF system with and without PAA. The photonic-assisted RF amplification technique provided approximately 15 dB gain for all transmitted RF signals. Neither distortion or significant noise floor increment have not been observed. Particularly for the 26 GHz band (Figure 6.5(d)), one can observe three 400 MHz sub-bands, as well as guard-bands of 40 MHz among them with 30-dB isolation. Besides the RF amplification, one can note a 3-dB maximum amplitude variation for both PAA and CRoF, due to the sub-bands very large bandwidth. In a fiber-wireless system, the four RF signals would be separated by using diplexers to be transmitted over the air.

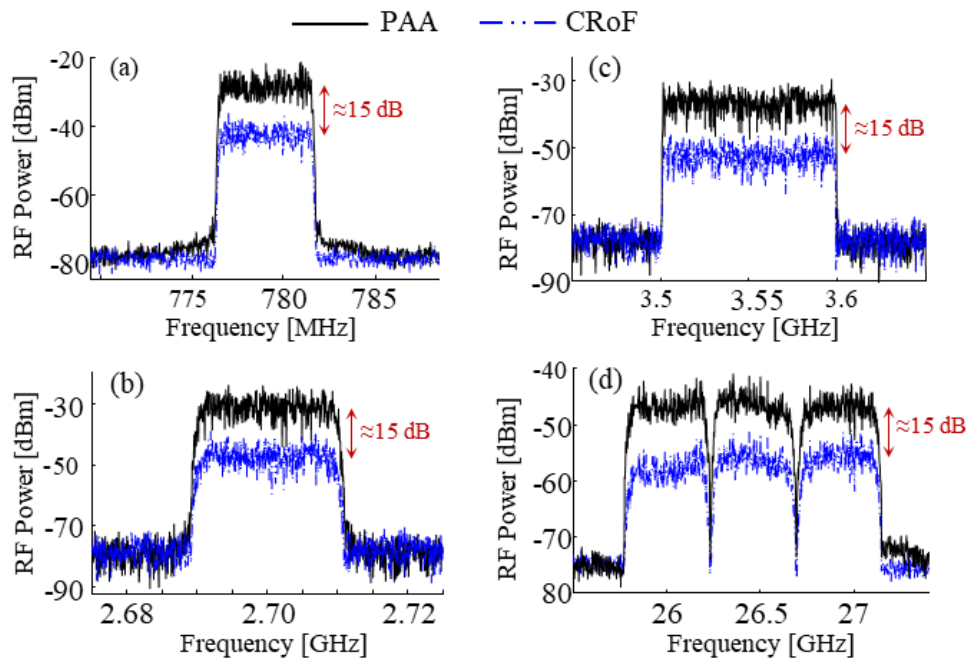


Figure 6.5 – Measured electrical spectra at the PD output: (a) F-OFDM at 788 MHz; (b) LTE at 2.7 GHz; (c) 5G NR at 3.5 GHz; (d) QAM at 26 GHz.

Figure 6.6(a) presents a wideband characterization of PAA, obtained by measuring the transmission coefficient ( $S_{21}$ ) and comparing it to the conventional RoF system. One can note PAA is able to perform uniform photonic-assisted RF gain of approximately 15 dB from 300 kHz to 26 GHz. The power reduction as a function of frequency, observed in both curves, is due to two reasons: the RF cables attenuation; the DD-MZM and PD electro-optic frequency response. In addition, Figure 6.6(b) reports the phase noise from the RF generator and PAA entire setup at 26 GHz, which was measured using the phase noise function from an MXA N9020A signal analyzer from Keysight. The RoF system with PAA presented phase noise levels close to that from the RF generator, e.g. -90 dBc/Hz at 10 kHz offset frequency, which means there are no significant penalty regarding this parameter. The PAA residual phase noise for offset frequencies higher than 200 kHz is still not harmful, since it remained below -100 dBc/Hz.

Figure 6.7 reports a digital performance analysis based on the  $EVM_{RMS}$  parameter of the 26 GHz sub-bands, by comparing the proposed multi-band and photonic-assisted system with CRoF. First, two identical 12-dB gain broadband electrical amplifiers ( $EA_1$  and  $EA_2$ ) from Fairview Microwave (SBUA-400-12-010-K) have been cascaded at the PD output, in such way  $EVM_{RMS}$  was measured after them using a vector signal analyzer (inset (i)).

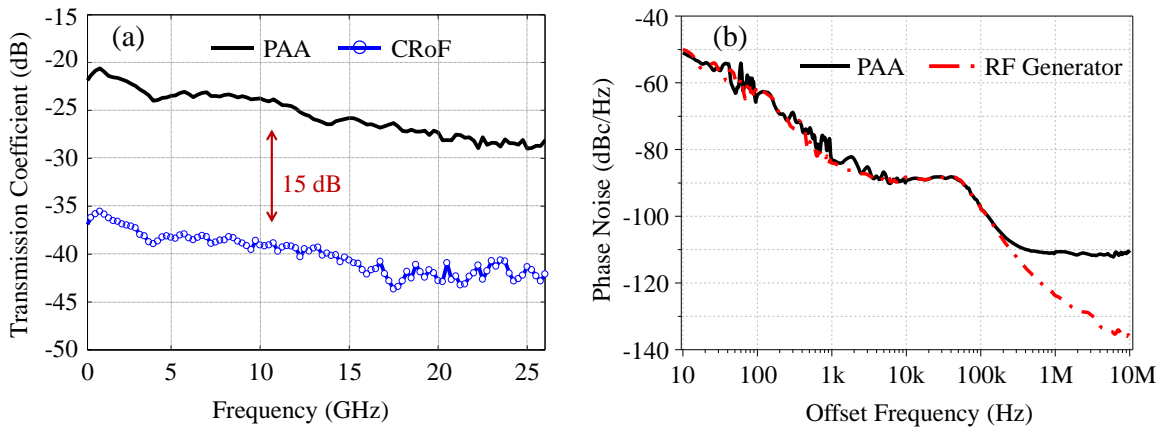


Figure 6.6 – PAA characterization: (a) Flatness as a function of frequency; (b) Phase noise at 26 GHz.

The  $EVM_{RMS}$  of the 26 GHz sub-bands were from 7.9 to 8.5% for the CRoF solution, fulfilling the 3GPP requirements [91], as reported in Figure 6.7. Our multi-band RoF system with 15-dB gain provided enhanced digital performance and suitable constellations due to the remarkable advantage of photonically amplifying the RF signal without adding noise. One can note a significant improvement on the  $EVM_{RMS}$  parameter, implying in 2.5%, 1.8% and 1.6% for the left, central and right sub-bands, respectively. It means the proposed approach can favor to bring robustness or extend the mobile coverage for mm-wave Gbit/s communications in accordance to the 3GPP requirements.

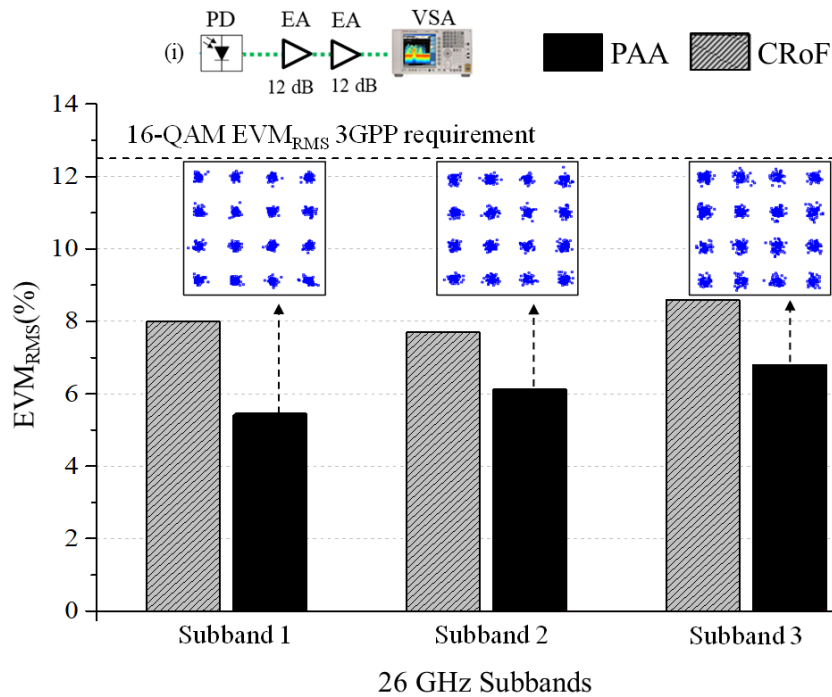


Figure 6.7 – Digital performance analysis of the 26 GHz sub-bands for PAA and CRoF.

In order to evaluate the digital performance of the received 4G and 5G signals in the lower frequency bands, we have kept both electrical amplifiers in the CRoF architecture (inset (i)) and removed them from the proposed system (inset (ii)) for comparison purposes, as reported in Figure 6.8. The 5G NR standard has been evaluated using 16-, 64- and 256-QAM mapping.  $EVM_{RMS}$  after photodetection has been measured using the Inatel's 5G receiver and VSA. Despite the EAs absence, one can observe the photonically-amplified approach provides superior digital performance for all evaluated cases, giving rise to constellations with well-defined symbols and lower  $EVM_{RMS}$  when compared to CRoF system. Additionally, the 3GPP recommendations in terms of  $EVM_{RMS}$  [91] have been satisfied in all cases, including 256-QAM, namely:  $EVM_{RMS} \approx 1.6\%$  for the 64-QAM F-OFDM at 788 MHz and 256-QAM LTE at 2.7 GHz signals;  $EVM_{RMS}$  lower than 2% for the 5G NR standard at 3.5 GHz with 16-, 64- and 256-QAM mapping. The digital performance enhancement ensured by PAA was more apparent for the 5G NR signals, since the EVM parameter of the F-OFDM and LTE signals were very close to our piece of full scale equipment. As a conclusion, the novel PAA technique provided enhanced digital performance over a CRoF system with purely electrical RF amplifiers. The multi-band 5G NR RoF system with 15-dB PAA might be then potentially considered for supporting 4G/5G applications, either reducing the number of RF amplification stages at RRU or extending the mobile coverage for mm-waves Gbit/s 5G communications.

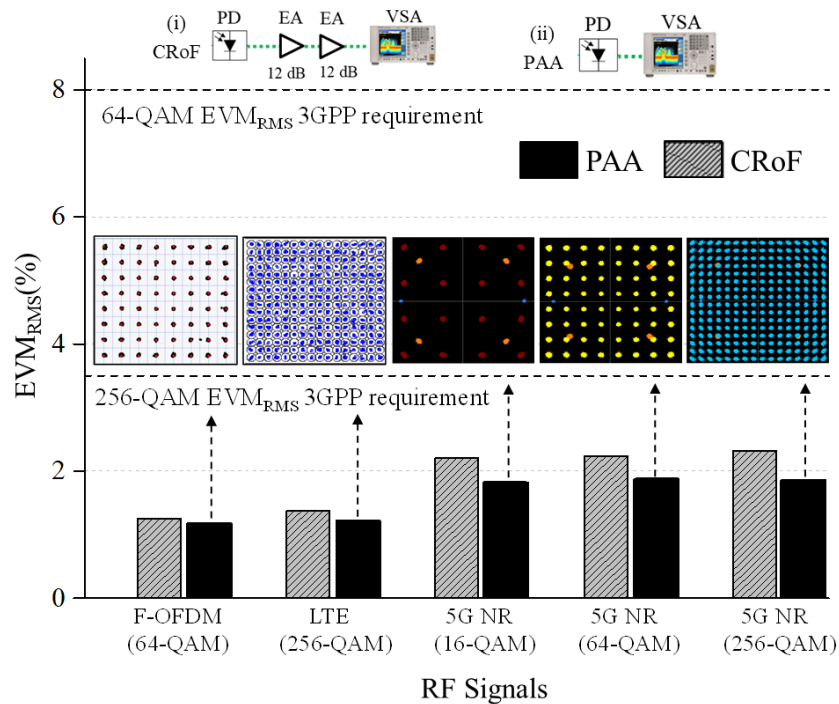


Figure 6.8 – Digital performance analysis of the F-OFDM, LTE, and 5G NR signals, assuming PAA without RF amplifiers and CRoF with two cascaded 12 dB EAs.

## 7. Final remarks

### 7.1. Conclusions

The 5G systems design within the scope of IMT-2020 and beyond has demanded for a physical layer network review, as well as the use of innovative technical solutions to fulfill diverse challenging scenarios and stringent requirements. Regarding the technical solutions proposed directly in the electrical domain, one can highlight the use of the recently launched 5G New Radio (NR) standard, additional spectrum bands including mm-waves, new waveforms and massive MIMO techniques. In parallel, the network planning has pointed out to optical-wireless convergence, mobile dense heterogeneous networks (HetNet) and centralized radio access network (C-RAN). C-RAN key advantages over the traditional distributed RAN (D-RAN) are the following ones: centralization of several base stations functions in a single location, enabling to share facilities as power and air-conditioning; management efficiency and reduced network deployment time, making practicable the base stations expansion; easier and agile communication between co-located baseband units (BBUs), contributing to the low latency applications; energy consumption reduction. These features contribute to reduce both capital and operational expenditures (CAPEX and OPEX) on radio access networks.

Microwave photonics has been recognized as an important enabler for the emerging broadband fiber-wireless (FiWi) 5G systems, bringing radio over fiber (RoF) solutions for midhaul and fronthaul, as well as techniques for enhancing the mobile system performance and making the mm-waves use feasible. Digital and analog RoF (D-RoF and A-RoF) solutions have been proposed in the literature in support of 5G fronthauling. Although D-RoF is the main available solution today, A-RoF topologies have been gradually becoming attractive as the envisaged throughput in the air increases and industry begins to deploy mm-waves access for 5G. The A-RoF main advantages over D-RoF are related with the centralization and remote radio unit (RRU) simplification, besides bandwidth and processing savings. These features make A-RoF schemes attractive to fit the C-RAN principle.

In order to demonstrate the feasibility of designing multi-band A-RoF systems without requiring multiple lasers and optical modulators, we initially proposed two RoF topologies based on single-drive Mach-Zehnder modulator (SD-MZM) and dual-drive MZM (DD-MZM), respectively. These approaches were experimentally investigated for

simultaneously modulating an optical carrier with two distinct RF-driven signals, one at 6 GHz and another at 28 GHz. The coexistence of RF signals did not introduce signal-to-noise ratio (SNR) penalty to the 6-GHz photodetected signal, however imposed SNR decrease at 28 GHz. This SNR reduction was reduced when using the topology with DD-MZM, e.g. from 7.5 to 1.9 dB for received optical power = -9 dBm. The obtained results indicated a promising direction on employing DD-MZMs to support multi-band A-RoF systems.

Next, we successfully applied the A-RoF technology based on DD-MZM for implementing three 5G systems as proof-of-concept. The first one embraced the integration of a 5G transceiver, previously developed by our group, in a RoF-based fronthaul architecture with wavelength division multiplexing (WDM) overlay. The following signals were simultaneously distributed over such transport network: a Generalized Frequency Division Multiplexing (GFDM) signal at 735 MHz, planned for the 5G lower spectral band toward long-reach applications; a 26 GHz digital modulated signal, as a mm-wave 5G band for enabling eMBB; a baseband signal from a gigabit passive optical network (GPON). The GFDM-based 100 Mbit/s signal was evaluated in terms of modulation error ratio (MER), which kept above 40 dB for RF-driven signal power up to -9 dBm. Furthermore, the digital pre-distortion (DPD) functionality from the 5G transceiver enabled to enhance MER at higher output power levels, by means of overcoming the non-linearities caused by RF amplifiers and electro-optical conversions. Reaching  $MER > 38$  dB at the remote unit was considered as an attractive achievement, since this MER value is in accordance with that expected from commercial RF transmitters. The 26-GHz RF signal was investigated as a function of error vector magnitude (EVM) for bitrates up to 1 Gbit/s.  $EVM_{RMS}$  of 2.18% and 5.70% were obtained for 100 Mbit/s and 1 Gbit/s throughput, respectively. It means that Gbit/s communication was attained meeting the 3GPP  $EVM_{RMS}$  requirements with at least 6.8% margin. As expected, the latency and throughput measurements of the baseband data stream originally running over GPON presented no significant penalties. These results indicate that PON capillarity might be effectively explored toward 5G systems implementation, since the MER and EVM obtained with the RoF-based fronthaul on top of GPON do not compromise wireless transmissions.

The second deployment was defined as DSP-based flexible-waveform and multi-application 5G fiber-wireless (FiWi) system. The RoF-based FiWi solution exploited a passive optical network (PON) infrastructure, from a commercial Internet service provider, to address 5G scenarios and a new PROFINET-based application stack. The RF transmitted signals included a Filtered Orthogonal Frequency Division Multiplexing (F-OFDM) at

788 MHz toward long range cells, a standardized 5G NR at 3.5 GHz for enabling eMBB outdoor macrocells, and a wide-bandwidth 26-GHz QAM for addressing eMBB indoor femtocells. The arbitrary 26 GHz signal has been later replaced by a 5G NR signal at the same frequency. We have used a centralized DSP-based solution for generating and selecting the waveform (OFDM/GFDM/F-OFDM), as well as for linearizing the RoF link by means of DPD. The F-OFDM signal presented 30.9 dB MER and 29 Mbit/s throughput for 2 km range PON, followed by a 105 m wireless link operating at 788 MHz. The 5G NR signal at 3.5 GHz reached approximately 385 Mbit/s for a 13 m macrocell application supplied by the optical fronthaul. A 26-GHz 10-m range femtocell presented throughput up to 4 Gbit/s and  $\text{EVM}_{\text{RMS}}$  performance in accordance with the 3GPP Release 15 requirements, as a result of DPD use for compensating the system degradation in terms of magnitude and phase. By implementing the 26 GHz femtocell with the 5G NR standard, 380.65 Mbit/s throughput and  $\text{EVM}_{\text{RMS}}$  lower than 5% were achieved. Therefore, the implemented FiWi system performed a 4.41 Gbit/s maximum throughput in the air, i.e. Gbit/s wireless communication, meeting the 3GPP  $\text{EVM}_{\text{RMS}}$  requirements for 5G NR.

The third implementation was defined as multi-band 5G NR system with photonic-assisted RF amplification (PAA). In such approach, A-RoF technology based on the use of DD-MZM and four-wave-mixing (FWM) were explored for simultaneously distributing and amplifying a Long Term Evolution (LTE) and three 5G signals in the frequency range from 780 MHz to 26 GHz, coexisting in the mobile fronthaul. The novel PAA technique provided uniform 15 dB ultra-wideband RF gain and, consequently, enhanced digital performance over a conventional RoF (CRoF) system characterized by employing purely electrical RF amplifiers instead of PAA. It is worth highlighting the proposed PAA technique, in contrast to the previous photonics-based RF amplification methods, takes advantage of using a single wavelength and does not requiring optical pumping and optical filter. These features allow PAA straightforward integration to the transport networks. Experimental results demonstrated the multi-band 5G NR system implemented with PAA enabled 5.64 Gbit/s total throughput. The 3GPP recommendations in terms of  $\text{EVM}_{\text{RMS}}$  were attained with margin in all evaluated cases, reinforcing the feasibility of the 4G and multiple 5G signals coexistence. The innovative RoF system proved to be potential for either reducing the RF-amplifiers number at RRU or extending the mobile coverage for mm-waves Gbit/s 5G communications.

In conclusion, this work presented analog RoF solutions in accordance with the C-RAN concept for enabling multi-band and Gbit/s 5G systems. The proposed RoF-based fronthaul architectures proved to be able to support the upcoming eMBB scenario, as well as

the long range coverage usage case. The possibility of using existent fiber-to-the-home (FTTH) networks for distributing 5G candidate signals was validated. Specifically, we innovated on experimentally demonstrating multi-band Gbit/s RoF and FiWi transmission using a single laser diode and DD-MZM as RoF transmitter. We also innovated on addressing three 5G predicted bands, using the GFDM and F-OFDM 5G candidate waveforms in a real-time flexible way, and employing the 5G NR standard in microwave and mm-waves. To the best of our knowledge, this was the first implementation of a FiWi system including the transmission and analysis of the 5G NR standard, in accordance with 3GPP Release 15 at 26 GHz. An additional innovation was proposing and implementing the multi-band 5G NR system with a novel PAA technique. Therefore, we believe this research brings relevant contributions to the research field of 5G FiWi systems.

## 7.2. Future works

Since this research focused on experimental investigations, a starting point that might be exploited as future work regards the mathematical analysis of the reported RoF techniques based on SD-MZM and DD-MZM. Other future research topics related to this work are as follows:

- **Implementation of a full-duplex 5G FiWi system.** The implemented RoF and FiWi systems are able to perform RF signals transmission in the downlink direction. In order to demonstrate a complete 5G communication system, it is imperative to implement also the transmission in the uplink direction.
- **Further investigation of a RoF-based gap filler system.** Gap filler systems comprise a kind of single frequency network, in which a repeater retransmits the received RF signal using the same frequency. It has been applied to digital terrestrial television for enabling coverage in specific areas where the signal is hard to be reached, without requiring an additional frequency allocation. Due to the common lack of isolation between the receiving and transmitting antennas at the relay station, gap filler systems suffer from echo interference [162,163]. Thus, there is an opportunity to further exploit our RoF-based fronthaul solutions for also implementing gap filler systems with the aim of mitigating the echo problem.

- **Increasing the 26-GHz femtocell reach.** As reported on Chapter 5, it was implemented a 26-GHz femtocell with 10 m range. This wireless link was limited by the laboratory layout, once we chose do not move the expensive equipment outside the laboratory. Since the  $EVM_{RMS}$  results met the 3GPP  $EVM_{RMS}$  requirements with margins, a future work is extending the 26-GHz femtocell reach.
- **Upgrading the FiWi systems to the sixth-generation (6G) of wireless networks.** The vision and planning of 6G communications has begun, with an aim to provide performance superior to 5G and satisfy future demands of 2030 [164]. Among the potential technologies for 6G, optical-wireless convergence continues to play an important role and artificial intelligence (AI)/machine learning arises to support autonomous networks and innovative air-interface design [165]. Therefore, a future work is creating a fiber-wireless channel model (it is still not well defined in the literature) and investigating the AI applicability to deal with channel impairments for which the RF receivers are not designed for. In other words, such proposal suggests evaluating the AI impact on 5G/6G FiWi communications.

## Appendix A

### The main pieces of equipment and components used in the experiments

Device	Manufacturer	Model
Analog signal generator	Keysight	N5173B
Arbitrary waveform generator	Keysight	M9505A
DC-block	Mini-Circuits	BLK-18-S+
	Fairview Microwave	SD3379
Diplexer	Marki Microwave	DPX1721
Dual-drive Mach-Zehnder modulator	Photline	MZ-DD-LN-10
Electrical spectrum analyzer	Anritsu	MT8222B BTS Master
	Keysight	- FieldFox N9952A - MXA N9020A
Erbium doped fiber amplifier	Golight	OA-D-D-C-30-20-G-1-FA
Ethernet Tester	DATACOM WISE	TSW900ETH
Laser	Golight	OS-WT-D-C-20-0-0-P
Media converters	Planet	- GT-806A15(V4)
		- GT-806B15(V4)
Network analyzer	Keysight	FieldFox N9952A
Optical attenuator	Thorlabs	VOA50PM-FC
Optical circulator	OZ Optics	FOC-12N-111-9/125
Optical fiber	Draka	SMF DLPC9 code 279/01
Optical general distributor	Parks	DGO-Split:3200
Optical line terminal	Parks	20028S
Optical network unit	Parks	Fiberlink 4100
Optical power meter	Anritsu	CMA5
Optical spectrum analyzer	Anritsu	MS9740A
Optical splitter	Petcom	1x2 PLC Splitter Module
Photodetector	u <sup>2</sup> t	XPDV2120RA
Polarization controller	General Photonics	PolaRITE 5561726
Power monitor	OZ Optics	OPM-200
Power supply	- Keysight	- E3640A - E3646A
	- Minipa	- MPL-3303M - MPS-3035D
RF amplifiers	Fairview Microwave	SBUA-400-12-010-K
	QuinStar Technology	QLW-18404540-J0
	Mini-Circuits	- ZX60-83LN12+ - ZJL-6G+
RF combiner	Kete	KTPD-M2460-2-SMAF
Single-drive Mach-Zehnder modulator	Fujitsu	FTM7939EK
Universal software radio peripherals	National Instruments	NI USRP-2954R
Vector signal analyzer	Keysight	DSAZ632A
	Rohde & Schwarz	FSW-8351
Vector signal generators	Keysight	- E8267D - N5172B
	Rohde & Schwarz	SMBV100B
WDM coupler	Haphit	FFWM-2465-173211-2

## Appendix B

### Relationship between MER and EVM

The modulation error ratio is defined as [142]

$$MER = 10 \log_{10} \left\{ \frac{\sum_{u=1}^N (I_u^2 + Q_u^2)}{\sum_{u=1}^N (\delta I_u^2 + \delta Q_u^2)} \right\} [\text{dB}],$$

where  $N$  is the number of received symbols,  $(I_u, Q_u)$  refers to the ideal symbol co-ordinates and  $(\delta I_u, \delta Q_u)$  denote the error in the received symbol position, i.e. the distance from the ideal symbol co-ordinates to the received ones.

Regarding the error vector magnitude, it is defined as [142]

$$EVM_{RMS} = \sqrt{\left\{ \frac{\sum_{u=1}^N (\delta I_u^2 + \delta Q_u^2)}{\sum_{u=1}^N (I_u^2 + Q_u^2)} \right\}} \cdot 100\% = \sqrt{\left\{ \frac{\frac{1}{N} \sum_{u=1}^N (\delta I_u^2 + \delta Q_u^2)}{S_{\max}^2} \right\}} \cdot 100\%,$$

in which  $S_{\max}$  is the vector magnitude to the outermost state of the constellation.

To compare MER and EVM, it is convenient to write them without using decibels and percentages. Expressing MER as simple voltage ratio ( $MER_V$ ) leads to

$$MER_V = \frac{\sqrt{\sum_{u=1}^N (I_u^2 + Q_u^2)}}{\sqrt{\sum_{u=1}^N (\delta I_u^2 + \delta Q_u^2)}},$$

whereas writing EVM as simple voltage ratio ( $EVM_V$ ) results in

$$EVM_V = \frac{\sqrt{\frac{1}{N} \sum_{u=1}^N (\delta I_u^2 + \delta Q_u^2)}}{S_{\max}}.$$

After multiplying both  $MER_V$  numerator and denominator by  $\sqrt{1/N}$ , one can relate MER and EVM as [142]

$$MER_V \cdot EVM_V = \frac{\sqrt{\frac{1}{N} \sum_{u=1}^N (I_u^2 + Q_u^2)}}{S_{\max}} = \frac{1}{V},$$

which finally results in

$$EVM_V = \frac{1}{MER_V \cdot V} .$$

The peak to mean voltage ratio,  $V$ , is a constant for a given transmission system whether each symbol has the same probability of occurrence. Table A.1 lists  $V$  values found in the literature for different QAM constellations [142, 143].

Table A.1 – Peak to mean voltage ratios for QAM constellation formats.

QAM format	4	16	32	64	128	256
$V$ value	1	1.341	1.303	1.527	1.440	1.627

As a conclusion, MER and EVM measure essentially the same quantity and conversion between these parameters is possible if the constellation is known. Results from calculations for converting MER to EVM are reported in Table A.2.

Table A.2 – Examples of conversion between MER and EVM.

QAM format	MER [dB]	$MER_V$	$EVM_V$	$EVM_{RMS}$ [%]
16	16	6.31	$118.18 \times 10^{-3}$	11.82
	20	10.00	$74.57 \times 10^{-3}$	7.46
	25	17.78	$41.94 \times 10^{-3}$	4.19
	30	31.62	$23.58 \times 10^{-3}$	2.36
	38	79.43	$9.39 \times 10^{-3}$	0.94
64	18	7.94	$82.48 \times 10^{-3}$	8.25
	25	17.78	$36.83 \times 10^{-3}$	3.68
	30	31.62	$20.71 \times 10^{-3}$	2.07
	34	50.12	$13.06 \times 10^{-3}$	1.31
	43	141.25	$4.64 \times 10^{-3}$	0.46
256	25	17.78	$34.57 \times 10^{-3}$	3.46
	28	25.12	$24.47 \times 10^{-3}$	2.45
	32	39.81	$15.44 \times 10^{-3}$	1.54
	38	79.43	$7.74 \times 10^{-3}$	0.77
	40	100	$6.15 \times 10^{-3}$	0.61

## References

- [1] 5G PPP, “5G vision,” *White paper*, Feb. 2015.
- [2] ITU-R, “IMT vision - framework and overall objectives of the future development of IMT for 2020 and beyond,” *Recommendation ITU-R M.2083-0*, Sep. 2015.
- [3] I. Philbeck, “Connecting the unconnected: working together to achieve Connect 2020 Agenda targets,” *ITU White Paper*, 2017.
- [4] 3GPP, “5G; Service requirements for next generation new services and markets,” TS 22.261 version 15.6.0 Release 15, 2018.
- [5] ETSI, “5G; Study on Scenarios and Requirements for Next Generation Access Technologies,” TR 138 913 V14.2.0 (2017-05), 2017.
- [6] A. Osseiran et al., "Scenarios for 5G mobile and wireless communications: the vision of the METIS project," *IEEE Commun. Mag.*, vol. 52, no. 5, pp. 26-35, May 2014.
- [7] C. Bockelmann et al., “Massive machine-type communications in 5G: physical and MAC-layer solutions,” *IEEE Commun. Mag.*, vol. 54, no. 9, pp. 59-65, Sep. 2016.
- [8] J. Sachs, G. Wikstrom, T. Dudda, R. Baldemair, and K. Kittichokechai, “5G radio network design for ultra-reliable low-latency communication,” *IEEE Network*, vol. 32, no. 2, pp. 24-31, Apr. 2018.
- [9] L. Zhang, A. Ijaz, P. Xiao, and R. Tafazolli, "Multi-Service System: An Enabler of Flexible 5G Air Interface," *IEEE Commun. Mag.*, vol. 55, no. 10, pp. 152-159, Oct. 2017.
- [10] ITU, “Setting the scene for 5G: Opportunities & challenges,” *White paper*, 2018.
- [11] M. Vaezi, Z. Ding, and H. V. Poor, Eds., *Multiple access techniques for 5G wireless networks and beyond*. Cham: Springer, 2019.
- [12] Y. Liu et al., “Waveform design for 5G networks: analysis and comparison,” *IEEE Access*, vol. 5, pp. 19282-19292, Feb. 2017.
- [13] R. Gerzaguet et al., “The 5G candidate waveform race: a comparison of complexity and performance,” *EURASIP J. Wireless Commun. and Netw*, vol. 2017, no. 13, pp. 01-14, Jan. 2017.
- [14] D. Zhang, M. Matthé, L. Mendes, and G. Fettweis, “A study on the link level performance of advanced multicarrier waveforms under MIMO wireless communication channels,” *IEEE Trans. Wireless Commun.*, vol. 16, no. 4, pp. 2350–2365, Mar. 2017.
- [15] G. Wunder et al., “5GNOW: non-orthogonal, asynchronous waveforms for future mobile applications,” *IEEE Commun. Mag.*, vol. 52, no. 2, Feb. 2014.
- [16] I. B. F. de Almeida, L. L. Mendes, J. J. P. C. Rodrigues, and M. A. A. da Cruz, “5G waveforms for IoT applications,” *IEEE Commun. Surveys Tuts.*, vol. 21, no. 3, pp. 2554-2567, Apr. 2019.
- [17] P. Weitkemper, J. Bazzi, K. Kusume, A. Benjebbour, and Y. Kishiyama, “On regular resource grid for filtered ofdm,” *IEEE Commun. Lett.*, vol. 20, no. 12, pp. 2486–2489, Dec 2016.

- [18] V. Vakilian, T. Wild, F. Schaich, S. Brink, and J.-F. Frigon, "Universal-filtered multi-carrier technique for wireless systems beyond LTE," in *9th International Workshop on Broadband Wireless Access*, Proc. Globecom 2013, Dec. 2013.
- [19] N. Michailow et al., "Generalized frequency division multiplexing for 5th generation cellular networks," *IEEE Trans. Commun.*, vol. 62, no. 9, pp. 3045-3061, Aug. 2014.
- [20] J. Ferreira et al., "GFDM frame design for 5G application scenarios," *J. Communication and Information Systems*, vol. 32, no. 1, pp. 54-61, 2017.
- [21] 3GPP, "5G; Study on New Radio (NR) access technology," TR 38.912 version 15.0.0 Release 15, 2018.
- [22] J. Le et al., "Spectrum for 5G: global status, challenges, and enabling technologies," *IEEE Commun. Mag.*, vol. 56, no. 3, pp. 12-18, Mar. 2018.
- [23] Qualcomm, "Making 5G NR a reality: leading the technology inventions for a unified, more capable 5G air interface," *White paper*, Dec. 2016.
- [24] Anatel, "5G technology and satellites are addressed at Futurecom (in Portuguese)," Nov. 07, 2018. [Online]. Available: <http://www.anatel.gov.br/institucional/noticias-destaque/2102-tecnologia-5g-e-satelites-sao-abordados-no-futurecom>. [Accessed Feb. 27, 2019].
- [25] S. Rangan, T. S. Rappaport, and E. Erkip, "Millimeter-wave cellular wireless networks: potentials and challenges," *Proc. IEEE*, vol. 102, no. 3, pp. 366-385, Mar. 2014.
- [26] 3GPP, "5G; NR; User equipment (UE) radio transmission and reception; Part 3: Range 1 and Range 2 interworking operation with other radios," TS 38.101-3 version 15.3.0 Release 15, 2018.
- [27] A. Tzanakaki et al., "Wireless-optical network convergence: enabling the 5G architecture to support operational and end-user services," *IEEE Commun. Mag.*, vol. 55, no. 10, pp. 184-192, Oct. 2017.
- [28] N. Zhang, N. Cheng, A. T. Gamage, K. Zhang, J. W. Mark, and X. Shen, "Cloud assisted HetNets toward 5G wireless networks," *IEEE Commun. Mag.*, vol. 53, no. 6, pp. 59-65, Jun. 2015.
- [29] 5G-Range Consortium, "Remote area access network for the 5th generation," *Application and requirements report*, Apr. 2018.
- [30] C. I. H. Li, J. Korhonen, J. Huang, and L. Han, "RAN Revolution with NGFI (xhaul) for 5G," *J. Lightw. Technol.*, vol. 36, no. 2, pp. 541-550, Jan. 2018.
- [31] J. Yao, "Microwave photonics," *J. Lightw. Technol.*, vol. 27, no. 3, pp. 314-335, Feb. 2009.
- [32] J. Capmany and D. Novak, "Microwave photonics combines two worlds," *Nature Photon.*, vol. 1, pp. 319-330, Jun. 2007.
- [33] H. Chi and J. P. Yao, "A photonic analog-to-digital conversion scheme using Mach-Zehnder modulators with identical half-wave voltages," *Opt. Express*, vol. 16, no. 2, pp. 567-572, Jan. 2008.
- [34] R. A. Minasian, "Photonic signal processing of microwave signals," *IEEE Trans. Microw. Theory Tech.*, vol. 54, no. 2, pp. 832-846, Feb. 2006.

- [35] T. Li, E. H. W. Chan, X. Wang, X. Feng, and B. Guan, "All-optic photonic microwave phase shifter requiring only a single DC voltage control," *IEEE Photon. J.*, vol. 8, no. 4, 5501008, Aug. 2016.
- [36] T. R. Clark and R. Waterhouse, "Photonics for RF front ends," *IEEE Microwave Mag.*, vol. 12, no. 3, pp. 87-95, May 2011.
- [37] R. M. Borges, A. L. M. Muniz and Arismar Cerqueira S. Jr., "Development and performance analysis of a photonics-assisted RF converter for 5G applications," *Fiber and Integrated Optics*, vol. 36, no. 1-2, pp. 25-37, Dec. 2016.
- [38] P. Ghelfi et al., "A fully photonics-based coherent radar system," *Nature*, vol. 507, pp. 341-345, Mar. 2014.
- [39] F. Scotti, D. Onori, A. Bogoni, and P. Ghelphi, "Frequency-agile and filter-free wireless communication transceiver based on photonics," in *Optical Fiber Communications Conference (OFC)*, San Diego, United States of America, 2018, Paper M2G.2.
- [40] N. J. Gomes, P. P. Monteiro, and A. Gameiro, Eds., *Next generation wireless communications using radio over fiber*. Noida: John Wiley & Sons, 2012.
- [41] P. J. Winzer, D. T. Neilson, and A. R. Chraplyvy, "Fiber-optic transmission and networking: the previous 20 and the next 20 years," *Opt. Express*, vol. 26, no. 18, pp. 24190-24239, Sep. 2018.
- [42] Huber+Suhner, "Microwave cable assemblies," SUCOFLEX<sup>®</sup>329 datasheet, Revised Jul. 2019.
- [43] H. T. Friis, "A note on a simple transmission formula," *Proc. IRE*, vol. 34, no. 5, May 1946.
- [44] S. Iezekiel, Ed., *Microwave photonics: devices and applications*. Chichester: John Wiley & Sons, 2009.
- [45] G. Kalfas et al., "Next generation fiber-wireless fronthaul for 5G mmWave networks," *IEEE Commun. Mag.*, vol. 57, no. 3, pp. 138-144, Mar. 2019.
- [46] W. E. Stephens, T. R. Joseph, and B. U. Chen, "Analog microwave fiber optic communications links," in *IEEE MTT-S Int. Microw. Symp. Digest*, San Francisco, California, 1984.
- [47] A. J. Cooper, "Fibre/radio for the provision of cordless/mobile telephony services in the access network," *Electron. Lett.*, vol. 26, no. 24, pp. 2054-2056, Nov. 1990.
- [48] J. J. O'Reilly and P. Lane, "Remote delivery of video services using mm-wave and optics," *J. Lightw. Technol.*, vol. 12, no. 2, pp. 369-375, Feb. 1994.
- [49] P. Hartmann et al., "Wideband fibre-agnostic DAS using pluggable analogue optical modules," in *Proc. Int. Top. Meeting Microw. Photon.*, Grenoble, France, 2006.
- [50] M. Sauer, A. Kobayakov, and J. George, "Radio over fiber for picocellular network architectures," *J. Lightw. Technol.*, vol. 25, no. 11, pp. 3301-3320, Nov. 2007.
- [51] C. Yeh et al., "Theory and technology for standard WiMAX over fiber in high speed train systems," *J. Lightw. Technol.*, vol. 28, no. 16, pp. 2327-2336, Aug. 2010.
- [52] D. Wake, A. Nkansah, and N. J. Gomes, "Radio over fiber link design for next generation wireless systems," *J. Lightw. Technol.*, vol. 28, no. 16, pp. 2456-2464, Aug. 2010.

- [53] Optical Zonu, “RF over fiber products,” Optical Zonu Corporation. [Online]. Available: <https://www.opticalzonu.com/rfofproducts/>. [Accessed: Apr. 2019].
- [54] Huber+Suhner, “RF over fiber series,” Huber+Suhner. [Online]. Available: <https://www.hubersuhner.com/en/products/radio-frequency/rf-over-fiber-series/rf-over-fiber/rf-over-fiber>. [Accessed: Apr. 2019].
- [55] G. Qi, J. Yao, J. Seregelyi, S. Paquet, and C. B elisle, “Generation and distribution of a wide-band continuously tunable millimeter-wave signal with an optical external modulation technique,” *IEEE Trans. Microw. Theory Techn.*, vol. 53, no. 10, pp. 3090-3097, Oct. 2005.
- [56] M. Wei , M. Huchard, A. St ohr, B. Charbonnier, S. Fedderwitz, and D. S. J ager, “60-GHz photonic millimeter-wave link for short- to medium-range wireless transmission up to 12.5 Gb/s,” *J. Lightw. Technol.*, vol. 26, no. 15, pp. 2424-2429, Aug. 2008.
- [57] A. Kanno et al., “Coherent radio-over-fiber and millimeter-wave radio seamless transmission system for resilient access networks,” *IEEE Photon. J.*, vol. 4, no. 6, pp. 2196-2204, Dec. 2012.
- [58] X. Pang et al., “25 Gbit/s QPSK hybrid fiber-wireless transmission in the W-band (75–110 GHz) with remote antenna unit for in-building wireless networks,” *IEEE Photon. J.*, vol. 4, no. 3, pp. 691-698, Jun. 2012.
- [59] S. Hughes et al., “Agile micro- and millimeter-wave communication using photonic frequency conversion,” in *Optical Fiber Communications Conference (OFC)*, Anaheim, United States of America, 2016, Paper W1G.5.
- [60] C. Lim, Y. Tian, C. Ranaweera, T. A. Nirmalathas, E. Wong, and K. Lee, “Evolution of radio-over-fiber technology,” *J. Lightw. Technol.*, vol. 37, no. 6, pp. 1647-1656, Mar. 2019.
- [61] C. Liu, J. Wang, L. Cheng, M. Zhu, and G. Chang, “Key microwave-photonics technologies for next-generation cloud-based radio access networks,” *J. Lightw. Technol.*, vol. 32, no. 20, pp. 3452-3460, Oct. 2014.
- [62] F. Tian et al., “A novel concatenated coded modulation based on GFDM for access optical networks,” *IEEE Photon. J.*, vol. 10, no. 2, Feb. 2018.
- [63] H. N. Parajuli, H. Shams, L. G. Gonzalez, E. Udvary, C. Renaud, and J. Mitchell, “Experimental demonstration of multi-Gbps multi sub-bands FBMC transmission in mm-wave radio over a fiber system,” *Opt. Express*, vol. 26, no. 6, pp. 7306-7312, Mar. 2018.
- [64] B. G. Kim, S. H. Bae, H. Kim, and Y. C. Chung, “RoF-based mobile fronthaul networks implemented by using DML and EML for 5G wireless communication systems,” *J. Light. Technol.*, vol. 36, no. 14, pp. 2874-2881, Jul. 2018.
- [65] A. Delmade et al., “Performance analysis of analog IF over fiber fronthaul link with 4G and 5G coexistence,” *J. Opt. Commun. Netw.*, vol. 10, no. 3, pp.174-182, Mar. 2018.
- [66] F. Lu et al., “Sub-band pre-distortion for PAPR reduction in spectral efficient 5G mobile fronthaul,” *IEEE Photon. Technol. Lett.*, vol. 29, no. 1, pp. 122-125, Jan. 2017.
- [67] M. Noweir et al., “Digitally linearized radio-over fiber transmitter architecture for cloud radio access network’s downlink,” *IEEE Trans. Microw. Theory Techn.*, vol. 66, no. 7, pp. 3564-3574, Jul. 2018.

- [68] J. J. V. Olmos, T. Kuri, and K. Kitayama, "Reconfigurable radio-over-fiber networks: multiple-access functionality directly over the optical layer," *IEEE Trans. Microw. Theory Techn.*, vol. 58, no. 11, pp. 3001-3010, Nov. 2010.
- [69] S. Pan and J. Yao, "Simultaneous provision of UWB and wired services in a WDM-PON network using a centralized light source," *IEEE Photon. J.*, vol. 2, no. 5, pp. 712-718, Oct. 2010.
- [70] W. Ho, H. Peng, H. Lu, C. Ying, and C. Li, "Novel ROF/FTTX/CATV hybrid three-band transport system," *Opt. Express*, vol. 19, no. 7, pp. 6980-6989, Mar. 2011.
- [71] M. Morant, R. Llorente, M. P. Thakur, and J. E. Mitchell, "Full-standard broadcast DVB-T and wireless overlay on legacy and OFDM next-generation FTTH networks," in *IEEE International Conference on Communication Workshop (ICCW)*, London, UK, 2015.
- [72] J. G. dos Santos, "Radio over fibre techniques for backhaul and fronthaul," Ph.D. thesis, Technischen Universität Berlin, Berlin, 2017.
- [73] H. Zeng, X. Liu, S. Megeed, A. Shen, and F. Effenberger, "Digital signal processing for high-speed fiber-wireless convergence," *J. Opt. Commun. Netw.*, vol. 11, no. 1, pp. A11-A19, Jan. 2019.
- [74] M. Xu, F. Lu, J. Wang, L. Cheng, D. Guidotti, and Chang, "Key technologies for next-generation digital RoF mobile fronthaul with statistical data compression and multiband modulation," *J. Lightw. Technol.*, vol. 35, n. 17, pp. 3671-3679, Sep. 2017.
- [75] L. Li et al., "Enabling flexible link capacity for eCPRI-based fronthaul with load-adaptive quantization resolution," *IEEE Access*, vol. 7, pp. 102174-102185, Aug. 2019.
- [76] M. Bi, W. Jia, L. Li, X. Miao, W. Hu, "Investigation of F-OFDM in 5G fronthaul networks for seamless carrier aggregation and asynchronous transmission," *Optical Fiber Communications Conference (OFC)*, Los Angeles, United States of America, 2017, Paper W1C.6.
- [77] U. Habib, A. E. Aighobahi, T. Qinlan, S. D. Walker, and N. J. Gomes, "Analog Radio-Over-Fiber Supported Increased RAU Spacing for 60 GHz Distributed MIMO Employing Spatial Diversity and Multiplexing," *J. Lightw. Technol.*, vol. 36, no. 19, pp. 4354-4360, Oct. 2018.
- [78] X. Li et al., "Real-time demonstration of over 20 Gbit/s V- and W-band wireless transmission capacity in one OFDM-RoF system," in *Optical Fiber Communications Conference (OFC)*, Los Angeles, United States of America, 2017, Paper M3E.3.
- [79] M. Sung, S. Cho, J. Kim, J. K. Lee, J. H. Lee, and H. S. Chung, "Demonstration of IFoF-based mobile fronthaul in 5G prototype with 28-GHz millimeter wave," *J. Lightw. Technol.*, vol. 36, no. 2, pp. 601-609, Jan. 2018.
- [80] N. Argyris et al., "A 5G mmWave fiber-wireless IFoF analog mobile fronthaul link with up to 24 Gb/s multi-band wireless capacity," *J. Lightw. Technol.*, vol. 37, no. 12, pp. 2883-2891, Jun. 2019.
- [81] M. Morant, A. Trinidad, E. Tangdiongga, T. Koonen, and R. Llorente, "Experimental demonstration of mm-Wave 5G NR photonic beamforming based on ORRs and multicore fiber," *IEEE Trans. Microw. Theory Techn.*, vol. 67, no. 7, pp. 2928-2935, Jul. 2019.

- [82] X. Li, J. Yu, and G. Chang, "Photonics-aided mm-wave communication for 5G," in *Optical Fiber Communications Conference (OFC)*, San Diego, United States of America, 2019, Paper Th1F.1.
- [83] J. Zou, C. Wagner, M. Eiselt, "Optical fronthauling for 5G mobile: a perspective of passive metro WDM technology," in *Optical Fiber Communications Conference (OFC)*, Los Angeles, United States of America, 2017, Paper W4C.2.
- [84] Y. Zhu, Y. Wu, H. Xu, C. Browning, L. P. Barry, and Y. Yu, "Experimental demonstration of a WDM-RoF based mobile fronthaul with f-OFDM signals by using directly modulated 3s-DBR laser." *J. Lightw. Technol.*, vol. 37, no. 16, pp. 3875-3881, Aug. 2019.
- [85] X. Hu, C. Ye, and K. Zhang, "Converged mobile fronthaul and passive optical network based on hybrid analog-digital transmission scheme," in *Optical Fiber Communications Conference (OFC)*, Anaheim, United States of America, 2016, Paper W3C.5.
- [86] A. M. Souza, "Double-cavity self-seeding WDM-PON topologies as 5G networks analog fronthaul," M.Sc. Dissertation, University of São Paulo, São Carlos, 2018.
- [87] J. H. Lee, K. Choi, J. Moon, and C. Lee, "Seamless upgrades from a TDM-PON with a video overlay to a WDM-PON," *J. Lightw. Technol.*, vol. 27, no. 15, pp. 3116-3122, Aug. 2009.
- [88] N. Cheng, "Flexible TWDM PON with WDM overlay for converged services," *Opt. Fiber Technol.*, vol. 26, pp. 21-30, Dec. 2015.
- [89] A. Shahpari et al., "Real-time bidirectional coherent nyquist UDWDM-PON coexisting with multiple deployed systems in field-trial," *J. Lightw. Technol.*, vol. 34, no. 7, pp. 1643-1650, Apr. 2016.
- [90] 3GPP, "5G; NR; Overall description; Stage-2," TS 38.300 version 15.3.1 Release 15, 2018.
- [91] 3GPP, "Group Radio Access Network; NR; User Equipment (UE) radio transmission and reception; Part 1: Range 1 Standalone," TS 38.101-1 version 15.5.0 Release 15, 2019.
- [92] Parks, "Fiberlink 20028," Parks S/A Comunicações digitais. [Online]. Available: <https://parks.com.br/fiberlink20028ing.html>. [Accessed: Apr. 2020].
- [93] Intelbras, "SFP+ 10 Gbps converter module (in Portuguese)," Intelbras. [Online]. Available: <https://www.intelbras.com/pt-br/modulo-conversor-sfp-10-gbps-kts-2110>. [Accessed: Apr. 2020].
- [94] Parks, "Fiberlink 4100," Parks S/A Comunicações digitais. [Online]. Available: <https://parks.com.br/fiberlink4100ing.html>. [Accessed: Apr. 2020].
- [95] ITU-T, "Broadband optical access systems based on passive optical networks (PON)," Recommendation G.983.1, 2005.
- [96] ITU-T, "Gigabit-capable passive optical networks (GPON): General characteristics," Recommendation G.984.1, 2008.
- [97] IEEE, "Ethernet in the first mile task force," IEEE802.3ah, 2004.
- [98] IEEE, "10Gb/s Ethernet passive optical network," IEEE P802.3av task force, 2009.

- [99] ITU-T, “10-Gigabit-capable passive optical network (XG-PON) systems: Definitions, abbreviations and acronyms,” Recommendation G. 987, 2012.
- [100] ITU-T, “40-Gigabit-capable passive optical networks (NG-PON2): General requirements,” Recommendation G.989.1, 2013.
- [101] ITU-T, “Spectral grids for WDM applications: CWDM wavelength grid,” Recommendation G.694.2, 2003.
- [102] ITU-T, “Spectral grids for WDM applications: DWDM frequency grid,” Recommendation G.694.1, 2002.
- [103] D. Nessel, “NG-PON2 technology and standards,” *J. Lightw. Technol.*, vol. 33, no. 5, pp. 1136-1143, Mar. 2015.
- [104] V. Houtsma, D. V. Veen, and E. Harstead, “Recent progress on standardization of next generation 25, 50 and 100G EPON,” *J. Lightw. Technol.*, vol. 35, no. 6, pp. 1228-1234, Mar. 2017.
- [105] M. A. Romero, “Passive optical networks: Present status and future outlook,” in *SBMO/IEEE MTT-S International Microwave and Optoelectronics Conference (IMOC)*, Águas de Lindóia, Brazil, Aug. 2017.
- [106] C. DeSanti, L. Du, J. Guarin, J. Bone, and C. F. Lam, “Super-PON: an evolution for access networks,” *J. Opt. Commun. Netw.*, vol. 12, no. 10, pp. D66-D77, Oct. 2020.
- [107] U. Hilbk, Th. Hermes, J. Saniter, and F. J. Westphal, “High capacity WDM overlay on a passive optical network,” *Electron. Lett.*, vol. 32, no. 23, pp. 2162-2163, Nov. 1996.
- [108] ITU-T, “40-Gigabit-capable passive optical networks 2 (NG PON2): Physical media dependent (PMD) layer specification,” Recommendation G.989.2, 2019.
- [109] M. A. Habibi, M. Nasimi, B. Han, and H. D. Schotten, “A comprehensive survey of RAN architectures toward 5G mobile communication system,” *IEEE Access*, vol. 7, pp. 70371-70421, 2019.
- [110] I. A. Alimi, A. L. Teixeira, and P. P. Monteiro, “Towards an efficient C-RAN optical fronthaul for the future networks: A tutorial on technologies, requirements, challenges, and solutions,” *IEEE Commun. Surveys Tuts.*, vol. 20, no. 1, pp. 708-769, 1st Quart. 2018.
- [111] A. Checko et al., “Cloud RAN for mobile networks—A technology overview,” *IEEE Commun. Surveys Tuts.*, vol. 17, no. 1, pp. 405-426, 1st Quart. 2015.
- [112] China Mobile Research Institute, “C-RAN – The road towards green RAN,” *White paper*, version 2.5, pp. 1-44, Oct. 2011.
- [113] ZTE Corporation, “Green technology innovations,” *White paper*, 2011.
- [114] Gigalight Technology, “24.33Gb/s CPRI SFP28 10km IND optical transceiver,” GSS-SPO240-LRT datasheet, 2018.
- [115] T. Pfeiffer, “Next generation mobile fronthaul and midhaul architectures,” *J. Opt. Commun. Netw.*, vol. 7, no. 11, pp. B38-B45, Nov. 2015.
- [116] Ericsson AB, Huawei Technologies Co. Ltd, NEC Corporation and Nokia, “CPRI - Common Public Radio Interface,” eCPRI specifications. [Online]. Available: <http://www.cpri.info/spec.html>. [Accessed: May 2020].

- [117] X. Liu and N. Deng, “Emerging optical communication technologies for 5G,” in *Optical fiber telecommunications*, vol. 11. Elsevier Inc, 2020, ch. 17, pp. 751-783.
- [118] Mellanox Technologies, “100GbE CPRI QSFP28 MMF Transceiver,” MMA1B00-C100C datasheet, 2018.
- [119] Pilot Photonics, “Directly modulated laser,” DFB laser datasheet. [Online]. Available: <https://www.pilotphotonics.com/high-speed-lasers/>. [Accessed: May 2020].
- [120] Fujitsu, “40 Gbps intensity modulator,” FTM7939EK datasheet. [Online]. Available: <http://www.realphoton.com/en/?p=127>. [Accessed: May 2020].
- [121] Finisar, “Ultra-fast 100 GHz photodetector,” XPDV412xR datasheet, rev. A1, 2014.
- [122] G. P. Agrawal, *Nonlinear fiber optics*. New York: Academic Press, 2001.
- [123] X. Zhang, D. Shen, and T. Liu, “Review of linearization techniques for fiber-wireless systems,” in *IEEE International Wireless Symposium (IWS)*, X’ian, China, 2014.
- [124] S. Yao et al., “Non-orthogonal uplink services through co-transport of D-RoF/A-RoF in mobile fronthaul,” *J. Lightw. Technol.*, Early Access, Mar. 2020.
- [125] Intel, “Radiocommunications Reference Center,” Intel. [Online]. Available: <https://www.intel.br/crr/>. [Accessed: Sep. 2019].
- [126] C. B. Schlegel and L. C. Perez, “Low-density parity-check codes,” in *Trellis and turbo coding: iterative and graph-based error control coding*. Wiley-IEEE Press, 2015, pp. 249-318.
- [127] S. Sun and Z. Zhang, “Designing practical polar codes using simulation-based bit selection,” *IEEE J. Emerg. Sel. Topics Circuits Syst.*, vol. 7, no. 4, pp. 594–603, Dec. 2017.
- [128] M. Matthé, L. L. Mendes, N. Michailow, D. Zhang, and G. Fettweis, “Widely linear estimation for space-time-coded GFDM in low-latency applications,” *IEEE Trans. Commun.*, vol. 63, no. 11, pp. 4501-4509, Nov. 2015.
- [129] N. N. N. A. Malik, N. Ngajikin, S. M. Idrus, and N. D. A. Latif, “Peak to average power ratio (PAPR) reduction in OFDM System,” in *IEEE International RF and Microwave Conference*, Putra Jaya, Malaysia, 2006.
- [130] H. D. Rodrigues, “RF power amplifier linearization with orthogonal digital pre-distortion and scalar feedback (in Portuguese),” Federal University of Itajubá, Itajubá, 2017.
- [131] P. Neuhaus et. al., “Deliverable 3.2 physical layer of the 5G-RANGE – Part II,” *5G-RANGE Tech. Rep.*, Feb. 2019.
- [132] Keysight, “5G waveform generation and analysis testbed, reference solution,” Solution Brochure. [Online]. Available: <https://literature.cdn.keysight.com/litweb/pdf/5992-1030EN.pdf?id=2642005>. [Accessed: Sep. 2019].
- [133] Rohde & Schwarz, “Be ahead in 5G. Be ready for the future,” Rohde & Schwarz test solutions for 5G. [Online]. Available: [https://scdn.rohde-schwarz.com/ur/pws/dl\\_downloads/dl\\_common\\_library/dl\\_brochures\\_and\\_datasheets/pdf/1/Rohde-Schwarz\\_5G\\_fly\\_Overview\\_en\\_5214\\_9896\\_62\\_v0200\\_120dpi.pdf](https://scdn.rohde-schwarz.com/ur/pws/dl_downloads/dl_common_library/dl_brochures_and_datasheets/pdf/1/Rohde-Schwarz_5G_fly_Overview_en_5214_9896_62_v0200_120dpi.pdf). [Accessed: May 2020].

- [134] Intel, “Intel realiza 1ª demonstração de uma tecnologia nacional para 5G,” Intel. [Online]. Available: <https://www.intel.br/imprensa/noticias/pesquisa-e-inovacao/3084-intel-realiza-1-demonstracao-de-uma-tecnologia-nacional-para-5g>. [Accessed: Sep. 2019].
- [135] 5G-Range, “5G-Range functionalities,” 5G-Range. [Online]. Available: <http://5g-range.eu/index.php/2019/05/15/5g-range-functionalities/>. [Accessed: Sep. 2019].
- [136] C. Lin et al., “Optical millimeter-wave up-conversion employing frequency quadrupling without optical filtering,” *IEEE Trans. Microw. Theory Techn.*, vol. 57, no. 8, pp. 2084-2092, Aug. 2009.
- [137] G.H. Smith, D. Novak, and Z. Ahmed, “Technique for optical SSB generation to overcome dispersion penalties in fibre-radio systems,” *Electron. Lett.*, vol. 33, no. 1, pp. 74-75, Jan. 1997.
- [138] Marki Microwave, “Broadband diplexer,” DPX-1721 datasheet, 2014.
- [139] Marki Microwave, “Ultra-wideband Wilkinson power divider,” PD-OR636 datasheet, 2018.
- [140] S. Yu, T. Jiang, J. Li, R. Zhang, G. Wu, and W. Gu, “Linearized frequency doubling for microwave photonics links using integrated parallel Mach-Zehnder modulator,” *IEEE Photon. J.*, vol. 5, no. 4, Aug. 2013.
- [141] Photline, “Dual-drive 10 GHz intensity modulator,” MZDD-LN-10 datasheet. [Online]. Available: <https://www.symphotony.com/wp-content/uploads/MZDD-LN-10.pdf>. [Accessed: Jun. 2020].
- [142] ETSI, “Digital video broadcasting (DVB); Measurement guidelines for DVB system,” TR 101 290 v1.3.1, 2014.
- [143] W. Fischer, *Digital video and audio broadcasting technology: A practical engineering guide*. München: Springer, 2010.
- [144] Rohde & Schwarz, “MER and coverage in broadcast network planning,” Rohde & Schwarz. [Online]. Available: [https://scdn.rohde-schwarz.com/ur/pws/dl\\_downloads/dl\\_common\\_library/dl\\_brochures\\_and\\_datasheets/pdf\\_1/MER-vs-Coverage\\_fly\\_en\\_3606-8820-32\\_v0101.pdf](https://scdn.rohde-schwarz.com/ur/pws/dl_downloads/dl_common_library/dl_brochures_and_datasheets/pdf_1/MER-vs-Coverage_fly_en_3606-8820-32_v0101.pdf). [Accessed: Jun. 2020].
- [145] Hitachi Kokusai Linear, “E-compact HP UHF digital TV transmitters,” High power ISDB-T digital TV transmitters brochure, Revised Nov. 2019. [Online]. Available: [https://www.hitachi-linear.com.br/products/pdf/\(EN-US\)%20E-Compact High Power UHF ATSC ISDB-T REV07.pdf](https://www.hitachi-linear.com.br/products/pdf/(EN-US)%20E-Compact%20High%20Power%20UHF%20ATSC%20ISDB-T%20REV07.pdf). [Accessed: Jun. 2020].
- [146] Screen, “ARK-X universal driver,” TV transmitters catalog. [Online]. Available: <https://www.screen.it/wp-content/uploads/2019/06/Screen-ARK-X-2019.pdf>. [Accessed: Jun. 2020].
- [147] D. López-Pérez et al., “Enhanced intercell interference coordination challenges in heterogeneous networks,” *IEEE Wireless Commun.*, vol. 18, no. 3, pp. 22-30, Jun. 2011.
- [148] PROFIBUS & PROFINET International (PI), “PROFINET – The solution platform for process automation,” *White Paper*, Jun. 2018.
- [149] M. Luvisotto, Z. Pang, and D. Dzung., “High-performance wireless networks for industrial control applications: new targets and feasibility,” *Proc. IEEE*, vol. 107, no. 6, pp. 1074-1093, Jun. 2019.

- [150] 3GPP, “Group RAN; NR; Base Station (BS) conformance testing Part 1: Conducted conformance testing,” 3GPP TS 38.141-1 version 1.0.0 Release 15, 2018.
- [151] M. Luvisotto, Z. Pang, and D. Dzung., “Ultra high performance wireless control for critical applications: challenges and directions,” *IEEE Trans. Ind. Informat.*, vol. 13, no. 3, pp. 1448–1459, Jun. 2017.
- [152] V.J. Urick, M. S. Rogge, F. Bucholtz, and K.J. Williams, “Wideband (0.045–6.25 GHz) 40km analogue fibre-optic link with ultra-high (>40 dB) all-photonic gain,” *Electron. Lett.*, vol. 42, no. 9, pp. 552-553, May 2006.
- [153] Fairview Microwave, “50 MHz to 40 GHz, broadband amplifier using USB control with 10 dBm, 12 dB gain and 2.92mm,” SBUA-400-12-010-K Datasheet, Rev. 1.0, 2015.
- [154] W. S. Wall and M. A. Foster, “Ultra-wideband gain in microwave photonic links using four-wave mixing,” in *Proc. Int. Conf. on Lasers and Electro-Optics (CLEO)*, San Jose, CA, 2012. Paper CTu3A.4.
- [155] Arismar Cerqueira S. Jr. et al., “Photonic-assisted microwave amplification using four-wave mixing,” *IET Optoelectron.*, vol. 10, no. 5, pp. 163-168, Sep. 2016.
- [156] A. L. M. Muniz, R. M. Borges, R. N. da Silva, D. F. Noque, and Arismar Cerqueira S. Jr., “Ultra-broadband photonics-based RF front-end toward 5G networks,” *J. Opt. Commun. Netw.*, vol. 8, no. 11, pp. B35-B42, Nov. 2016.
- [157] A. L. M. Muniz, D. F. Noque, R. M. Borges, A. Bogoni, M. Hirano, and Arismar Cerqueira S. Jr., “All-optical RF amplification toward Gpbs communications and millimeter-waves applications,” *Microw. Opt. Technol. Lett.*, vol. 59, no. 9, pp. 2185-2189, Sep. 2017.
- [158] D. F. Noque, R. M. Borges, A. L. M. Muniz, A. Bogoni, and Arismar Cerqueira S. Jr., “Thermal and dynamic range characterization of a photonics-based RF amplifier,” *Opt. Commun.*, vol. 414, pp. 191-194, 2018.
- [159] E. S. Lima, R. M. Borges, L. A. M. Prereira, H. R. D. Filgueiras, A. M. Alberti, and Arismar Cerqueira S. Jr., “Multiband and photonicallly amplified fiber-wireless Xhaul,” *IEEE Access*, vol. 8, pp. 44381-44390, Mar. 2020.
- [160] C. J. McKinstrie and G. Raymer, “Four-wave-mixing cascades near the zero-dispersion frequency,” *Opt. Express*, vol. 14, no. 21, pp. 9600-9610, Oct. 2006.
- [161] J. Yao, “A tutorial on microwave photonics,” *IEEE Photon. Society Newslett.*, pp. 4-12, Apr. 2012.
- [162] C. Rocha, C. Akamine, G. B. Junior, E. L. Horta, and G. Stolfi, “Adaptive gap filler for digital terrestrial television,” in *IEEE International Symposium on Broadband Multimedia Systems and Broadcasting*, Beijing, China, 2014.
- [163] Y. Kaneko, K. Nishiyasu, T. Higashino, and M. Okada, “An evaluation of radio over fiber based gap-filler for high definition mobile broadcasting,” in *IEEE International Symposium on Broadband Multimedia Systems and Broadcasting*, Nara, Japan, 2016.
- [164] S. Dang, O. Amin, B. Shihada, and M. Alouini, “What should 6G be?,” *Nature Electron.*, vol. 3, pp. 20-29, Jan. 2020.
- [165] Z. Zhang et al., “6G wireless networks: Vision, requirements, architecture, and key technologies” *IEEE Veh. Technol. Mag.*, vol. 14, no. 3, pp. 28-41, Sep. 2019.